INSTITUTO POLITÉCNICO DE BRAGANÇA Escola Superior de Tecnologia e de Gestão

UNIVERSIDADE TECNOLÓGICA FEDERAL DO PARANÁ

Fire Performance on the Load Bearing LSF Walls

Fallconny Rodrigues Sensato Oliveira

Thesis Submitted to the School of Technology and Management of the Polytechnic Institute of Bragança (Portugal) with the Technological Federal University of Paraná (Brazil) to the Fulfilment of the Requirements for the Double Degree program to obtain the degree of

Master of Science in Industrial Engineering - Mechanical Engineering branch.

Supervised by:

Prof. Doctor Paulo Alexandre Gonçalves Piloto

Prof. Doctor Henrique Cotait Razuk

Bragança

December 2020

INSTITUTO POLITÉCNICO DE BRAGANÇA Escola Superior de Tecnologia e de Gestão

UNIVERSIDADE TECNOLÓGICA FEDERAL DO PARANÁ

Fire Performance on the Load Bearing LSF Walls

Fallconny Rodrigues Sensato Oliveira

Thesis Submitted to the School of Technology and Management of the Polytechnic Institute of Bragança (Portugal) with the Technological Federal University of Paraná (Brazil) to the Fulfilment of the Requirements for the Double Degree program to obtain the degree of

Master of Science in Industrial Engineering - Mechanical Engineering branch.

Supervised by:

Prof. Doctor Paulo Alexandre Gonçalves Piloto

Prof. Doctor Henrique Cotait Razuk

Bragança

December 2020

"Man is the most insane species. He worships an invisible God and destroy a visible Nature, unaware that, this Nature he's destroying is the God he's worshiping".

Hubert Reeves.

Acknowledgement

First of all, I would like to thank my family, specially my mother, Eliane and my sister Andressa, which made possible for me to come all the way from Brazil to Portugal. They have been a huge support for me in this period. Thanks both of you for teaching me to never give up and to always give my best, I love you.

To my friends from Brazil, I also thank you for the good memories, jokes, parties and fun times spent together. For the ones I met at UTF, I'll always have you with me! To Renan and Carol, thank you for driving me to Curitiba that day in such short notice, so I could get the documents for the visa, if it wasn't for that, I would not be here today.

To the friends I made in Bragança, thank you!! You were amazing, we had the best apartment ever! Italy, Spain and Brazil are the best friends combinations and I hope to see you soon again. Of course, for the Turkish and Polish girls, thanks for the best quarantine that I could have! Thanks all of my Braganças' friends for the last months supports, it has been really important for me.

I thank the Federal Technological University of Paraná (UTFPR) that gave me the opportunity to come to the Polytechnic Institute of Bragança (IPB). It has been the most amazing experience of my life, expanding my knowledge and social relationships. Special thanks to IPB for the support provided during the Covid-19 pandemic.

Thank you, Flaminio and Tadashi for our brotherhood (it can't be called friendship anymore), for our time spent here, the emotional support, and for all the good music and cooking.

A special thanks to Prof. Paulo Piloto and Prof. Henrique Razuk, for the supervision in this work.

Abstract

This work presents a numerical validation study of a load bearing light steel frame (LSF) wall structure in respect to full scale-test, to obtain the fire resistance of the wall. Three parametric studies were performed to evaluate the influence of the plasterboard's thickness, plasterboard restriction and steel section in the fire resistance of load bearing LSF wall. Simplified studies were also developed in order to compare with advanced calculation models. The finite element method was done in three stages: (1) simulation at room temperature to obtain the buckling and ultimate loads, (2) simulation of the transient thermal analysis to obtain the temperature distribution and (3) simulation of the thermomechanical analysis to obtain the fire resistance and critical temperature of the load bearing wall under fire. Results showed good agreement at room temperature. In the thermal analysis, the model was able to predict the temperature field with good accuracy, however, for thermomechanical, the model did not show good agreement with test results. In respect to the parametric analysis, plasterboard thickness influenced in the temperature distribution, resulting in a higher critical temperature in the thermomechanical simulation. Plasterboard restriction is affecting the lateral deflection of the wall in thermomechanical simulation. The steel section has a big effect in the load bearing capacity at room temperature, regarding the buckling and ultimate load, it also affects the out of plan displacement in the thermomechanical simulation. Simplified methods have been used to predict the critical temperature results under fire, with good conservative prediction for lower load ratios.

Keywords: Light Steel Frame. Load Bearing Walls. Numerical Simulation. Fire resistance.

Resumo

Este trabalho apresenta um estudo de validação numérica de uma parede portante feita em estrutura de Light Steel Frame (LSF), em relação a ensaios em escala real, com o objetivo de obter a resistência ao fogo da parede. Para avaliar a influência de outros parâmetros, três estudos paramétricos foram realizados: a influência da espessura da placa de gesso, a influência da restrição da placa de gesso e a influência secção da viga de aço na resistência ao fogo da parede portante de LSF. Estudos simplificados também foram desenvolvidos para fins de comparação com modelos de cálculo avançados. Realizou-se as simulações em elementos finitos em três etapas: (1) simulação à temperatura ambiente para obter as buckling loads e cargas últimas, (2) simulação térmica transiente para obter as distribuições de temperaturas e (3) análise termomecânica para obter a resistência ao fogo e a temperatura crítica da parede portante em situação de incêndio. Os resultados mostraram boa concordância à temperatura ambiente. Na análise térmica, o modelo foi capaz de reproduzir o campo de temperatura com boa precisão, porém, para termomecânica o modelo não apresentou boa concordância com os resultados do teste. No que diz respeito à análise paramétrica, a espessura do painel de gesso influenciou na distribuição da temperatura, resultando em uma temperatura crítica mais elevada na simulação termomecânica. A restrição da placa de gesso está afetando a deflexão lateral da parede na simulação termomecânica. A secção da viga de aço tem um grande efeito na capacidade de carga à temperatura ambiente, no que diz respeito ao buckling e a carga última, ela também afeta o deslocamento para fora do plano na simulação termomecânica. Métodos simplificados foram usados para prever os resultados de temperaturas crítica sob fogo, com previsão conservadora para load ratios menores.

Palavras-chave: Estruturas de Aço Leve. Paredes Portantes. Simulação Numérica. Resistência ao fogo.

Summary

List of Tables

List of Figures

Chapter 1

Introduction

Since the beginning of humankind, men and women have settled inside caves to protect themselves against rain, animals and to be together as families. Over time, they became nomads, in which, required new adaptions to their place to live: light easily removable tents that could be moved without many problems, because they were moving constantly to find better places. After the agriculture revolution, most of the nomads people turned into sedentary, transition that, once more, required evolution of the means of living, such as houses. So, they started to need, besides a place to live and protect themselves, somewhere they could store their agriculture production.

The sedentism enabled the agglomeration of different folks and the cities started to emerge. After years, new needs for homes were appearing, such as running water, gas, electricity and, more recently, internet connection. In addition, news concepts of aesthetics building that involves arts and different shapes are currently being widely used. This caused the emergence of more complex houses and buildings that comes with several risks: collapses and fire due electrical and gas usage.

Therefore, buildings are expected to be safe for the people that work or live inside them, generating requirements to be fulfilled. For this reason, in the last years many researchers are focusing in the development of standards and methods to enhance safety of building construction products , keeping houses as comfortable spaces.

1.1 LSF Walls

Load bearing Lightweight Steel Frame (LSF) walls assemblies are structural members made by cold-formed steel that are widely used on buildings, because they offers numerous advantages as light weight (which implies not heavy lifting equipment required), steel members that can be supplied to the exact lengths required, eliminating cutting and waste, they also are prefabricated with the necessary space for service installations (piping and electrical network), minimizing work [1].

LSF walls can be responsible of holding weights from elements above it or not. If they are used to bear loads, they will be classified as load bearing, by contrast, non-load bearing walls are responsible, solely, of hold themselves up, besides other functionalities. The LSF walls are constructed by connecting studs and tracks with screws, to form an easy assembled and fabricated frame for load bearing or non-load bearing function. A typical LSF assembly is shown in Figure 1.1. In this work, only load bearing LSF walls are to be investigated.

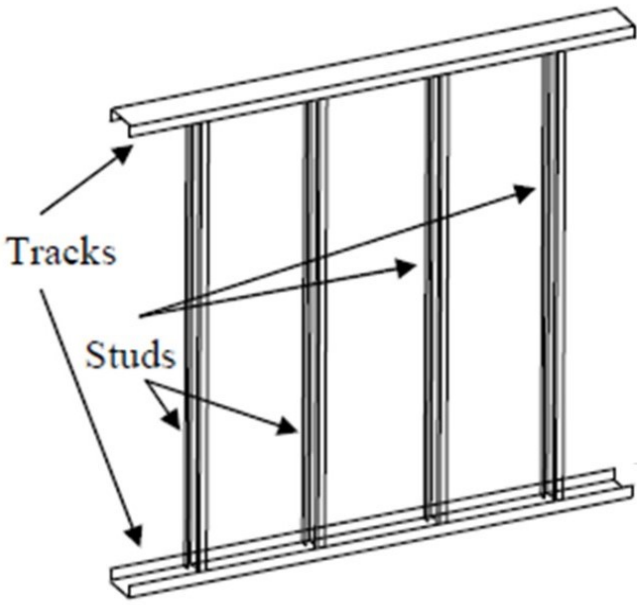

Figure 1.1: Typical LSF Wall assembly (Modified from [2]).

The lightweight steel framing can be applied in residential, industrial and commercial

buildings (see Figure 1.2). These framing are resistant and non-combustible, allowing them to resist under fire and natural events, like earthquakes and storms. Under fire conditions, the steel temperature rises rapidly causing a reduction in strength and stiffness. For this reason, usually, plasterboards are applied in both sides to serve as fire protection and slow down the steel heating up process. Therefore, LSF wall are expected to have fire resistance, in which, may considers the integrity (E), the insulation (I) and the structural adequacy (R) to provide enough time for safe evacuation of occupants and prevent fire spread to others rooms.

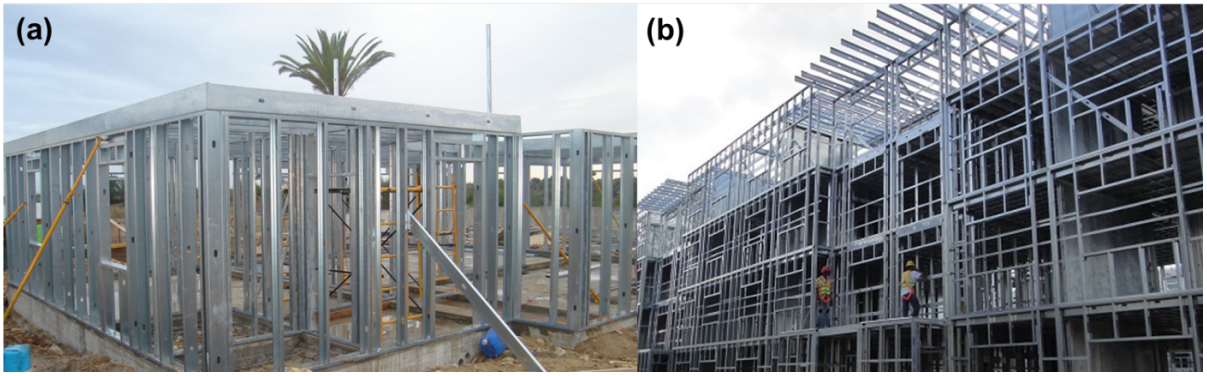

Images from: (a): http://www.soluft.pt/ (b): http://mapsa.co.ir/ [Accessed 18 Oct. 2020]

Figure 1.2: LSF Wall systems.

In order to quantify the fire resistance of LSF walls, standard tests are usually developed using standard fire curves. These tests consist in submit the wall to a fire condition (heated from one side) while loads are being applied on the top or in the bottom, simulating a real load bearing LSF wall.

However, standard tests are time consuming and expensive, and requires the usage of modern technology, also a high qualified personal. For this reason, others methods may be used to evaluate the fire resistance, such as advanced calculation method. Therefore, the motivation of this Thesis is to develop a advanced calculation method using a finite element model.

1.2 Objectives

This work presents numerical validation and a parametric numerical analysis, regarding the fire resistance of load bearing LSF walls, using different configuration and materials.

Specific tasks are to be investigated: different thickness of panels, their thermal behaviour characterization and different types of steel sections.

Two different methods are to be used in order to determine the fire resistance: advanced calculation method and simplified calculation method.

Special numerical tasks aim to develop accurate advanced calculation method using a finite element model to predict fire resistance with ANSYS Multiphysics. The validation of the 3D finite element model is presented.

1.3 Thesis Content

Chapter 2: presents the state of the art which describe, in a temporal line, studies regarding load bearing LSF walls.

Chapter 3: presents the fire event and the standard fire curves. It also describes the heat transfer theory.

Chapter 4: presents the LSF walls assemblies, the fire safety requirements and fire resistance using standard tests with standards involved. This chapter also discuss about the insulation, plasterboard and steel properties.

Chapter 5: presents the advanced calculation method with the finite element method and all the necessary boundary conditions: LSF wall geometry, material properties and finite element information.

Chapter 6: presents the parametric study and the influence of different parameters.

Chapter 7: presents the application of the simplified method to estimate the fire resistance of LSF walls.

Chapter 8: presents the main conclusions about this work and future investigations that are required.

Appendix A: presents the LSF Wall representations.

Appendix B: presents the material proprieties.

Chapter 2

State of the Art

This chapter describe the literature review of the research of load bearing LSF Wall under fire conditions. The research aimed on finding experimental, numerical and simplified models investigation about the fire performance on load bearing LSF Wall. All the information found is going to be displayed in a temporal line together with the results of each researcher.

2.1 Experimental Tests

In the last years, research about the behaviour of cold-formed lightweight steel framing (LSF) has increased, to develop safer design rules that allows LSF walls construction elements with the required needs. Among them, LSF walls are expected to resist the load bearing imposed by the building construction, even during extreme condition such as fire. Therefore, knowing the behaviour of those structures under fire condition implies a safer design. Due to this, in 1973, the Department of Housing and Urban Development of Washington, D.C, sponsored two test of LSF wall proposed for low rise multifamily residential conducted by the Fire Research Section of the National Bureau of Standard [3].

In the research, Son and Shoub [3] used double-walls assemblies with gypsum boards constructed on metal studs. Elements were tested in accordance with the requirements

of ASTM Standard E119-71 (Fire Test of Building Construction and Materials). The applied load was calculated from the weight of the modules that were above and with a live load, ceiling and roof (with snow load included) load.

Klippstein [4], in 1980, did an experimental study using two C-section LSF Walls. During tests, the individual steel studs' loads were significantly different from the intended average load during the pre-load and this difference increased during the fire test. Klippstein stated that since the frame above the walls are very rigid, the loads in the centre stud increase more rapidly, leading to an earlier structural failure. He concluded that in last test, the total load applied into the wall was nearly 100% greater than the initial load, implying that the hydraulic response of the testing equipment has to change due stud elongations.

Only in 1995 another study about load bearing LSF walls was published by Gerlich [5]. In his research, load bearing LSF drywall system were tested with standard ISO834 fire and real compartment fires. In the experimental test, he used a moving bottom platen to apply the constant load to the LSF wall, in contrast to the Klippstein [4] tests, it allowed the vertical thermal expansion of the steel framing members to occur, avoiding the increase of the applied loads during fire tests.

In 2006, Kodur and Sultan [6], researched about the factors that influenced fire resistance in load bearing walls. In total, they tested 14 walls assemblies, with plasterboard in the exposed and unexposed side and glass, rock, dry brown cellulose fibre insulation in the cavity. Results showed that insulation type and number of plasterboards have expressive influence on the fire resistance.

In 2013, Gunalan and Mahendran [7], proposed a new composite wall panel to improve fire resistance rating of LSF walls, in which the insulation layer has been externally applied between plasterboards on both sides instead of using in the cavity. The results showed that externally insulated LSF wall have higher fire performance in comparison with the insulated cavities.

In 2015, Kesawan and Mahendran [8] proposed a new type of stud section, instead of using lipped channel, commonly used, they used hollow flange channel (HFC) sections

studs. The study aimed to verify the behavior of LSF walls made of welded HFC section studs under standard fire conditions and compare them with conventional LSF walls made of lipped channel. Results showed that fire performance of welded HFC section studs were superior of those made with conventional lipped channels.

In 2018, Dias, Keerthan and Mahendran [9] proposed another stud section, web-stiffened channel sections (SCS). Results showed that the performance of SCS channel is higher than lipped channel and equal to welded HFC (hollow flange section) sections from previous study [8], [10]. They also concluded that the performance of HFC and SCS were equivalent, the SCS channels are economically a more efficient alternative to welded HFC sections, due to the manufacturing cost. Therefore, it was concluded that stiffened channel section provides economical and structurally efficient alternative for use in LSF walls.

2.2 Numerical Simulations

In 1995, Gerlich [5] made one of the first study using a numerical model to predict the heat transfer and steel framing temperature using TASEF (Temperature Analysis of Structures Exposed to Fire), a two dimensional finite element heat transfer software. The model gave good agreement when compared with temperatures from the full-scale test, however it was more accurate when using ISO834 time-temperature curves than when using natural fire curve. It happened because the software was not able to predict the severe thermal degradation of the gypsum plasterboard causing temperature to rise quickly over time.

In 2000, Alfawakhiri and Sultan [11] did an analytical thermomechanical model for LSF using data from six standard fire resistance tests. The numerical simulations were conducted using the TRACE (Temperature Rise Across Construction Elements) software. Different from Gerlich [5], the software could model the spalling of gypsum board by taking it off the simulation at a user-specified time, thus the registered time of spalling based on visual test observations were used. They also used another software, STUD to simulate

the structural behavior of the load bearing LSF walls. The results were very accurate for all simulations, however the STUD software could not predict so accurately the lateral deflection at failure time.

In 2006, Telue and Mahendran [12] developed studies with FEA (finite element modelling) using the MSC/PATRAN and ABAQUS software to understand the behavior of one side lined steel wall frames. Their FEA result was validated with experimental results from previous tests made by them. The results of the ultimate load, failure mode agreed well with FEA, and design rules based on the finite element modelling results was developed and proposed as improvement to the normative.

In 2013, Gunalan and Mahendran [13] developed a finite element model of load bearing LSF wall based on tests made by them in 2013 [7]. They were able to input complex thermal and structural effects as thermal bowing and local buckling to the finite element analyses and the FEA model was validated using experimental tests [7]. The FEA was conduct using only one stud to represent the whole wall and the results agreed well with the tests.

Kesawan and Mahendran [10] in 2016 developed a finite element model to predict the fire performance of LSF walls made of hollow flange channel. The FEA results agreed well with full scale tests and also confirmed that LSF walls made of HFC sections studs had superior fire performance compared with conventional LSF walls with lipped channel.

In 2018, Dias, Keerthan and Mahendran [9] proposed another stud section, web-stiffened channel sections (SCS). They performed FEA tests with LSF walls made of SCS and validated using fire tests results. Results showed that the stud geometry on the fire performance of LSF wall configurations is minimal. Thus, considering performance results and the reduced cost, they concluded that the SCS is recommended for use in LSF walls.

2.3 Simplified Methods

In 1978, Klippstein [4], [14] presented the first ever made simplified method to predict the failure time for load bearing LSF walls under standard fire from ASTM E119-7. In his study, Klippstein proposed a load-ratio criterion (LR), based on the failure load at room temperature to be applied uniformly to all studs in the test panel. Results for failure time of LSF wall assemblies were derived as a function of LR for different thickness of gypsum boards. However, these curves were not conservative for high-load ratios and his method was dependent on empirical determination of stud temperatures and lateral deflections.

In 1995, Gerlich [5], proposed equations to solve the thermal deflections, assuming that the horizontal deflection of studs was the sum of a thermal bowing deflection, proposed by Cooke [15],due to the temperature gradient (assuming linear variation for temperature across the stud) and a secondary deflection caused by the bending moment. He used data from Klippstein and Cooke [14], [4], [15] to fit a polynomial curve to the yield strength and elasticity modulus reduction in function of time and used as an input to his calculations. The result agreed very well between the deflections calculation from measured temperatures and the measured horizontal deflections.

In 2000, Alfawakhiri and Sultan [11], presented an expression for lateral deflection at the mid-height of the LSF wall, considering the results effect of the sum of the free initial imperfection caused by thermal bowing and the secondary deflection caused by the eccentricity of the load with eccentricity. Then, these expressions were incorporated in the STUD software to predict the behavior of load bearing LSF Walls. Predictions for non-insulated walls showed reasonable agreement with test structural failure times. Furthermore, they stated that predictions based on measured temperatures show a better agreement with test results than based on simulated temperatures.

In 2005, Zhao et al. [16] did an extensive report with full-scale tests and numerical evaluation for the European Committee. One of their aims was to develop simplified design methods for LSF walls. Their approach was equal to the ENV 1993-1-3 but with some modifications as including variation of the material properties in function of temperature

and considering thermal bowing effects. The proposed calculation model was suitable to predict with a good precision the cold-formed steel 'C' section fire resistance with small temperature gradient. However, for steel section under large temperature gradient it was not capable to predict with an acceptable accuracy.

In 2010, Kolarkar [17] developed in his thesis, a simplified method to determine the failure times for load bearing LSF walls. Kolarkar presented a graphical solution method, in which, used the yield stress reduction factors and idealized time-temperature profiles to approximate the failures times of LSF wall system. This method considers non-insulated and insulated cavity, also, externally insulated wall specimens. The predict failure time from the method proposed showed good agreement when compared to actual times of failures from specimens tested.

In 2014, Gunalan and Mahendran [18] proposed a simplified method based on two sets of equations to predict temperature as function of time during a standard fire and the failure temperature in function of load ratio for LSF wall systems considering various steel and pasteboard-insulation configurations. Results showed that their method agreed well when compared to corresponding FEA and test results.

In 2018, Piloto, Khetata and Gavilán [19], proposed a new formula based in the load level applied to the LSF wall to determine the critical temperature of the studs. The formula was developed based on numerical studies validated with full-scale tests.

In 2020, Chen et al. [20] proposed a simplified method, in which, used a reference temperature for correction to the equal area method and energy-based method. They also preliminary proposed a time-equivalent method of cavity-insulated load bearing walls, their results showed good agreement with experimental results. However, it was stated that their time-equivalent method stills needed to be verified and corrected with more analyses from cold formed steel walls under fire conditions

Chapter 3

Fire

This chapter presents information about the fire event and the thermal loads involved. Also describes the standard fire curves and presents the basic theory for heat transfer.

Fire is a process of combustion with heat emission and it happens when three factors exists simultaneously: fuel (1), heat source (ignition) (2) and oxidizing atmosphere (3) [21]. Fuel can be any kind of substance, oxidizing is the substance that reacts with the fuel, commonly is oxygen or air.

To start the fire an ignition is required, which provides enough temperature variation that the mix of (1) and (3) reaches its ignition point, making the transition to the growth period. As soon as the process of combustion starts (1) and (3) are needed for it to continuous exists, but the ignition source is not needed anymore, as the energy released by combustion is used to continuously feed the process, creating a chain reaction. If the chain reaction goes out of control then a fire situation happens, in which can lead to permanent damage to life, the environment and heritage [21].

Therefore, taking in to account the severe risks that a fire event can bring, several actions were taken to develop fire safety for compartments. In particular, for construction elements, fire curves were generated to simulate their behaviour under fire, thus, being able to develop actions and standards to provide safety. Namely, according to EN 1991-1-2, there are different types of curves, such as: Natural Fire and Standard Fire temperature-time curves [22]. These curves allow for standards tests, in which the fire performance

and fire resistance of construction elements can be determined.

3.1 Natural Fire

Natural fire or real fire represents a time-temperature curve for a process of fire inside a compartment. The natural fire curve is divided in four periods: incipient (ignition), growth, burning and decay, as shown in Figure 3.1.

The initial period of fire development is the incipient, in which heating of fuel is taking place. Ignition occurs when the oxidizing substance (mixture of gases) is heated to high temperatures that starts exothermic oxidation reaction of combustion, transitioning the curve to the growth period [21]. The amount of heat and temperature needed to initiate ignition depends on the properties of the fuel, size and shape of ignite object (that can be, among others: matches, candles, gas heaters and cigarettes) and also the time of exposure to heat. The time to ignite materials depends on the product of three properties: thermal conductivity, density and specific heat [21], named thermal inertia. This propriety defines which materials heat more rapidly when compared to others: higher thermal inertia leads to much more fast ignition than lower thermal inertia materials.

In the growth period, fire starts to propagate throughout the room and spread first due to combustible surfaces. A large number fire events do not consider this phase, mainly because there is no sufficient fire load or air supply to allow further growth, however in many cases, at this point, human intervention may be the cause for the flashover, such as: more air supply is provided by opening a door or window [23].

The periods before flashover is often ignored in the response analysis of the structural members, because the temperatures here are not high enough to cause significant change in the structural behaviour, reason why standard curves do not take it into consideration. However, this stage is very important when designing for life safety, because most of the toxic gases are created during these periods.

Hot gases created by combustion will hit the ceiling and if fire continuous to grown

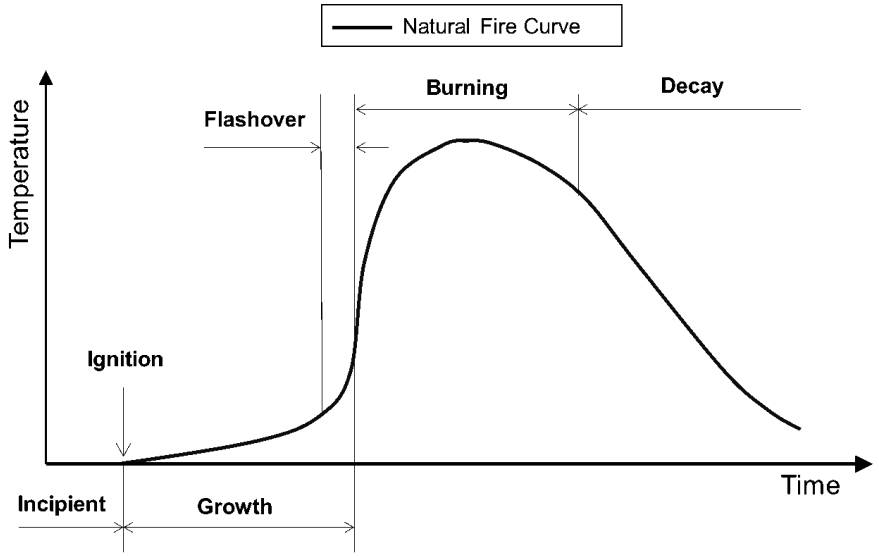

Figure 3.1: Time-temperature periods for a full process of fire development (Modified from [21], [23]).

without intervention, temperatures of the ceiling will rise, therefore, magnifying the radiant flux to all other objects in the room [24]. When the heat flux reaches a critical level, all available combustible items in the room will burn, causing the heat and temperatures to rise rapidly. In other words, the fire ceases to be a local phenomenon and start to be within all the compartment, this transition is called flashover. A flashover only occurs if there is sufficient fuel and ventilation for development of the fire, typically it occurs when the hot layer temperature at the ceiling is about 600 [°C], or a radiant heat flux about 20 [kW/m^2] at floor [21], [23], exists. After that, starts the post-flashover stage, also called full developed fire, the burning period.

During the burning period, the combustion gases and air flows are considered turbulent, generating high heat flux by radiation and high temperatures throughout the compartment. The maximum temperature is obtained during this period, temperatures in the post-flashover stage can be in the order of about 1000 [°C] [21]. The temperature rises until the combustible consumption start to decrease or there is not sufficient oxygen to feed the process. This period is critical for structural design, because the structural elements are exposed to severe effect of fire, high temperatures that modify the material properties, in which, collapse or loss of integrity and insulation are likely to happen [23].

After reaching the temperature peak, decay phase begins, where the temperatures start to decrease as reduction of combustible in the compartment.

Performance based structural design with natural fire curves are more precisely since it shows the behaviour under real situation, however, the estimation of temperature in post-flashover fire cannot be done precisely [21]. Numerous tests were carried out to measure and develop methods to predict it, but the temperature depends at any time of many variables, such as openings in the compartment, heat losses by radiation, convection and conduction into to walls, floor, ceiling and thermal properties from the objects inside the compartment. In this regard, parametric curves were developed, which are more realistic time-temperature curves, that can be used to any fuel load, openings and materials. However, those curves are not of interest to this work, only the effect of standard fire curves is to be investigated.

3.2 Standard Fire Curves

Standard fire curves are an approximation to natural curves, but not take in consideration the openings, space, fire load density in the compartment and do not account the decay phase. These curves represent the temperature increase after flashover period, in which the structure is under high heat and temperature load, therefore, considered a critical point of analysis.

The Eurocode 1: Actions on structures, part 1.2: general actions on structures expose to fire, presents three nominal fire curves: standard, external fire and hydrocarbon curve [22]. In this work, only the ISO 834 standard curve will be used and the formula is given by the eq. 3.1.

$$\theta_g = 20 + 345 \cdot log_{10}(8 \cdot t + 1) \qquad [°C] \quad (3.1)$$

Where θ_g is the gas temperature in the fire compartment in [°C] and t is the time in minutes [min]. The time-temperature plot curve for four hours is shown in Figure 3.2.

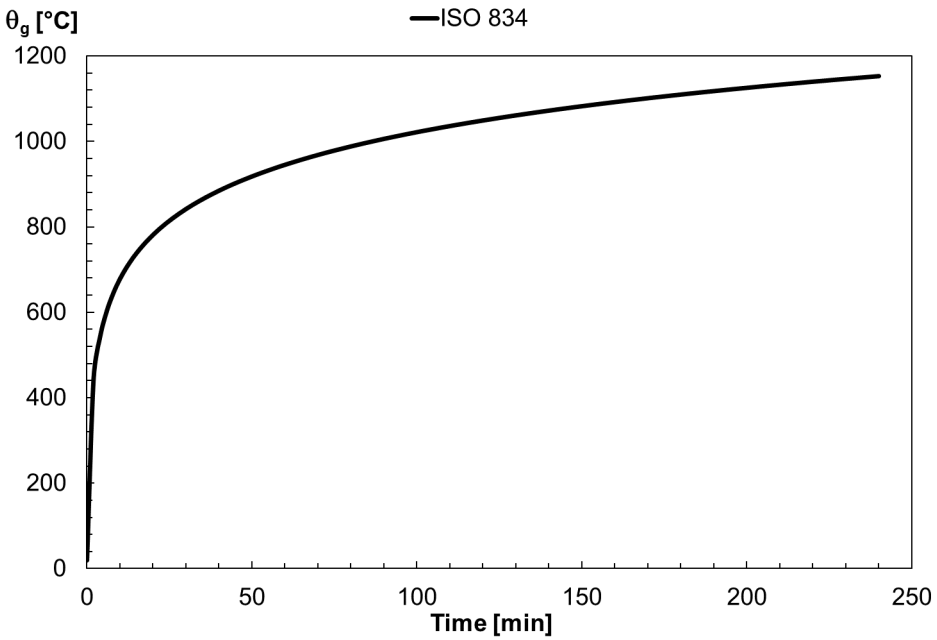

Figure 3.2: ISO 834 standard time-temperature curve.

3.3 Heat Transfer

The fire scenario depends on energy interactions of the objects inside the compartment with the surroundings. During this event, thermal energy is being transferred due to temperature difference across the compartment. Thermal energy in transit is defined as heat transfer and can occur by three process: conduction, convection and radiation, in which, can act together or separately.

Conduction is heat transfer in solid and stationary flux, when there is a temperature gradient in these medium. This process is an important aspect to fire resistance of barriers and structural members and depends, in solids, of the density, specific heat and thermal conductivity from materials.

Convective heat is when thermal energy is transferred by fluids in movement to the surface of a solid material, heating or cooling it. In a fire situation, convective heat has influence in flame spreading, transport of smoke and hot gases to the ceiling or out the window from the compartment [21]. For fire exposed surfaces, the net convective heat flux, according to the EN 1991 part 1.2 [22] is determined by eq. 3.2.

$$\dot{h}_{net,c} = \alpha_c \cdot (\theta_g - \theta_m) \qquad [\mathrm{W}/m^2] \quad (3.2)$$

In which, α_c is the coefficient of heat transfer by convection in [W/m^2·K], θ_g is the gas temperature in the vicinity of the fire exposed member [°C] and θ_m is the surface temperature of the member or material in [°C]. For applications using ISO 834 time-temperature curve, discussed in the previous section, the coefficient of heat transfer by convection should be taken as $\alpha_c = 25$ [W/m^2·K][22].

Radiation is the energy transferred by electromagnetic waves, in which can travel through any kind of medium and does not depend on their characteristics. In some fire events, radiation is responsible to transfer heat from hot flames to combustibles surfaces or from hot smoke to building objects inside the compartment. According to the EN 1991 part 1.2 [22] the net radiative heat flux per unit of surface area exposed to fire is given by e.q 3.3.

$$\dot{h}_{net,r} = \Phi \cdot \varepsilon_m \cdot \varepsilon_f \cdot \sigma \cdot [(\theta_r + 273)^4 - (\theta_m + 273)^4)] \qquad [\mathrm{W}/m^2] \quad (3.3)$$

Where, Φ is the configuration or view factor that may be taken as $\Phi = 1{,}0$, but lower values can be used to consider shadow effects. The surface emissivity of the member, ε_m, unless given in other design standard, a value of $\varepsilon_m = 0{,}8$ is to be used. Fire emissivity, ε_f, should be taken as $\varepsilon_f = 1{,}0$. The σ represent the Stephan Boltzmann constant equal to $5{,}67 \cdot 10^{-8}$ [W/m^2·K^4], θ_r represents the effective radiation temperature of the fire environment [°C] whlie θ_m is the surface temperature of the member in [°C] [22]. For fully fire engulfed members, which will be analysed in this work, θ_r can be represented by the gas θ_g temperature around the member. The gas temperature, on the other hand, can be adopted as nominal temperature-time curves, such as ISO 834 from eq. 3.1.

Thermal actions on the fire exposed surfaces, the net heat flux is given by the sum of convection and radiation shown in eq. 3.4 below [22].

$$\dot{h}_{net} = \dot{h}_{net,c} + \dot{h}_{net,r} \qquad [\mathrm{W}/m^2] \quad (3.4)$$

In which, $\dot{h}_{net,c}$ and $\dot{h}_{net,r}$ are given by equations 3.2 and 3.3 respectively. On the unexposed surface of separating members, $\dot{h}_{net}$ should be determined using eq. 3.4 with $\alpha_c = 4\ [W/m^2 \cdot K]$, if effects of heat transfer by radiation are to be considered separately, or $\alpha_c = 9\ [W/m^2 \cdot K]$ if the effect of radiation is to be included in the net heat flux by convection [22].

Chapter 4

LSF Walls Assemblies

This chapter will describe the assembly, design and fire resistance of LSF walls for fire safety. Also, standards involved in the process of determining fire resistance of load bearing LSF walls will be discussed.

The load bearing capacity of LSF walls comes from materials properties of cold-formed steels, commonly, galvanized mild steels and from the geometry [17]. These steels can assume different sections and are created by cold rolling processes, using thin metal sheets. This process causes hardening due to cold rolling effects, affecting the load bearing capacity. There are many cross section shapes available, such as plain C-section, lipped C-section, Z section and hollow section. In addition, the cold rolling process produces geometric imperfections and residual stresses that compromise the load bearing capacity of structural members and LSF walls.

Cold-formed steel when exposed to temperature variation, as in fire events, because of their thin thickness, heat up and loses strength and stiffness more rapidly when compared with others steel, like hot-rolled, reaching values in order of 10-20% more in strength loss [1], [17]. In order to delay the temperature variation in LSF Walls, fire resistant barriers are included to help maintaining integrity and hinder fire spread to adjacent compartments in fire situations. Therefore, LSF Walls frames can be lined in one or both sides with one, or more, sheeting of gypsum board (plasterboards) or others materials, that form walls and increases the level of fire protection (see Figure 4.1).

In LSF walls design, for fire safety reasons, fire resistance is required according to each national regulation. The fire resistance represents the ability of the load bearing wall to withstand exposure to fire. Fire resistance is evaluated by considering the amount of time that the wall can be exposed to standard fire curves, using experimental tests, without losing its fire load bearing or fire separating requirements [24]. For this evaluation, three standards are to be used: EN 1363-1 (Fire resistance tests – General Requirements) [25], EN 1991-1.2 (Eurocode 1: Actions on structures exposed to fire) [22] and EN 1993-1.2 (Eurocode 3: Design of steel structures – General rules: Structural fire design) [26].

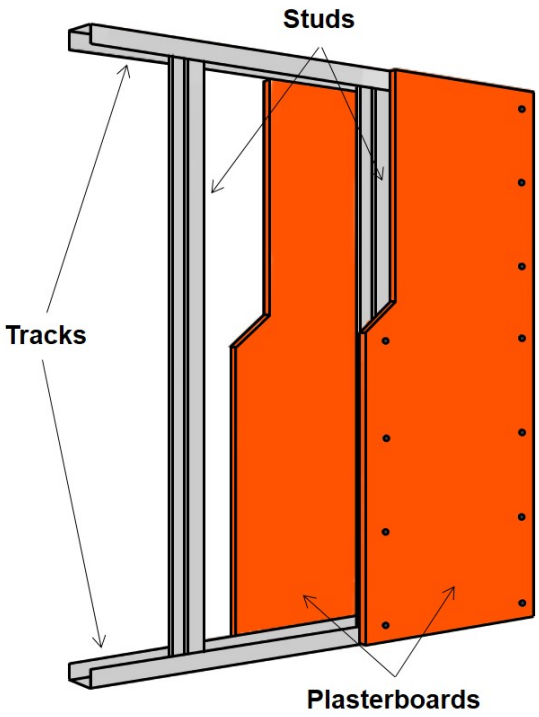

Figure 4.1: LSF Wall lined in both sides with one sheeting of plasterboard.

4.1 Fire Safety

Fire safety may be assumed as a set of actions to prevent the ignition of fire and measures to limit the development, minimizing risks and destruction in a fire event. Thus, fire safety engineering is the application of scientific and engineering principles to prevent

and reduce the loss of life, damage to property and environment, by providing protective and preventive measures solutions [23].

When designing building structures, regarding to fire safety, there are five points to be considered: (1) control of ignition, (2) control of means of escape, (3) detection of fire, (4) control of fire spread, (5) prevention of structure collapse. For that, active and passive measures should be applied.

Active measures are provisions that require manual or automatic controls in order to work, such as provision of alarm system, smoke control system, in-built firefighting or fire control system. Fire extinguisher, fire blanket and sprinklers, are very well known examples of active fire protection measures.

Passive measures, by contrast, do not need any type of activation, they are an integral component of building structures and should provide control of flammability of the structure fabric, provision of fixed escape routes and adequate structural performance. In this work, only actions related to provide adequate structural performance are to be investigated, therefore, no active or other passive measures will be analyzed.

The provision of structural performance is to assure that there are no total collapse of the structure during a fire event, that is, fire resistance. Fire resistance has to ensure enough time for evacuation of the occupants and for firefighting operations, and also prevent fire spread during exposure to a specified fire severity. Fire severity is a measure of the destructive impact of a fire, or a measure of temperatures or the loads that could lead the structure collapse or other failure caused by the fire [21]. Therefore, designing structure for fire safety is to verify if the fire resistance is equal or bigger than the fire severity. Table 4.1 shows three possible different methods for comparing fire severity with fire resistance in time domain, temperature domain and strength domain, according with Buchanan and Kwabena [21].

In time domain, fire resistance can be defined by the time, in which, the structure failed during test when exposed to standard fire. The fire severity, in this scenario, is the time specified by the standard or national regulation.

In temperature domain, the maximum temperature in any part of the structure should

Table 4.1: Methods for comparing fire severity with fire resistance (Modified from [21]).

Domain	Units	Fire Resistance	$\geq$	Fire Severity
Time	min or h	Time to failure	$\geq$	Fire duration as calculated or specified by standard or regulation
Temperature	°C	Temperature to cause failure (critical temperature)	$\geq$	Maximum temperature reached by the material during the fire
Strength	kN or kNm	Load bearing capacity at elevated temperature	$\geq$	Applied load during the fire

not be greater than the temperature that could lead to failure (critical temperature). Failure in this scenario can be the loose of separating capability of the element due excessive temperature rise or structural collapse of load bearing structures. Non-load bearing LSF walls are considered to be separating element and failure is when the temperature on the unexposed face reaches a certain value that allows fire to spread into others compartment, specified by the standard.

In strength domain, the verification is made by comparing the minimum load capacity reached and the applied load at the time of fire.

To verify the fire resistance of elements in any of the domain cited above, fire resistance tests may be developed and will be discussed next.

4.2 Fire Resistance Test

In general, countries have their own building codes (national regulations), generally based on standards, that specify the required fire resistance rating for building elements, often, specified in hour or minutes. The fire resistance rating can be obtained through full-scale fire resistance tests, however, these are very expensive, and are only made when necessary [21].

Full-scale tests for load bearing walls, consist in exposing one surface of the LSF Wall to fire and applying the required load by hydraulic jacks (keeping the possibility to reduce load as long as the element tries to expand), or by the use of weights in a furnace. The test is carried out using representative specimens of building elements. An example of a furnace is showed in 4.2.

A test furnace, typically, consist of a large steel box lined with ceramic fibre blanket or fire bricks and inside there are burners, in which, are mandatory to be able to reproduce the standard time-temperature curve [21]. According to EN 1363-1 [25], the loading equipment must be able to provide constant test load, reason why, the interface beam (platen) is used (see Figure 4.2), to ensure that the load is being well distributed on the wall.

The temperature inside the furnace should follow the curve under testing, based on reading from plate thermocouples. The plate thermocouple should be placed in the specific position of the furnace at a distance of 100 +/- 50 [mm] from the specimen. According to test method, EN 1364-1: Fire resistance tests for non-load bearing elements - Part 1: Walls, one should use 1 thermocouple for each $1{,}5m^2$ of the element under analysis. According to the general requirements for testing elements under fire, EN 1363-1: Fire resistance tests - Part 1: General requirements, the furnace thermocouples should be separated from the burners and away from the wall (450 [mm]).

The reaction frames should be able to reproduce the boundary and support conditions such as restraint against expansion, contraction or rotation [25].

The objective of fire resistance tests is not to simulate real fires, rather, allow fire performance comparison between structures through a standard method. The method gives ways of quantifying the fire resistance of elements exposed to standard fires by determining their fire resistance rating. In accordance to EN 1363-1 the resistance rating is obtained by setting, among others, three failures criteria: load bearing capacity (R), fire containment (integrity) (E) and thermal transmittance (insulation) (I) [25].

a) Load bearing capacity (R)

Load bearing capacity is the time that the LSF Wall specimen is able to maintain

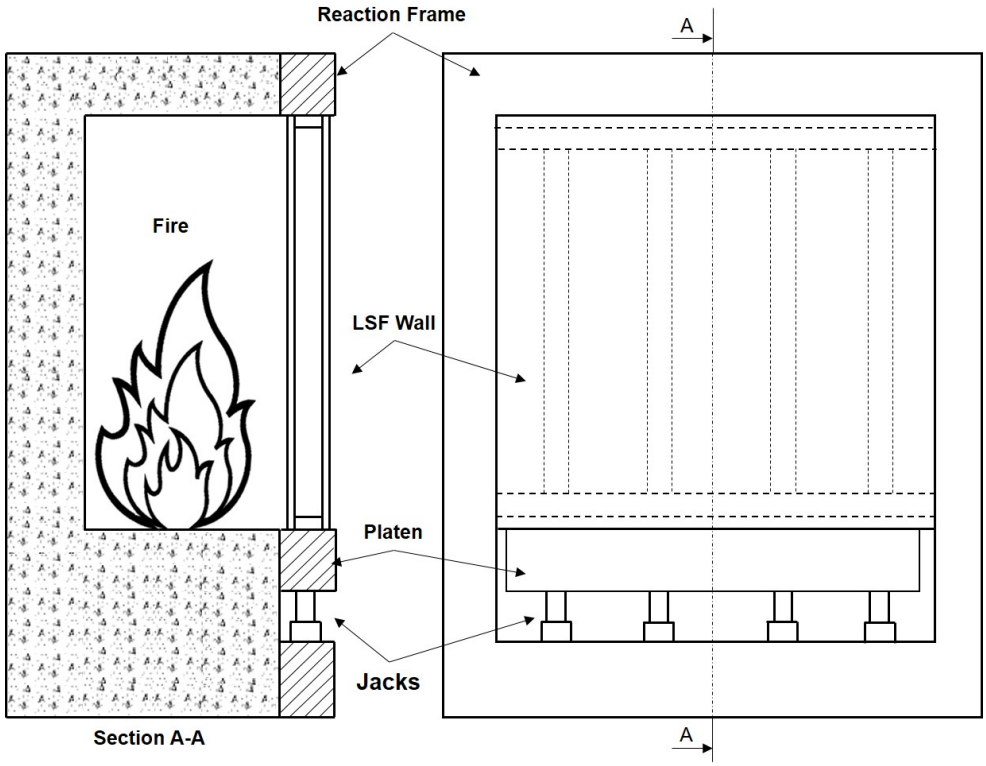

Figure 4.2: Example of a testing furnace for load bearing LSF Wall (Modified from [21]).

its ability to support the load during the test. Accord to EN 1363-1, the LSF failure to support the load occurs, for vertically loaded elements, by limiting vertical contraction (see eq. 4.1) or limiting the rate of vertical contraction (see eq. 4.2) [25].

$$C = \frac{h}{100} \qquad \text{[mm]} \quad (4.1)$$

$$\frac{dC}{dt} = \frac{3h}{1000} \qquad \text{[mm/min]} \quad (4.2)$$

In which h is the initial height of the test wall in [mm] once the load has been applied.

b) Integrity (E)

The integrity criterion is the time for which the specimen sustains its separating function during the test without allowing smoke, hot gases and fire to pass through the assembly [25]. The experimental procedure includes the ignition of a cotton pad or the

use of gap gauges to control openings during the test.

c) Insulation (I)

Insulation is the time that the LSF Wall continues to have its separating function without transmitting excessive heating to the unexposed side, limiting the average and maximum temperature. In accordance with EN 1363-1 there are two limits [25]:

$$\theta_{avg} \leq \theta_{avg,0} + 140 \quad \text{[K]} \quad (4.3)$$

$$\theta \leq \theta_{avg,0} + 180 \quad \text{[K]} \quad (4.4)$$

The Equation 4.3 defines that the increase of the average temperature θ_{avg} should not be 140 [K] above the initial average temperature ($\theta_{avg,0}$). In Equation 4.4 , the increase of the maximum temperature at, any location, should not be more than 180 [K] when compared with the initial average temperature ($\theta_{avg,0}$). The LSF Wall insulation is considered to be failed when the temperature reaches values of Equation 4.3 or Equation 4.4. The initial average temperature is the average temperature of the unexposed face at the begging of the test [25].

All the criteria are considered in the time domain, in which, allow to compare the values found in the fire resistance tests with the code-specified or national regulation fire resistance. Full-scale fire resistance test is considered better than cheaper small-scale tests because it is able to evaluate the effects of connections, shrinkage, deflections and gaps between lining materials [23]. However full-scales tests, as pointed before, are too expensive and for these reasons others methods may be developed to assess structural fire resistance: advanced and simplified calculations methods.

Chapter 5

Advanced Calculation Method to Estimate Fire Resistance of Load bearing LSF Walls

This chapter describes the development and validation of an advanced calculation method, using Ansys Mechanical APDL 18.2, to estimate the fire resistance of load bearing LSF Wall using a finite element model. For validation, the results obtained from the finite element model will be compared with a fire resistance test, chosen from references.

Advanced calculations methods (ACM) provide realistic predictions of structural behaviour and are cheaper than full-scale fire resistance tests, mentioned before [21]. In accordance with Eurocode 3 – part 1.2, ACM should include separate models to determine (1) the development and distribution of temperature (thermal response model), (2) the mechanical behaviour of the structure (mechanical response model) [26].These methods can be used to study the effects of different components, assemblies, material, section, and others characteristics on the fire behaviour of the LSF Wall and can be analysed with any heating curve, if there are material properties known for the temperature range.

For the thermal response, the model must consider, according with Eurocode 3 part

1.2, the relevant thermal actions specified in EN 1991 part 1.2 [22]. The mechanical response must consider changes of mechanical properties with temperature, the combined effects of mechanical actions, geometrical imperfections and thermal actions, and incremental and non-linear geometrical analysis [26].

Not all ACM require the use of finite element software, nevertheless, in this work, a finite element model will be developed to predict the fire behaviour of load bearing LSF Wall. However, all advanced calculation needs validation and should be done by checking the accuracy based on test results, in which, refers to (1) temperature, (2) deformations and (3) fire resistance times [26]. For the developed method of this thesis, validation will be done comparing with tests results from Gunalan and Mahendran [7], [13].

5.1 Development and validation of a finite element model

In this thesis, the loadbering LSF Wall assembly to be validated is the test specimen "7" made by Gunalan and Mahendran in 2013 [7]. The simulation consist in four steps: (1) Elastic buckling analysis; (2) Load bearing capacity at room temperature; (3) Non-linear thermal transient analysis and (4) Thermomechanical analysis. More details are showed in the scheme from Figure 5.1.

The full-scale fire resistance test was validated using finite element model by the same authors, in which, a single stud was simulated representing the whole structure, thus this finite element simulation will be accounted as well [13]. Some extra information needed was taken from Gunalan thesis from 2011 [2]. A representation of the LSF Wall assembly is shown in Figure 5.2.

The frame was made from G500 galvanized steel sheets with 1,15 [mm] thickness and were built with 2400 [mm] height and 2100 [mm] width. The LSF wall has four studs (90 x 40 x 15 x 1,15 [mm]) spaced every 600 [mm] from each other, made with lipped C cross sections and two tracks (92 x 50 x 1,15 [mm]) made of un-lipped section. The structure is

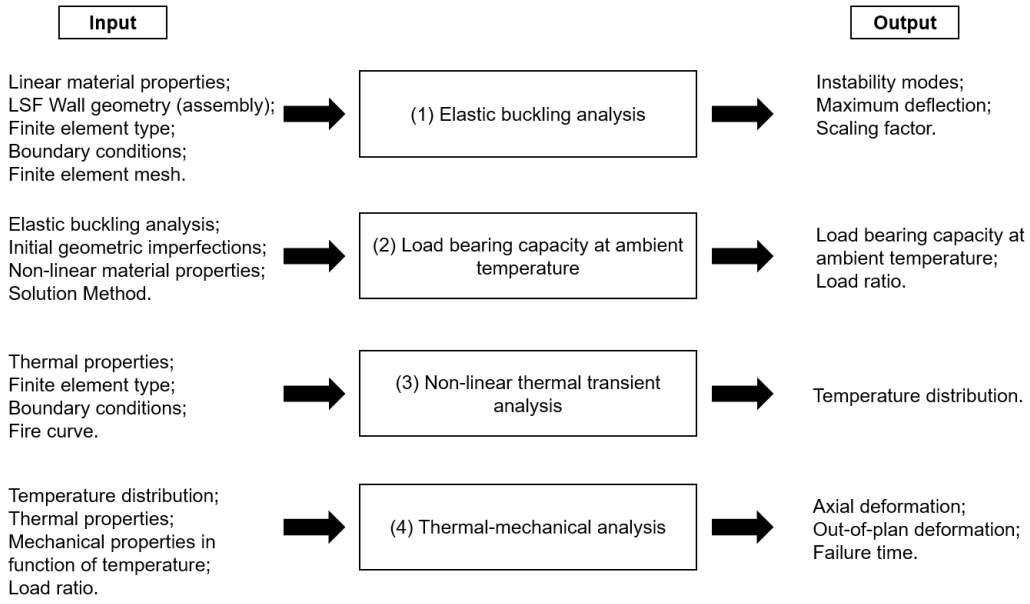

Figure 5.1: Simulation steps.

lined with two layers of plasterboard in both sides, with 16 [mm] thickness built 1200 [mm] in width and 2400 [mm] in length. Between the plasterboards, an external insulation was formed, filled with 25 [mm] glass fibre insulation. An upper view of the assembly is shown in Figure 5.3, more information and the drawings of this wall is present in Appendix A.

5.2 Mechanical analysis under room temperature

The mechanical analysis under room temperature can determine the critical loads and the ultimate load of the structure. The elastic buckling load represent the critical loads (P_{cr}) when the LSF wall become unstable (assuming that the element and material are both perfect). The ultimate load is the maximum load that the structure can hold under room temperature. The elastic buckling is an abrupt shape change in structural members under a certain load level as in members under compression, like LSF walls. In these walls, the studs are under compression, and can bow if the load is gradually increased and reaches critical level, at this point, the structure takes on a shape associated to the load and assume a buckled condition.

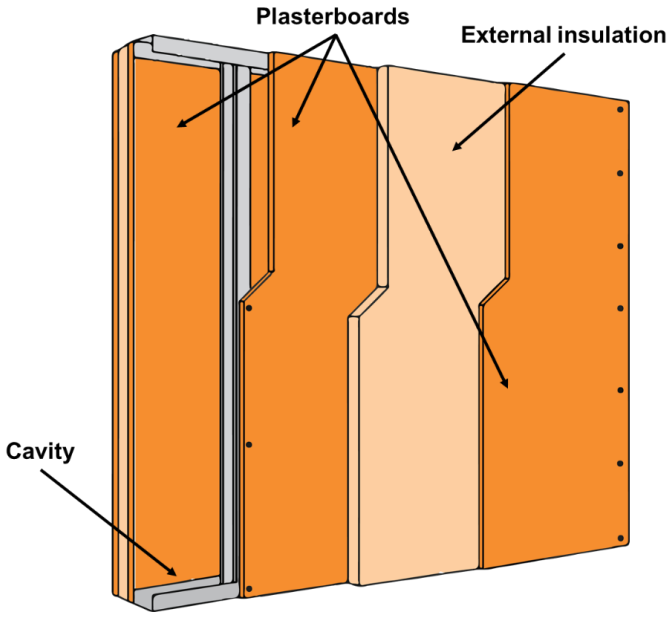

Figure 5.2: LSF Wall representation.

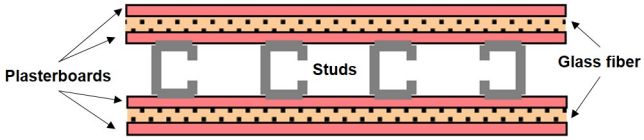

Figure 5.3: Upper view of the LSF Wall (Modified from [2]).

The determination of the elastic buckling loads are important when designing the LSF wall, because buckling may occur in stress levels way bellow of the level needed to cause structure material to fail. After reaching the buckling load, the structure become unstable and can lead to complete loss of the load bearing capacity of the wall. In finite element model, the elastic buckling analysis is the method used to determine the elastic critical buckling loads.

5.2.1 Elastic Buckling Analysis

Elastic buckling analysis uses the eigen-value theory to determine the buckling load of the LSF wall, it can predict theoretical buckling load of an ideal elastic structure by calculating the eigen-values for the system load and constraints. This method is known

as classical Euler buckling analysis. Each eigen-value has a buckling load associated, one of them is the critical load, in which, represent the most likely load to cause the structure to buckle.

In Ansys, this analysis is made in two steps: first a static linear simulation is conducted applying a reference load F_{ref} and then the eigen-values are extracted using Block Lanczos method. When the boundary conditions (constraints) and linear material properties are set, a linear system of equation is formed as in eq. 5.1.

$$[K_0] \cdot \{d\} = \{F_{ref}\} \tag{5.1}$$

In which, K_0 is the global stiffness matrix and d is the displacement vector. In this system of equation, K_0 is determined by the material properties and constrains set, F_{ref} is the load applied to the model, assumed to be unitary, 1 [N], in this work.

As pointed before, the buckling is the point where the structure starts to become unstable and this happens due to the compressing forces, in which, causes the global stiffness matrix of the structure, K_0, to decrease. When K_0 approaches zero, the structure displacement increases quickly until reaching the point that the internal and external forces are in unstable equilibrium.

When the static linear simulation finishes, the displacement vector d can be determined and the stress field can also be determined for the reference load, F_{ref}, which enable to generate the stress stiffness matrix: $K_{\sigma,ref}$. Both F_{ref} and $K_{\sigma,ref}$ are proportional, so, a new load vector and stress stiffness matrix can be defined in function of $F_{ref}/K_{\sigma,ref}$ with a proportional constant λ ($\{F\} = \lambda\{F_{ref}\}$ and $[K_\sigma] = \lambda[K_{\sigma,ref}]$). The stiffness matrix does not change in function of the F_{ref} because it is linear.

Still, the critical buckling load can be determined in function of the F_{ref} by considering the λ_{cri}, the multiplier value for the buckling load. Thus, a relation between the stiffness matrix, displacement and critical load can be developed as shown in eq. 5.2.

$$[[K] + \lambda_{cri}[K_{\sigma,ref}]] \cdot \{d\} = \lambda_{cri}\{F_{ref}\} \tag{5.2}$$

Buckling definition is the quick change in displacement under the effect of the same load, therefore, an incremental displacement, δd is applied, resulting in eq. 5.3.

$$[[K] + \lambda_{cri}[K_{\sigma,ref}]] \cdot \{\{d\} + \{\delta d\}\} = \lambda_{cri}\{F_{ref}\} \tag{5.3}$$

At each iteration, the software applies a displacement δd on to the structure until it is not possible to maintain static equilibrium, defined by eq. 5.4.

$$[[K] + \lambda_{cri}[K_{\sigma,ref}]] \cdot \{\delta d\} = 0 \tag{5.4}$$

There are several instability modes (λ) associated to loads ($\{F\} = \lambda\{F_{ref}\}$), however, the lowest of them it is usually considered the most critical, because is this one that the structure will reach first and most likely to fail before reaching any other mode. Thus, with the d known from linear simulation, in the second step analysis, Ansys will extract the vectors for the eigen modes, solving the homogeneous equation, extracting them using block Lanczos method, with incremental buckling displacement vector, δd.

5.2.2 Element type

For the simulations under room temperature, the element shell 181 was used. This is a fully Gauss integrated element with four nodes (I, j, k, l) containing six degrees of freedom in each node: translation in x, y and z directions, rotation about x, y and z-axes. The shell 181 is suitable for linear, large rotation and large strain nonlinear applications, the element geometry is shown in Figure 5.4 [27].

For full integration applications, this element has four Gauss integration points in-plane and up to nine trough thickness. In this work, this element was used as full integration with five integration points through thickness as shown in 5.4. This element uses linear interpolation functions for translations and rotations [27].

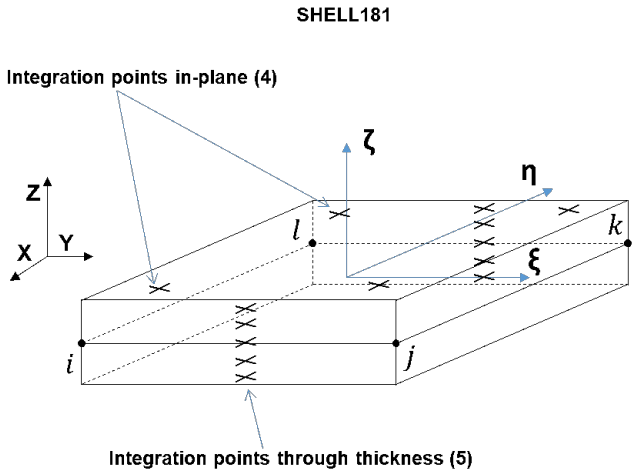

Figure 5.4: Shell 181 element geometry (Modified from [27]).

5.2.3 Mechanical properties

In finite element analysis, the use of corrects mechanical properties are fundamentals, because these properties define the material behaviour, therefore, the structure behaviour when submitted to loads. The mechanical properties are defined by the constitutive law used for the stress-strain, by the elastic modulus and by the poisson's ratio.

The LSF wall was made by G500 galvanized steel sheets with 1,15 [mm] thickness and its mechanical properties were determined based on tensile coupon tests [7]. At room temperature, the measured yield strength was 569 [MPa] and an elasticity modulus of 213,520 [GPa] [7].

Finite element analysis can be simulated with different models for the constitutive law, such as elastic-perfect-plastic, in which, assumes constant yield stress in all plastic range and strain hardening model that accounts the strain hardening in the inelastic phase. The results obtained from the test developed by Gunalan, Kolarkar and Mahendran [7], showed the existence of presence of strain hardening. The graph of 5.5 presents the difference for the stress-strain models that can be used.

Even though both models are suitable for the finite element model (FEM), the simplest one is desirable since it will be less time and memory consuming that a more complex model. However, there is a need to verify if the simplified model is capable of representing

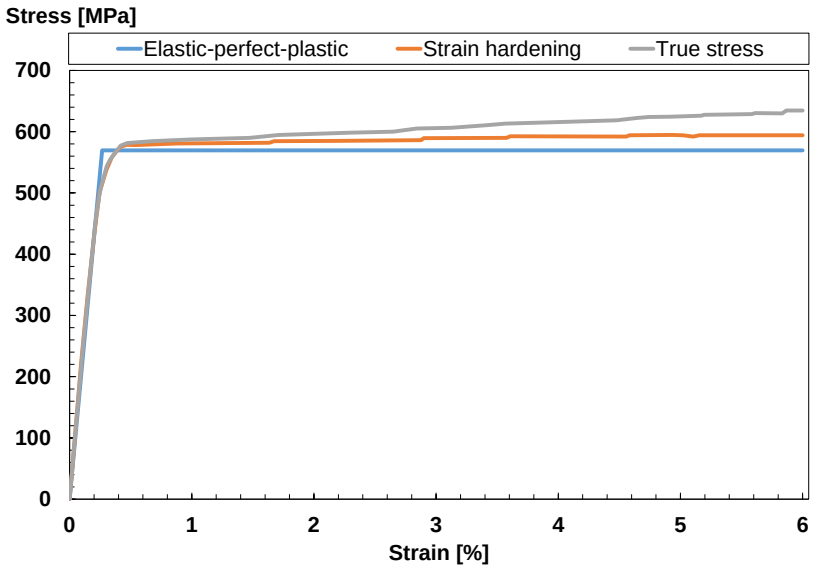

Figure 5.5: Comparison of different stress-strain models (Modified from [2]).

the material behaviour since the tests showed, clearly, strain hardening as shown in Figure 5.5.

Additionally, another analysis was proposed by Gunalan, Kolarkar and Mahendran, where the true stress and logarithmic plastic strain [13], [2], [7] has been used, instead of engineering stress-strain obtained from the coupon tests (see Figure 5.5). The true stress takes in to account the "necking", which represents the effect of cross-section changes during the test, while engineering stress assumes a constant cross-section (original one). To convert engineering stress strain (σ_{eng} and ε_{eng}) to true stress and logarithmic plastic strain values (σ_{true} and ε^{pl}_{true}) the equations 5.5 and 5.6 should be applied.

$$\sigma_{true} = \sigma_{eng} \cdot (1 + \varepsilon_{eng}) \qquad \text{[MPa]} \quad (5.5)$$

$$\varepsilon^{pl}_{true} = ln(1 + \varepsilon_{eng}) - \frac{\sigma_{true}}{E} \qquad (5.6)$$

Table 5.1: Comparison of plasticity models for room temperature.

Model	U [kN]
Elastic-perfect-plastic	78,8
Strain hardening	79,2
True stress	80

Where E is the elasticity modulus. A comparison of the nonlinear simulation was made using the elastic-perfect-plastic model, the strain hardening and the true stress calculated by the equations 5.5 and 5.6 The results for the ultimate load (U) are in Table 5.1.

All three cases resulted in similar values, strain hardening and elastic-perfect-plastic were closer to the test result, 79 [kN] [7]. Elastic-perfect-plastic model was chosen to be used in the finite element model, due to the fact that it is less complex than strain hardening model and results are in good agreement with test ultimate load (relative error 0,25%). The difference found between the three cases, could have been caused due to the 1% convergence tolerance set for the simulations.

5.2.4 Finite Element Mesh

The finite element mesh is an important step in the finite element analysis (FEA) because the accuracy of the results from FEA is directly related to the mesh. The mesh determines the quantity of elements, therefore, number of nodes in the model. Each element has set of equations that are assembled and the sum of all these elements approximate the behaviour of the structure. For this reason, as the element size gets smaller or bigger the approximation to the true solution is changed: small elements will drive the solution to the real value. However as small as the mesh size is, more computational resource and time is required.

Overall, the mesh size depends on the system to be analysed: the geometry and the physics involved in the process. Materials properties, constrains, load and others variables, that can affect the system, should be taken in consideration in order to define the mesh. Normally, in the first simulation, a coarse mesh is used with relatively big elements to analyse the response of the structure. A coarse mesh will not require too much time

and computational resources, but probably the results are not good. This preliminary simulation can be used to verify if all the boundary conditions and materials properties are well defined. From this point on, the mesh needs to be refined: relatively smaller elements are defined and then the simulation is made again.

5.2.5 Boundary conditions

The finite element model should be able to simulate the boundary conditions set during the test such as restraint against expansion, contraction or rotation, appropriated loading in the LSF wall. These boundary conditions have to be in accordance with the LSF wall.

In Gunalan work, the load was applied by a hydraulic jack in each stud and pinned conditions were used in the test. A loading plate were used to transfer the load to the studs via their geometric centroids [2] (see Figure 5.6).

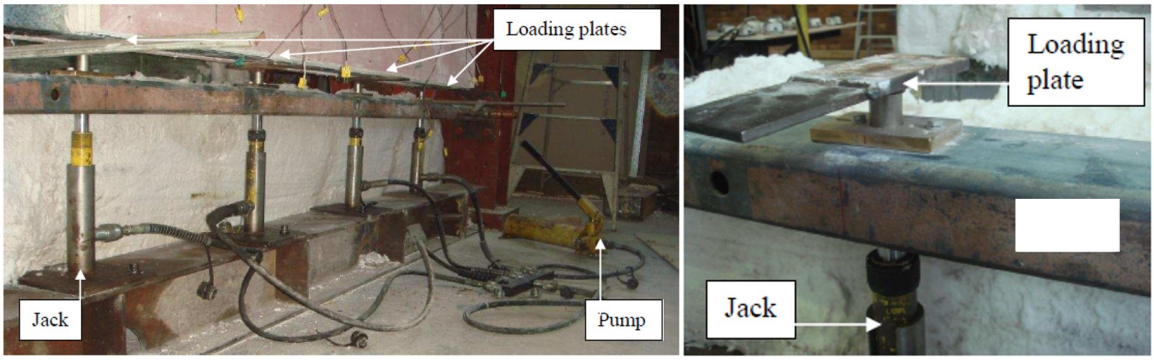

Figure 5.6: Loading plate used during test [2].

To represent the upper restriction caused by restraining the wall into the furnace, the top nodes from the top track were restrained in $u_x = u_y = u_z = Rot_z = 0$. On the connection between the tracks and the studs, a double thickness has been used, with 2,30 [mm] (two times the nominal) to avoid complex joint simulation model. Still, in the middle of this interface, a restrain in the u_x was applied to simulate the screw connection between both elements (stud and track).

A horizontal restrain has been applied on the vertical studs, $u_x = 0$, to simulate the connection of steel stud and the plasterboard, spaced every 300 [mm] along the length.

In the simulation under room temperature the plasterboard was not included, only the restriction caused by it has been considered. The horizontal restrain in the stud due the plasterboard, and in the interface between stud and track were applied both studs' sides. All the restraining can be seen in Figure 5.7 and Figure 5.8.

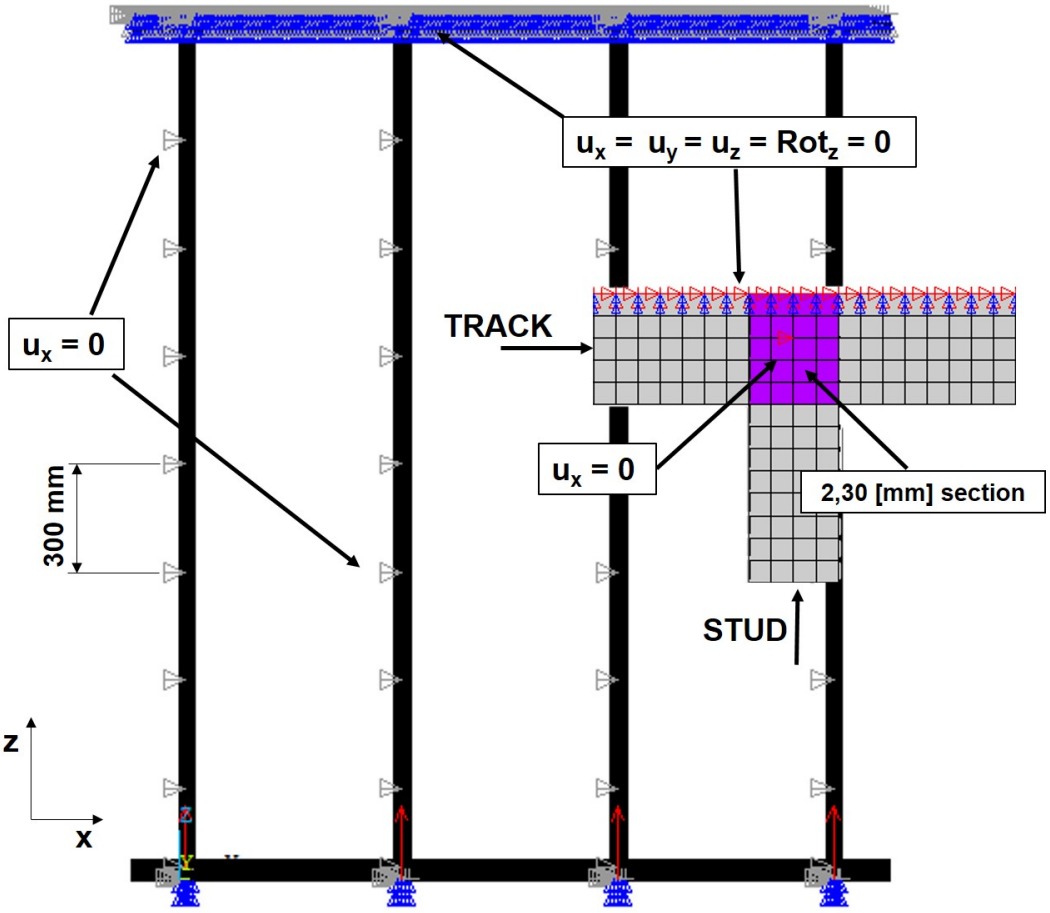

Figure 5.7: Restrains applied in the top track and in the interface between tracks and studs.

The load has been applied in the bottom track, using the centroid of each stud. To make sure that the load was well distributed a rigid plate was created with E = 2100 [GPa] and boundary condition (B.C.) of $u_x = u_y = Rot_z = 0$. The B.C. were applied in two different cases: at the node of force node (F_a) and at studs bottom area (A_s), see Figure 5.9. The rigid plate was used to distribute the load and not to give additional stiffness to the wall, therefore, different plates thicknesses were investigated, giving different results,

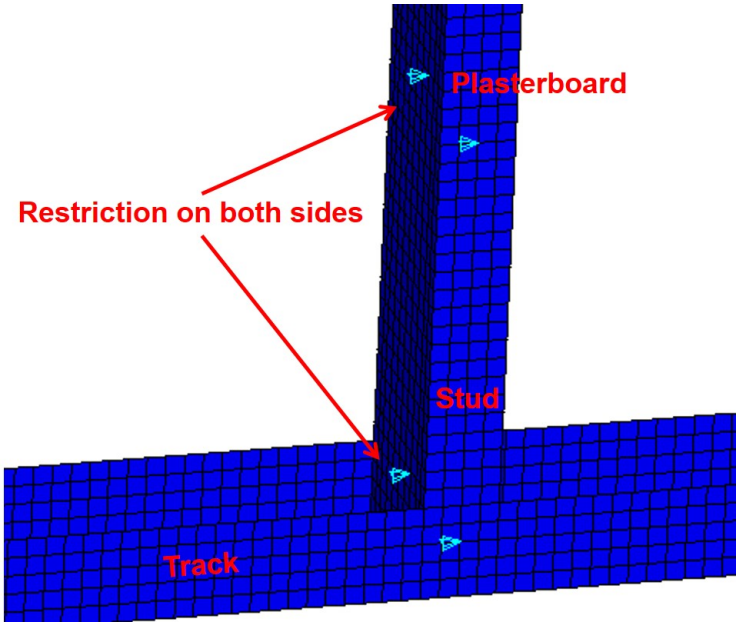

Figure 5.8: Connection between the stud and plasterboard the connection between the stud and track.

see Table 5.2.

Results from Table 5.2 showed that the thickness does not have any significant influence in critical load (P_{cr}), however, it has big effect in the ultimate load. For all simulations, the 13 [mm] thick plate with boundary conditions at stud bottom area has been identified with the best result.

5.2.6 Initial geometrical imperfections

Cold-formed steel are likely to have initial geometric imperfection due the process of manufacturing and because they can also deform during handling and assembling. Geometrical imperfections are a deviation of the member from a "perfect" geometry, which may include bowing, warping, twisting or local deviations. According to Schafer and Peköz (1998), there are two categories of geometric imperfections: type 1, maximum local imperfection in a stiffened element and type 1, maximum deviation from straightness for a lip stiffened or unstiffened flange, represented in Figure 5.10 [28].

Where, in Figure 5.10, d_1 and d_2 are the maximum geometric imperfection in the web

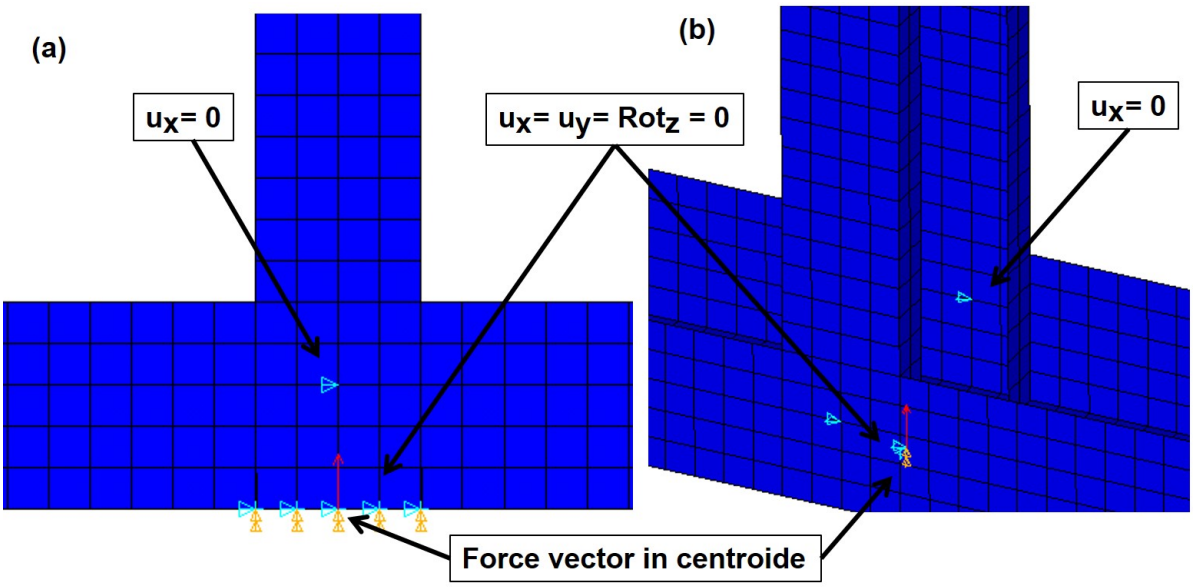

Figure 5.9: (a) A_s boundary application and (b) F_a boundary application.

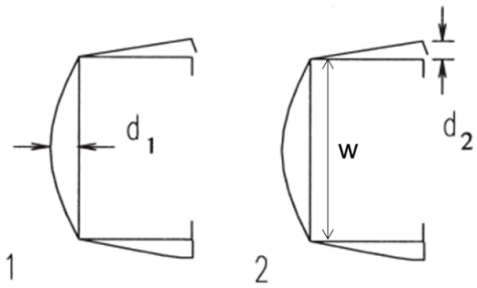

Figure 5.10: Geometric imperfections, type 1 on the left and type 2 on the right (Modified from [28]).

and flange, respectively and w is the stud width. In this work, only the d_1 imperfection will be considered and the amplitude of it, according to Schafer and Peköz, is given by eq.5.7 [28].

$$d_1 = 0.006 \cdot w \qquad \text{[mm]} \quad (5.7)$$

The strength of a cold-formed steel member is sensitive to the geometric imperfections. The maximum amplitude of the web buckling mode has been used to define the imperfections [28].

Table 5.2: Critical and Ultimate load for different B.C. and plate thickness.

B.C.	Thickness [mm]	P_{cr} [kN]	U [kN]	Relative error [%]	
–	–	39,8*	79**	–	–
A_s	30	39,92	85,65	0,3	7,76
F_a	30	39,87	88,59	0,2	10,82
F_a	20	39,85	88,40	0,1	10,63
A_s	15	39,85	86,20	0,1	8,14
F_a	15	39,82	85,73	0	7,85
A_s	14	39,83	84,75	0	6,78
F_a	14	39,83	81,31	0	2,84
A_s	13	39,83	78,89	0	0,13
A_s	12	39,80	66,20	0	16,2
F_a	10	39,80	53,4	0	32,4

*: FEM results taken from: [13]; **:Test results taken from: [7].

In finite element model, the imperfection with d_1 amplitude has been applied to the non-linear model using a scale factor showed in equation 5.8. This scale factor has been applied to define a new position for the nodes of the structure.

$$s_f = \frac{d_1}{u_{x,max}} \tag{5.8}$$

Where, $u_{x,max}$ is the maximum displacement in d_1 horizontal direction, obtained from the requested instability mode. The maximum geometric imperfection, d_1, for the LSF wall is 2,4x10^{-4} [mm].

The initial geometric imperfection is applied in Ansys through the option "updated geometry", using the adequate mode (usually the lowest) from the five modes extracted of the elastic buckling analyses, using the scale factor calculated by equation 5.8.

After applying the imperfections, the next step is to run the simulation with incremental load, using a solution method.

5.2.7 Mesh convergence

In the model developed, a convergence test was made with elements of size: 10, 8, 6 and 4 [mm], the results are shown in the Table 5.3. Another 2 [mm] element size model was developed, however, the hardware settings available were not capable of processing the finite element model. Since 4 [mm] element agreed well with test results, as Table 5.3 shows, this mesh model has been considered to have converged in respect to the mesh.

Table 5.3: Mesh convergence test.

Element Size [mm]	P_{cr} [kN]	U [kN]
Test (no elements)	39,8*	79**
10	40,76	85,55
8	40,33	81,72
6	40	80,66
4	39,8	78,89

*: FEM results taken from: [13]; **:Test results taken from: [7].

5.2.8 Solution method

After the elastic buckling analysis, the load bearing capacity at room temperature was evaluated. This analysis is conducted to determine the axial compression load bearing capacity, that the LSF Wall can hold at room temperature, considering the geometric imperfections, presents from the manufacturing process and the non-linear behaviour of the materials.

This simulation consists in using the mode of instability from the previous elastic buckling analysis to apply an initial geometric imperfection to the model. The non-linear material properties shown in 5.2.3 were also considered.

In order to model the real experiment, where the hydraulic jack applies the load during the fire test, the load was applied using an incremental value. In each increment, the software will try to stablish equilibrium in the structure using a pre-defined solution method. If at certain time, therefore, a certain load, the equilibrium is no longer sustained, and the structure is considered to have failed (failure by loss of equilibrium may be different

from failure by any of other criteria defined for displacement or rate of displacement). This load and the displacement have to agree with test results, then the model can be validated.

Two solution methods are going to be discussed in this work: Newton Raphson and Arc-Length method.

5.2.8.1 Newton Raphson method

The Newton Raphson method guarantees convergence in few interactions and is largely applied in FEA software, it is ideal when solving larger systems of non-linear equations [29]. In this method, the external load, F^{ext} is increased, using a scalar λ, from 0 until it reaches the desired value. In a generalized case, in which, the system of equation is not in equilibrium, the residual vector is given by eq. 5.9 [29].

$$R(u) = F^{int}(u) - F^{ext} \Rightarrow R(u) = F^{int} - \lambda \cdot F^{ext} = 0 \tag{5.9}$$

Where R(u) is the residual vector and changing the magnitude of λ the load is increased or decreased. At each increment, i, of λ, the eq. 5.9 is solved to determine u. Assuming that the last converged solution is u_0, λ_0, the load increment is calculated using eq. 5.10.

$$\lambda' = \lambda_0 + \Delta\lambda \tag{5.10}$$

Therefore, the displacements are given by eq. 5.11.

$$u' = u_0 + \Delta u \tag{5.11}$$

So equation 5.9 is updated to equation 5.12.

$$R(u') = R(u_0 + \Delta u) = 0 \Rightarrow F^{int}(u_0 + \Delta u) - (\lambda_0 + \Delta\lambda)F^{ext} = 0 \tag{5.12}$$

However, $F^{int}(u_0 + \Delta u)$ can be expressed in terms of $F^{int}(u_0)$ using Taylor expansion series. Excluding the other terms from the expansion, the expression is given by eq. 5.13.

$$F^{int}(u_0 + \Delta u) = F^{int}(u_0) + \left[\frac{\partial F(u)}{\partial u}\right] \cdot \Delta u = F^{int}(u_0) + [K_T]_{u_0} \cdot \Delta u \tag{5.13}$$

In which, $[K_T] = [\frac{\partial F(u)}{\partial u}]$ is the Jacobian matrix, also known as the Tangential Stiffness Matrix [29]. Combining equations 5.12 and 5.13 is possible to solve Δu using eq. 5.14.

$$F^{int}(u_0) + [K_T]_{u_0} \cdot \Delta u - (\lambda_0 + \Delta\lambda)F^{ext} = 0 = F^{int}(u_0) - \lambda_0 F^{ext} + [K_T]_{u_0} \cdot \Delta u - \Delta\lambda F^{ext}$$
$$\Rightarrow \Delta u = [K_T]_{u_0}^{-1} \cdot (\Delta\lambda F^{ext}) \tag{5.14}$$

When equation 5.12 is solved for Δu (from eq. 5.14) a non-zero residual vector R'(u') will be obtained. Through this vector a new displacement correction, δu, is calculated by eq. 5.15 [29].

$$\delta u = [K_T]_{u'}^{-1} \cdot R'(u') \tag{5.15}$$

In this way, a new displacement correction is determined and can be applied in equation 5.12 that will generate a new and smaller residual vector R'(u"). This is repeated until the norm of the vector is less than the tolerance versus the R_{ref} (residual reference vector), $\varepsilon \cdot R_{ref}$ [29].

In Ansys, the norm can be calculated in three different ways: infinite norm, L1 norm and L2 norm. For all the simulations the L2 norm has been used, in which, consider the square root of the sum of the squares values of the terms: $|R| = (\Sigma R_i)^{1/2}$. For the reference (R_{ref}), the value is taken by the norm of the external force, $|F^{ext}|$, however for DOF that has displacement constrains, the reference is taken as $|F^{int}|$. Still, in some cases Ansys will assume a minimum value for the R_{ref}, selected as 1,0 for all the simulations [27].

The tolerance, ε was settled as 0,01 (1%) for all simulations. The time at the end of solution was defined as 100000 [N], incremental load with minimum 1 [N], normal 100 [N]

and maximum 1000 [N].

The steps for an iteration (i) are:

(0) Step 0: $\Delta\lambda$ is defined between the maximum and minimum values pre-defined;

(1) Step 1: Compute the Stiffness matrix (Jacobian);

(2) Step 2: Solve equation 5.12 to find Δu;

(3) Step 3: Check if $|R'(u')| < \varepsilon_{ref}$, if not go to step 5;

(4) Step 4: Go to the next iteration (i+1);

(5) Step 5: Calculate δu using equation 5.15 with R'(u');

(6) Step 6: Solve equation 5.14 using $R(u_0 + \Delta u + \delta u)$;

(7) Step 7: Check if $|R'(u'')| < \varepsilon_{ref}$, if not, go to step 5, if yes, go to step 4.

This process will be repeated until the solution is found, in general, it is when the solver can no longer find equilibrium in the structure. A generic example of how Newton method's works is represented in the graph of Figure 5.11.

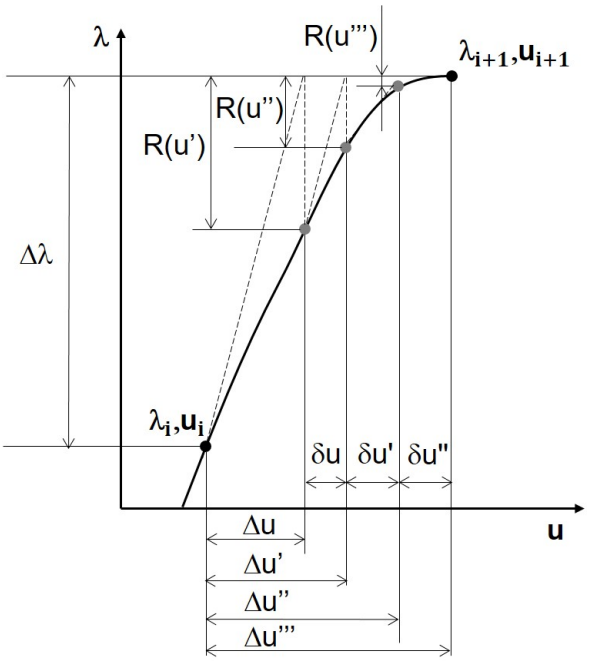

Figure 5.11: Newton-Raphson Method with load increment (Modified from [29]).

Newton-Raphson provides fast convergence and is able to solve, with efficiency, any

set of non-linear equations from a mechanical system until it reaches the critical point [29]. However, this method fails to follow the equilibrium path once the stiffness matrix reaches zero, which means that this method does not accept values of λ_i minor than λ_{i-1}. This happens because in the formulation of the method, shown above, the load, λ, does not change its loading pattern, that is, it changes monotonically in each increment (always increasing). This case can better seem in Figure 5.12.

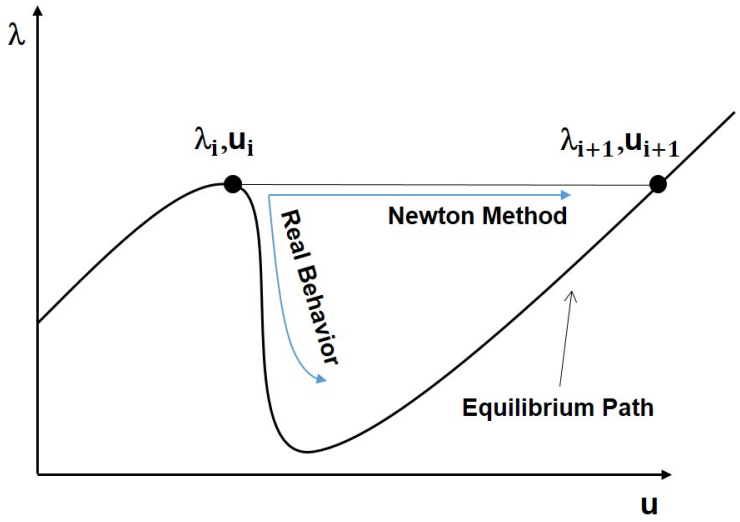

Figure 5.12: Newton-Raphson method fails to predict the equilibrium path (Modified from [29]).

This is a problem when structures have Snap-Through behaviour (shown in Figure 5.12), in which, the load λ_i is smaller than λ_{i-1}. However, in these cases a solution is to apply the Newton-Raphson method with incremental displacement, u, because it will continuously increase and u_i will be larger than u_{i-1}, thus being able to follow the equilibrium path [29].

Still, there are cases that the structure goes under Snap-Back behaviour, in which, the u_i is smaller than u_{i-1}, so, the solution will not be able to follow the equilibrium path. Some cases, the system can undergo both behaviours, where, the Newton-Rapshon method using load or displacement increment could not be applied. The main problem is that the structural response of the system (the equilibrium path) is, in general, unknown, meaning that the behaviours cannot be expected. For these cases there is no guarantee that

Newton-Raphson method will represent the equilibrium path [29]. So, another solution method must be applied, such as the Arc-Length method.

5.2.8.2 Arc-Length method

The Arc-Length method uses the same principles as the Newton method, however, instead of interpolating to find Δu using a known $\Delta\lambda$, the method postulates a simultaneous variation in both, that is, Δu and $\Delta\lambda$ are unknown.

So, applying the variation of u and λ (equations 5.10 and 5.11) to the equilibrium equation from 5.9), the new residual vector is given by 5.16 [29].

$$R(u', \lambda') = F^{int}(u_0 + \Delta u) - (\lambda_0 + \Delta\lambda)F^{ext} = 0 \tag{5.16}$$

If 5.16 is satisfied for the variables $u_0, \Delta u, \lambda_0, \Delta$ then the solution for that iteration is done and the next one starts. But, not all times this is possible, as result, it has to be correct by adding δu and $\delta\lambda$ and the new equation will be 5.17.

$$R(u'', \lambda'') = F^{int}(u_0 + \Delta u + \delta u) - (\lambda_0 + \Delta\lambda + \delta\lambda)F^{ext} = 0 \tag{5.17}$$

Using Taylor expansion and keeping only the linear terms, the equation results in 5.18 [29].

$$-R(u', \lambda') = [K_T]_{u_0+\Delta u} \cdot \delta u - \delta\lambda \cdot F^{ext} \tag{5.18}$$

However, this equation has more unknown variables than equation, which means, that this system cannot be solved. There are different approaches to solve this case, but, the method used by Ansys will be discussed. In this method, the u is given by equation 5.19 [27].

$$\delta u = \delta\overline{u} + \delta\lambda \cdot \delta u_t \tag{5.19}$$

In which, $\delta\overline{u} = [K_T]^{-1}_{u_0+\Delta u} \cdot R(u', \lambda')$ and $\delta u_t = [K_T]^{-1}_{u_0+\Delta u} \cdot F^{ext}$. To solve for $\delta\lambda$, the

software uses the norm of a vector t, that represents the distance between the previous equilibrium point and the next point to be solved [27]. This vector t varies from a maximum and minimum range pre-determined. The graphical representation of the method is shown in Figure 5.13.

The size of the arc in blue (see Figure 5.13) is determined by the norm of the vector t and is constant during all the sub steps that the solver needs to work in order to advance to the next equilibrium point (i+1). So, the norm of t and t' and so on, are numerically equal, but, the vector itself is not the same, because for each sub step, the value of u and λ are corrected by δu and $\delta\lambda$. The solver can go to any point inside the radius of the circle and if it is not capable of finding the solution, then, the software will change t according to the max and min value determined.

The difference between arc-length and Newton method is clearly seen by comparing the Figure 5.11 with Figure 5.13: in the arc-length there are corrections for the load and displacement, but in Newton method both corrections do not happen simultaneously.

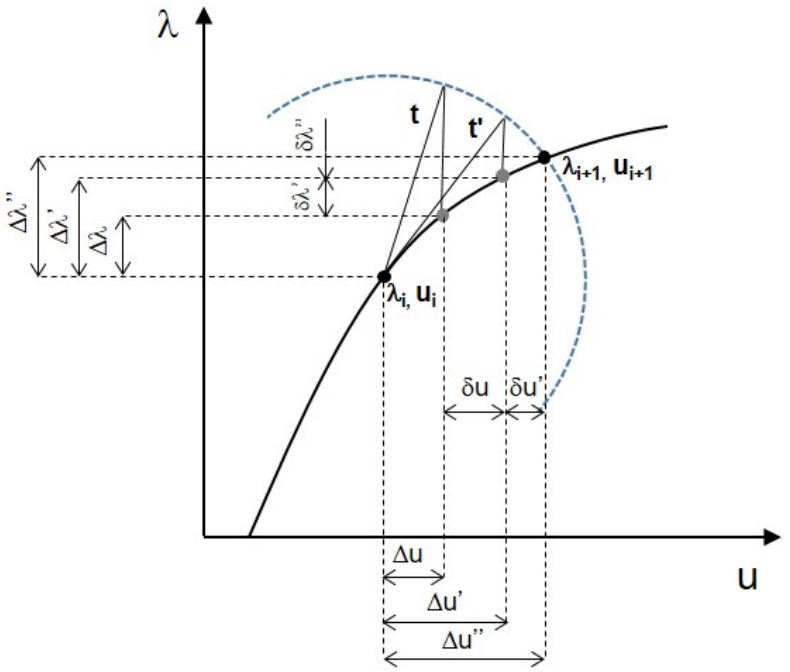

Figure 5.13: Arc-Length method in a graphical representation.

At each iteration between two equilibrium points, the software solves equations 5.18 and 5.19 to determine $\delta\lambda$, in order to update the variations of u and λ. Then the software applies both in 5.17 and check the convergence, if the norm of R is less than the tolerance, the solution goes to the next iteration (i+1), if not, then it starts all over by solving equations 5.18 and 5.19, so that, the next sub step (represented by the use of apostrophe in Figure 5.13) until it reaches the point of not being able to find equilibrium in the system.

However, this process is high time and memory consuming, in which, does not justify its application in some simulations. In this work, the main focus will be to use the (1) Newton-Raphson method using force increment to determine the ultimate load, (2) Newton-Raphson method using displacement increment to determine the structure behavior (if possible).

5.3 Thermal analysis under fire

The finite element analysis under fire condition (thermal simulation) includes a transient simulation, that takes in to account the thermal loads and others boundaries conditions from full scale fire test. In these simulations, the materials properties are temperature dependents and the fire curve is applied in order to obtain the temperature distribution in respect to time. This solution step is uncoupled from the mechanical analysis, because it is assumed that the strain rate is small and does not consider any modification in the material temperature.

The main objective of the finite element analysis under fire condition is to find the temperature profile and compare with the full-scale fire tests results. Then, these profiles are, later on, applied in to a new structural simulation, in which, will assess the structural load bearing capacity of the wall during a fire event.

5.3.1 Element Type

In the thermal simulation two elements type were used: shell 131 (applied in the LSF structure) and solid 70 (applied in the plasterboards and insulation material).

Shell 131 is the equivalent of the shell 181 previous applied in load bearing and eigen buckling analysis, but all degrees of freedom are modified to include the temperature. This element consists in a 3D layered shell in which has in-plane and trough thickness thermal conductivity capacity. It can be used in steady-state or transient thermal analysis and the element has capability of generating temperatures that can be transferred to shell elements for modelling thermal bending [27].

The shell 131 is a fully integrated element made by layers, with four nodes having a maximum of 32 temperatures degrees of freedom (DOF) per node. This element has four integration points in-plane and up to nine trough thickness, but five were chosen to be used in the simulations as shown in 5.14. This element presents linear interpolation functions [27].

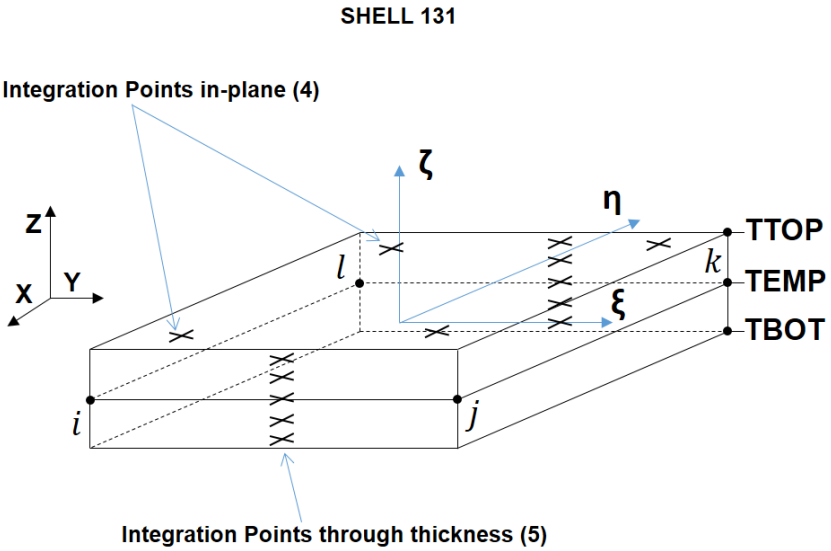

Figure 5.14: Shell 131 geometry (Modified from [27]).

The temperature variation was determined to be linear through layers (thickness), having in the bottom face the temperature denoted as TBOT and temperature on top of each layer named TE2, TE3 (represented with TEMP in Figure 5.14), ..., up to TTOP.

This element can have 31 layers and every single one of them has a TE degree of freedom. The number of layers was settled one (by default), implying two degrees of freedom: TTOP and TBOT (see Figure 5.14) [27]. Still, the paint option has been selected for this element, in which, makes TBOT to be replaced for another degree of freedom: TEMP, this configuration allows the element to be attached to a finite solid element avoiding the use of constrains equations, see Figure 5.15.

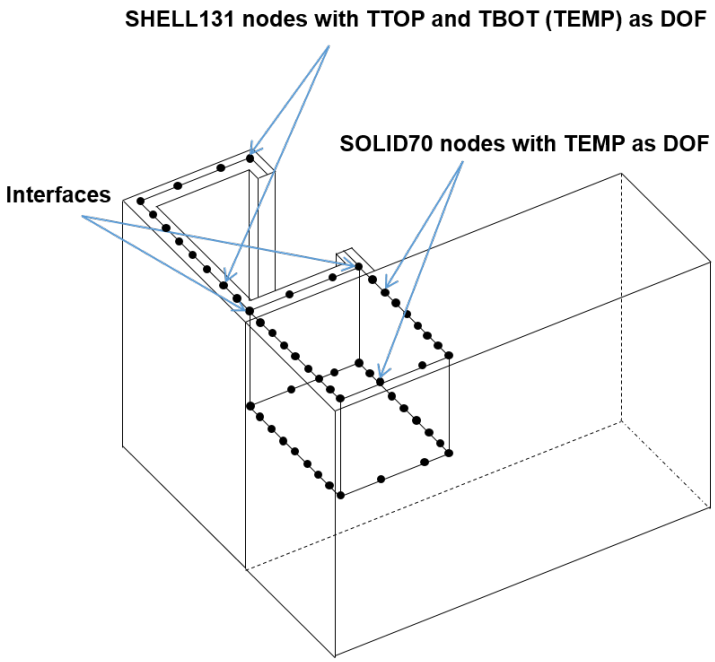

Figure 5.15: Contact between a shell finite element and a solid finite element.

Figure 5.15 shows an example of the contact between a shell 131 finite element and a solid 70 finite element. In the interface, temperature TEMP from shell matches the temperature DOF from solid element, that is, TEMP. Thus, this condition implies no need of any kind of master and slave option, in which would generate a much more complex model.

The solid 70 is a 3D and fully integrated element with three dimensions thermal conduction capability. This element has eight nodes with one degree of freedom, temperature (TEMP), at each node. It can be applied to steady-state or transient thermal analysis. The element geometry is represented in Figure 5.16 [27].

The solid 70 finite element has eight Gauss integration's points, distributed as shown in Figure 5.16.

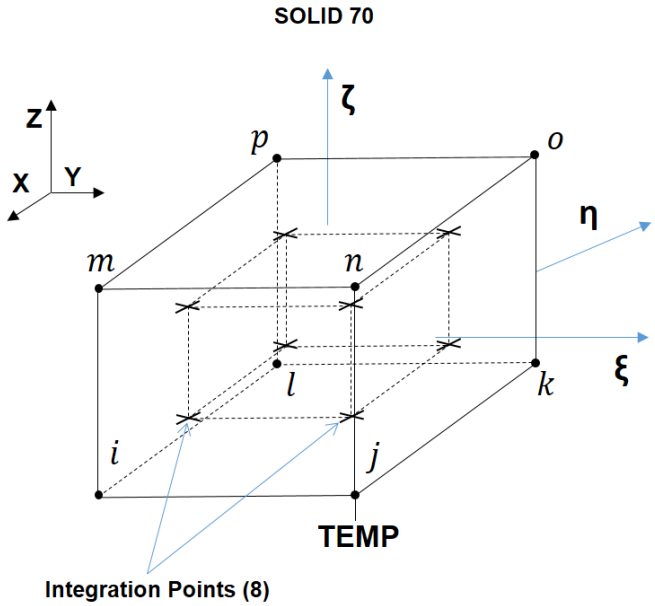

Figure 5.16: Solid70 element geometry (Modified from [27]).

5.3.2 Thermal Properties

Thermal properties are very important and their temperature dependence must be considered for the simulation due to their influence in the structure behaviour. Steel and other materials can change both material properties with temperature. Besides that, the EN 1991-1.2 indicates a structural fire analysis should take into account the material properties variation in accordance with EN 1993-1.2 [22], [26]. Namely they are: stress-strain relationship (in which includes yield strength and elastic modulus), emissivity, specific heat and thermal conductivity. Density is considered constant. The properties related to the mechanical behaviour will be considered in the thermomechanical analysis (see 5.4.2).

For the steel, in all the simulations, emissivity, ε_m, will be taken as 0,7 in accordance with EN 1993-1.2 [26], specific heat and thermal conductivity will be considered in conformity with EN 1993-1.2 [26] and are presented in Appendix B.

The insulation's materials, plasterboards (gypsum) and glass fibre, the properties are presented in Appendix B and were taken from [30].

5.3.3 Finite element mesh

For this simulation, the plasterboards and external insulation were added to the steel structure (see Figure 5.17). A 10 [mm] mesh was applied in the whole structure. In the tests, plasterboards were applied to the wall by joining three gypsums pieces: left, middle and right piece, but in FEA model the plasterboard was considered as one piece.

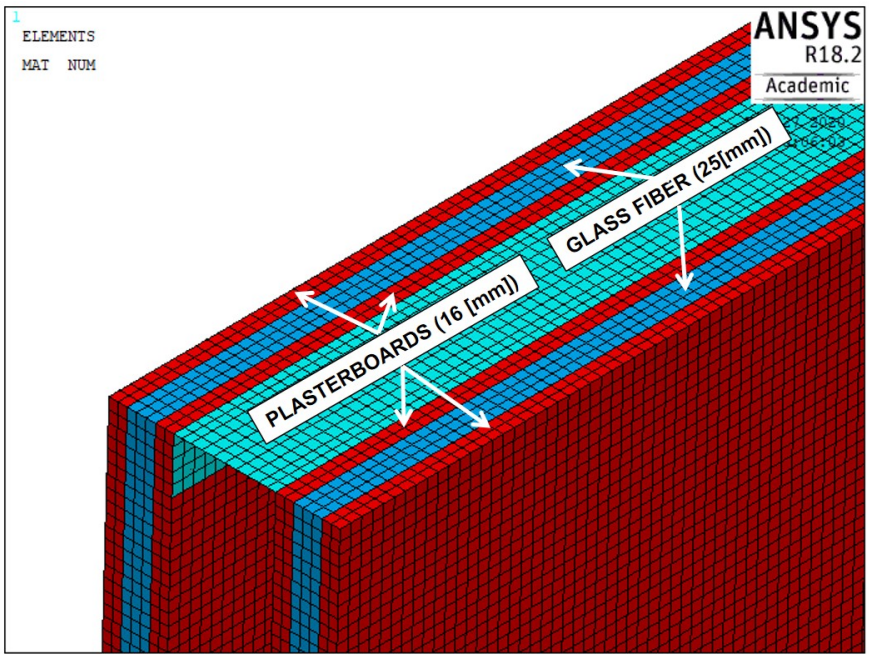

Figure 5.17: Wall geometry with applied mesh, plasterboards (red) and external insulation (dark blue).

The 10 [mm] mesh was chosen instead of 4 [mm] due time and memory limitations. For this reason, the mechanical simulations that are going to be developed after the thermal simulation, will be using the same mesh size, 10 [mm], distance between nodes.

5.3.4 Boundary conditions

Thermal simulation aims to model the fire inside the furnace in a transient-state. For this reason, the boundary conditions need to model a full-scale test model.

The first step and boundary condition, is to apply in all the nodes from the structure the initial temperature of 20 [°C]. Then, the others conditions should be applied at the unexposed surface (which stays outside the furnace), cavity (inside the structure) and exposed surface (which stay inside the furnace), see Figure 5.18 for more details.

Figure 5.18: Upper view of the structure in Ansys.

a) Unexposed surface

For unexposed surface, according to EN 1991-1.2 [22], the heat flux should be calculated by equation 3.4. Hence, at this surface the convection boundary with film coefficient of 9 [$W/m^2 \cdot K$] and constant bulk temperature of 20 [°C] have been applied (see Figure 5.19).

b) Cavity

The cavity is the region between plasterboards where the four studs are located. In this location, the heat flux is also described by equation 3.4, that is, convection and radiation shall be considered. This boundary condition is not specified by EN 1991 part 1.2, but has been used for long time by Piloto, Khetata and Gavilán [19].

For convection, at the outside surfaces from studs and at the inside surfaces of paste-boards which are in contact with the cavity region, a film coefficient of 17,5 [$W/m^2 \cdot K$] [19] for convection with bulk temperature determined from experimental tests were applied (see Figure 5.19). The profile was defined by the average temperature measured at mid-height of Stud 3 from [7] and is shown in Figure 5.20. This bulk temperature takes

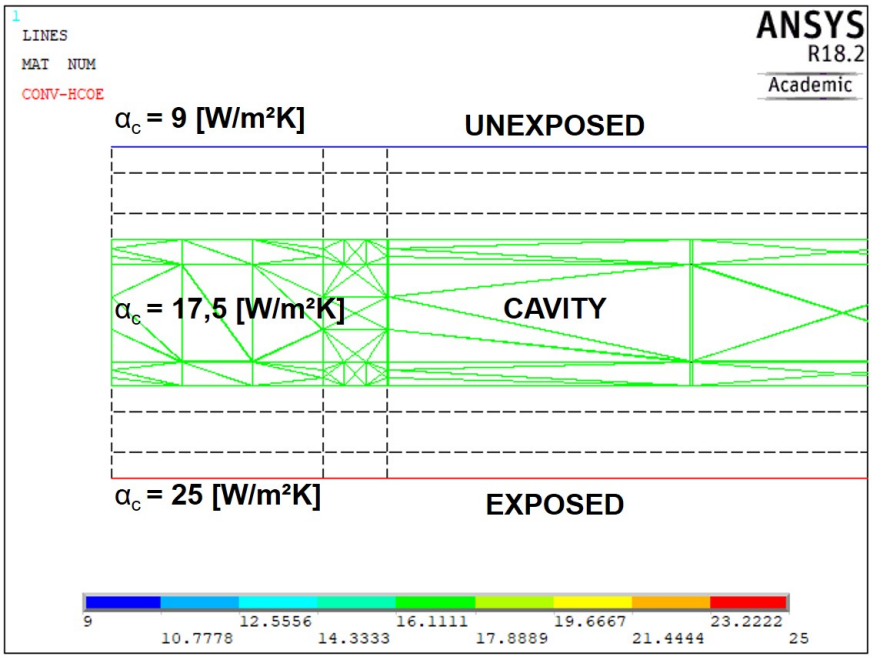

Figure 5.19: Upper view of the structure with convection applied.

into consideration the thermal damage of the protection layers.

The radiation boundary condition is also applied in at the steel elements in contact with air, using the emissivity value equals to 1 and defining a second enclosure (number 2) (see Figure 5.21). The enclosure 2 was created with Stephan Boltzmann constant equal to $5,67 \times 10^{-8}$ $[W/m^2 \cdot K^4]$, using a space node that contains the temperature profile from Figure 5.20. This condition was also applied to the gypsum finite elements that are in contact with the cavity region (see Figure 5.22). These elements will interact with the steel elements and their temperature variation will affect the heat flux by radiation.

c) Exposed surface

The heat flux by radiation and convection are going to be considered in the exposed surface. The convection film coefficient of 25 [W/$m^2 \cdot K$] (see Figure 5.19), is in accordance with EN 1991-1.2 [22], and the bulk temperature is determined by the ISO 834, eq. 3.1, due the fact that this surface is in contact with fire inside the furnace.

The radiation condition was applied at the same surface area, with emissivity equals to 1, defining the enclosure 1 (see Figure 5.21). The enclosure 1 was created with the

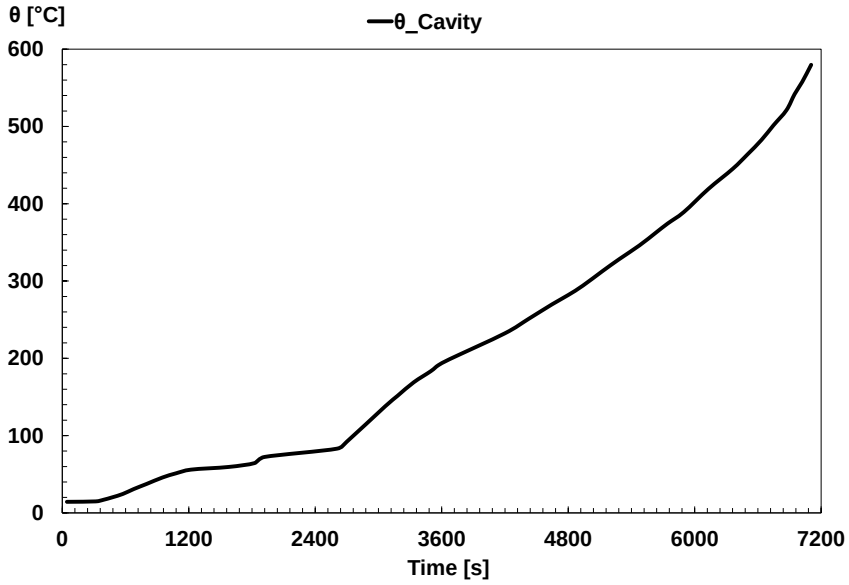

Figure 5.20: Bulk temperature profile used in FEA [7].

Stephan Boltzmann constant equal to $5,67 \times 10^{-8}$ $[W/m^2 \cdot K^4]$ using a space node that contained the temperature profile from ISO 834 (see Figure 3.2).

5.3.5 Solution Method

For thermal simulation, the full-method has been selected in Ansys, in which, the Newton-Raphson solution algorithm is used to solve for temperature, in the second order

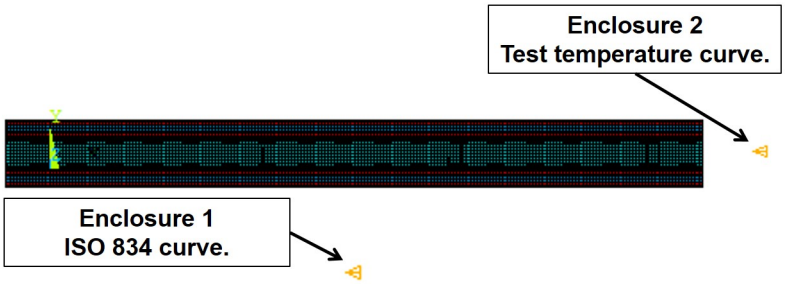

Figure 5.21: Enclosure position in finite element model.

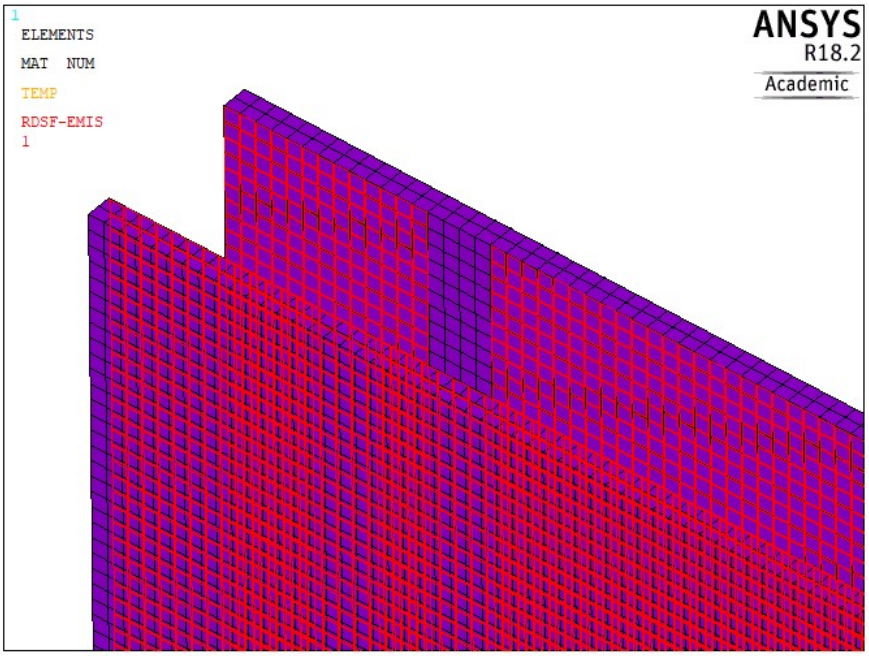

Figure 5.22: Radiation applied to the inside elements of the plasterboards.

differential equation. The governing equation is given by eq. 5.20. Where [C] is the specific heat matrix, [K] the conductivity matrix, θ the vector of nodal temperatures and Q^a the applied heat flows [27]. In this simulation, both time and temperature are incremented, so, at a time n+1, the temperature increment is given by 5.21. In which, Λ, is the transient integration parameter (1,0 by default), $\Delta t = t_{n+1} - t_n$ is the time variation between iteration n and n+1, θ_n is the nodal temperature at the time n, $\dot{\theta}_n$ is the time rate of the nodal temperatures values at time t_n (computed at previous time step) [27].

$$[C]\{\dot{\theta}\} + [K]\{\theta\} = Q^a \tag{5.20}$$

$$\{\theta_{(n+1)}\} = \{\theta_n\} + (1 - \Lambda)\Delta t\{\dot{\theta}_n\} + \theta\Delta t\{\dot{\theta}_{n+1}\} \tag{5.21}$$

At each increment, when θ_{n+1} is obtained, $\{\dot{\theta}_{n+1}\}$ is updated. After solving equation 5.20, the solver computes the L2 norm of the residual vector R(θ) and check the convergence in respect to heat flow, with a tolerance of 0,001 and a reference value of 1×10^{-6},

if the tolerance is met, then the solution converged, if not, time is dived by 2 and then the temperature is corrected, and $\{\dot{\theta}_{n+1}\}$ is updated with eq. 5.21 and the process is repeated until the solution is found.

The time at the end of the solution was set as 7200 [s] with an average time step of 60 [s] and maximum time step of 60 [s] and minimum set as 1 [s].

5.4 Thermomechanical Analysis under fire

During full scale-tests, while the temperature of the furnace is rising by equation 3.1, the hydraulic jacks are keeping a constant load applied in the LSF wall (see Figure 4.2). This procedure is in accordance to the experimental test loading system.

During test, as the temperature rises, the mechanical properties are being affected and the wall will start, at some point, to show signs of failure such as cracks and openings in the plasterboard and/or buckling, until it can no longer sustain the load, failing.

The thermomechanical analysis aims to verify, if the wall can still withstand mechanical load during the fire situation.

The thermomechanical analysis is a sequential of mechanical simulations, with a predefined time step, that takes in to account the temperature field. However, since it is a structural simulation, the plasterboards and insulation material were removed, resulting only the LSF structure. Additionally, load is applied on the studs, so the solver, at each time increment, will try to establish mechanical equilibrium in the structure using the properties determined for the temperature field for that time.

If the thermal expansion is considered, the mechanical load has to be decreased during the test, as it is the case in experimental tests, keeping the load constant.

5.4.1 Element Type

Since this is a structural simulation, the element and element configuration used are the same from room temperature simulation: shell 181, more information can be found in 5.2.2.

5.4.2 Thermomechanical Properties

In this simulation, for steel, the stress-strain relationship, including the yield strength and elastic modulus in function of temperature will be considered.

Regarding the insulation's materials, the plasterboards and glass fibre, they were removed from the structure in this simulation, therefore, their properties were not considered.

In addition, for this analysis, the thermal elongation was considered, being taken from EN 1993 1.2 [26], presented in Appendix B.

5.4.2.1 Stress-strain - constitutive law

The elastic part of the stress-strain curves is determined with the respective elastic modulus and yield strength for a given temperature. The reduction factors applied to these properties are presented by EN 1993-1.2 [26], however, for more accurate results, the properties provided by the material characterization are to be taken in consideration.

For the LSF wall, Gunalan and Mahendran used the strain-stress curves from equations proposed by Ranawaka and Mahendran, developed in 2009 that, for a given stress, f_θ, at a temperature θ, the strain is found by eq. 5.22 [2], [31]. This constitutive model is the well-known Ramberg Osgood model.

$$\varepsilon_\theta = \frac{f_\theta}{E_\theta} + \beta \cdot \left(\frac{f_{y,\theta}}{E_\theta}\right) \cdot \left(\frac{f_\theta}{f_{y,\theta}}\right)^{n_\theta} \tag{5.22}$$

In which, E_θ is the elastic modulus, $f_{y,\theta}$ is the yield strength, β is a parameter that should be taken as 0,86 and n_θ is given by the eq. 5.23.

$$n_\theta = -3,05 \times 10^{-7} \cdot \theta^3 + 0,0005 \cdot \theta^2 - 0,2615 \cdot \theta + 62,653 \tag{5.23}$$

Where, θ is the temperature, that can change between 20 and 800 [°C]. The yield strength is found by equations 5.24, 5.25 and 5.26 [2].

$$20 \leq \theta < 300\ [^{\circ}C] \qquad \frac{f_{y,\theta}}{f_{y,20}} = \left(1 - \frac{(\theta - 20)^{4,56}}{1 \times 10^{10} \cdot \theta}\right) \tag{5.24}$$

$$300 \leq \theta < 600\ [^{\circ}C] \qquad \frac{f_{y,\theta}}{f_{y,20}} = \left(0,95 - \frac{(\theta - 300)^{1,45}}{7,76 \cdot \theta}\right) \tag{5.25}$$

$$600 \leq \theta \leq 800\ [^{\circ}C] \qquad \frac{f_{y,\theta}}{f_{y,20}} = -0,0004 \cdot \theta + 0,35 \tag{5.26}$$

The ratio $f_{y,\theta}/f_{y,20}$ is the reduction factor, in which, $f_{y,20}$ is the 0,2% stress at room temperature and $f_{y,\theta}$ is the 0,2% stress at θ temperature. For the elastic modulus, E_θ, equations 5.27 and 5.28 shall be used [2].

$$20 \leq \theta \leq 200\ [^{\circ}C] \qquad \frac{E_\theta}{E_{20}} = -0,000835 \cdot \theta + 1,0167 \tag{5.27}$$

$$200 < \theta \leq 300\ [^{\circ}C] \qquad \frac{E_\theta}{E_{20}} = -0,00135 \cdot \theta + 1,1201 \tag{5.28}$$

The ratio E_θ/E_{20} is the elastic modulus reduction factor, where, E_{20} is the elastic modulus at room temperature and E_θ at the temperature θ. Stress-strain curves were obtained using equation 5.22 to 5.28, with $E_\theta = 213{,}512$ [MPa] and $f_{y,20} = 569$ [MPa] [2], they are shown in Figure 5.23.

For comparison purposes, the reduction factor provided by EN 1993-1.2 [26] for cold formed class 4 steel sections, namely, $k_{p0,2,\theta}$, and $k_{E,\theta}$ were plotted in with the reduction factor used by Gunalan and Mahendran (2013) [13] from equation 5.24 to 5.28.

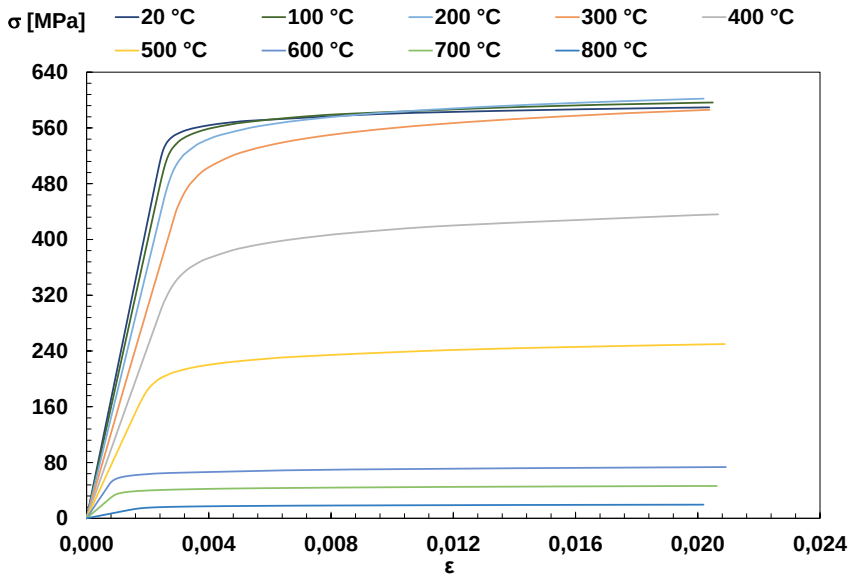

Figure 5.23: Stress-strain curves for G500 steel.

The graph shows a significant difference between the two biography (see Figure 5.24) for both: yield strength ($k_{p0,2,\theta}$ and $f_{y,\theta}/f_{y,20}$) and elastic modulus ($k_{E,\theta}$ and E_θ/E_{20}), reasons why, the reduction factors provided by the European standard will be not considered in this study.

5.4.3 Finite Element Mesh

The element mesh was maintained from the thermal simulation, with 10 [mm] elements, due to the fact that the numbers of nodes from both simulations have to be the same, so that the nodal temperatures from thermal simulation can be used as input in this analysis. More information about the mesh can be found in 5.3.3.

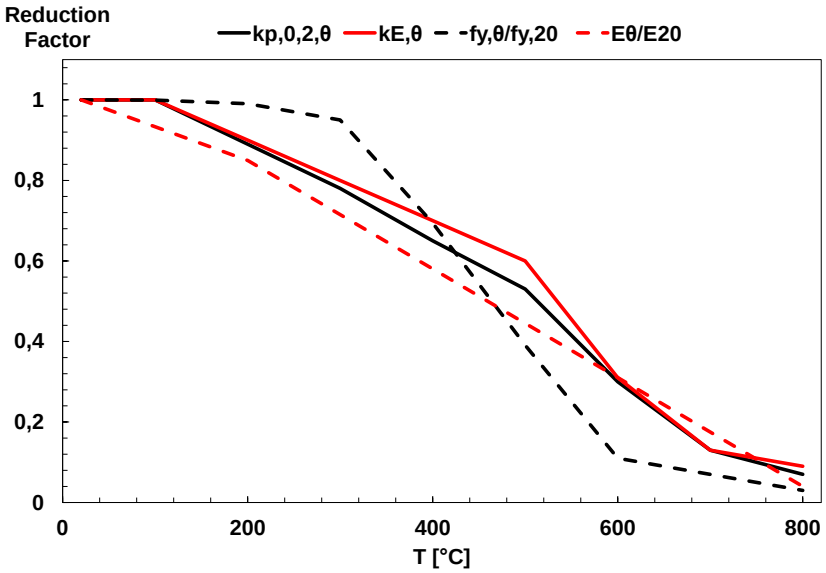

Figure 5.24: Reduction factor based on Gunalan and Mahendran (2013) and EN 1993-1.2 [26].

5.4.4 Boundary Conditions

The boundary conditions were used the same as the under room temperature analysis with two changes: the load and temperature variation.

The mechanical load applied should be defined by the Load Ratio, which depends on the ultimate load at room temperature, given by eq. 5.29.

$$LR = \frac{T}{U} \tag{5.29}$$

The load ratio, is defined as a percentage of the Ultimate Load U and T is the target load to be applied in thermomechanical simulation, both in [N]. The selection of the load ratio is very important, because higher load ratio approximate the applied load to the load bearing capacity, that is, to the failure load. This means that, in higher temperature, where the mechanical resistance is lower in comparison to room resistance, the wall will only withstand for a short period of time, thus, being not able to observe

the wall behaviour during the fire situation. Therefore, the fire resistance depends on the load ratio, and this value is selected based in the application of the element, also defined by the engineer during test. For validation of the model, a load ratio of approximately 20 [%] was applied [12], in which represents a magnitude of 15 [kN].

Although the load is a constant value, during tests, the thermal expansion causes displacements, therefore, reaction forces, in which the hydraulic jacks have to add or reduce load to keep the magnitude of the resulting force in 15 [kN]. For this reason, this model has accounted for the load change during time, and for that, a resulting force between the target (15 [kN]) and the reaction caused by thermal elongation for each time increment has to be obtained. The thermal expansion expression is given by equation eq. 5.30.

$$\varepsilon = \alpha \cdot \Delta\theta \tag{5.30}$$

In which, ε is the thermal elongation, α is the thermal expansion coefficient, in $[K^{-1}]$ and $\Delta\theta$ the temperature variation. The strain ε can be calculated using the simplified Hooks law, assuming the elastic relation between the Young's modulus (E) and the tensile stress (σ), see eq. 5.31.

$$\sigma = \varepsilon \cdot E \qquad \text{[MPa]} \tag{5.31}$$

Assuming a uniform distributed load in each stud cross section, assuming, σ= P/A and applying in 5.31 combining with equation 5.30, the reaction force caused by the thermal elongation is given by eq. 5.32.

$$P = A \cdot E(\theta) \cdot \alpha(\theta) \cdot \Delta\theta \qquad \text{[N]} \tag{5.32}$$

In which, the Young's modulus and α, are temperature dependent. The cross-sectional area, A, is from the studs, with a value of $1,92855 \times 10^{-4}$ $[m^2]$. Therefore, the resulting force (R) is found by eq. 5.33.

$$R = T - P \qquad \text{[kN]} \quad (5.33)$$

Where, P is the reaction force from eq. 5.32 and T is the target load, that, for LR of 20% is 15 [kN]. So, R was the applied load during thermomechanical simulation. For the parametric analysis, a load ration LR of 40 % has also been used.

The nodal temperatures from transient simulation were applied to the structure.

5.4.5 Solution Method

The structural simulations are non-linear, and the solver will use the Newton-Raphson method to find the solution. This method was explained before and can be seen in 5.2.8.1.

The time at the end was settled 7200 [s] with average and maximum incremental step of 60 [s] and minimum set as 1 [s]. After, analyzing the time in which the LSF Wall structurally failed, the maximum temperature (critical temperature) for that given time is also obtained. The fire resistance is given by the last time that the wall was able to withstand the combined mechanical and thermal load. However, at each time increment, the stiffness matrix from equation 5.13, is changing due to the mechanical properties variation with temperature. Thus, the solver will update the matrix in accordance to the properties for that given temperature, previously determined and will try to establish equilibrium until it reaches the maximum displacement in a given time. Also, the applied load is varying in function of the time, so, at each time increment the solver will keep the load level (introducing the variation due to thermal expansion).

After, analysing the time in which the LSF Wall structurally failed, the maximum temperature (critical temperature) for that given time is also determined (on average). The fire resistance is given by the last time that the wall was able to withstand the combined mechanical and thermal load.

5.5 Validation of the Finite Element Model

Finite element model validation will be presented, comparing with the tests results in three steps: (1) the ultimate load and displacement at room temperature, (2) temperature field, (3) thermomechanical behaviour using time versus displacement comparison.

5.5.1 Validation at room temperature

In order to obtain the material imperfection, the lowest buckling load was considered. Since only web imperfections were considered, the x nodal displacement was analysed and the $u_{x,max}$ was obtained to apply the scale factor from eq. 5.8. The lowest eigen buckling load was localized in the third stud (see Figure 5.25) and the deformed shape for this eigen value showed web buckling.

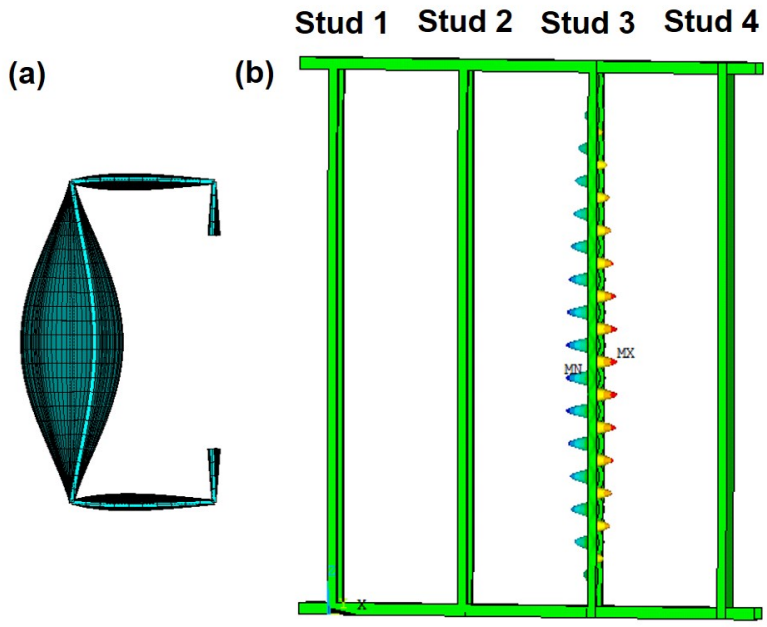

Figure 5.25: (a) upper view of the buckling shape of stud 3, (b) u_x and the buckled mode for the lowest buckling load.

In the non-linear simulation, the model was able to predict the ultimate load in comparison with full-scale test results from [13]. The results showed failure by local buckling of web and flanges, accentuated in the base of the stud, close to the loading point. In the

tests, larger web deformations and failure due to local web buckling and flanges were seen near the supports [2]. The comparison is shown in Figure 5.26.

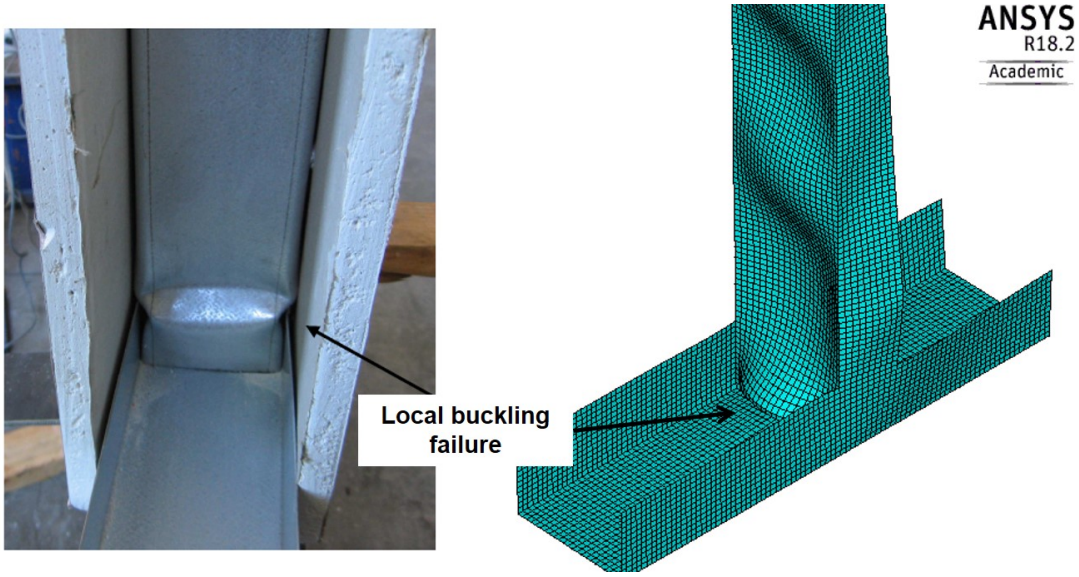

Figure 5.26: Stud3 at failure time in test [2], in the left, and in the right, Stud 3 at failure time from FEA.

The nodes displacements, where the loads were applied, were extracted from FEA model and are depicted in Figure 5.27. For the simulated LSF Wall, the Stud 3 demonstrated higher axial deformation when compared to the other studs. Even though the difference is not significant. This behaviour agrees with test results, because during tests, Stud 3 and 2 showed the highest deformation (see Figure 5.27).

The results from the FEA model developed by Gunalan and Mahendran were also added to the graph [2]. When compared with the Gunalan's FEA model the results agreed well, however, the studs during the full-scaled test had higher displacement.

The observed higher displacement in test when compared to FEA, shown in Figure 5.28, could have been, in accordance with Gunalan, due an overall initial imperfection in the stud [2] that was not accounted. Still, the author stated that others deviations in testing, might have led to higher deformation, that, led to higher axial shortening.

The comparison between Newton-Raphson model with force and displacement increment is shown in Figure 5.29. Results are the same with some slight difference in Stud 3.

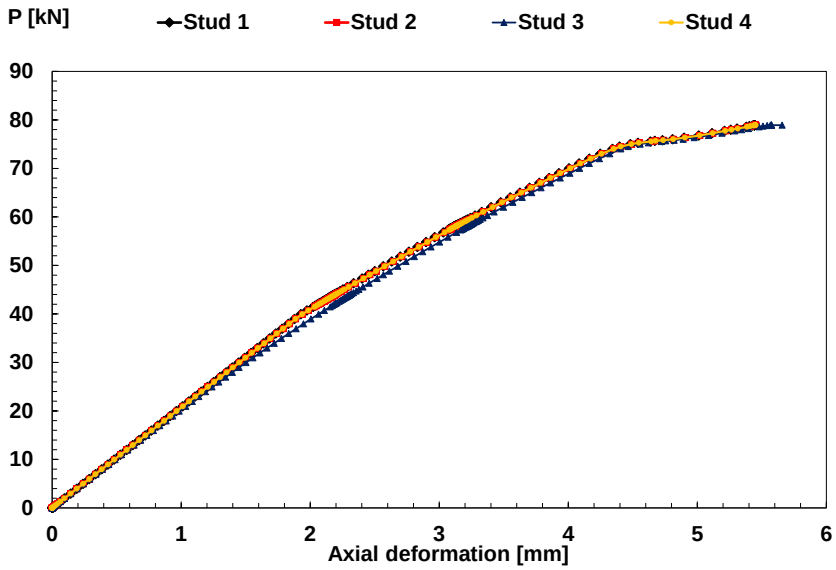

Figure 5.27: Axial deformation in function of the applied load.

However, both models reached the same ultimate load. Still, none of the models were able to follow the equilibrium path, that is expected of NR with load increment, however, since NR with displacement increment was also not able to predict, means that the structure goes under a snap-back behavior, shown in 5.13, in which, this model is not capable of predict.

The results obtained are compared with test results in Table 5.4, ultimate load (U) relative errors were compared with test results and critical load (P_{cr}) error was compared with Gunalan [2] finite element analysis.

Table 5.4: Results compared for room temperature.

Model	P_{cr} [kN]	U [kN]	Relative error P_{cr}/U [%]
Test*	–	79	–/–
FEA (Gunlan)*	39,8	77,1	–/2,4
FEA	39,8	78,89	0/0,13

*Taken from [2].

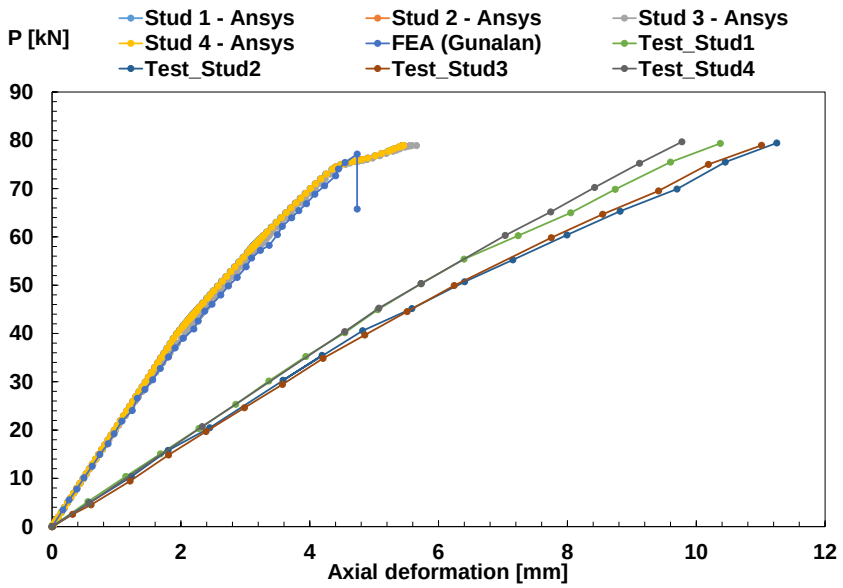

Figure 5.28: Axial deformation comparison.

In respect to the von Mises stress of the LSF Wall at failure, the highest stress was found near the base where the load was applied, also high stress values were obtained along studs. The yielding has occurred in the web element near the base, where values were higher than the 569 [MPa] G500 yield strength. The results from von Mises stress is shown in Figure 5.30.

All results at room temperature showed good agreement with test results, thus, this model can be considered validated for room temperature analysis.

5.5.2 Temperature field validation

The temperature field depends on time. The numerical results were obtained in the same location used for the thermocouples during the test (see Figure 5.31). At each surface three nodes temperature curves were extracted at the mid-height (1,2 [m]) of the LSF Wall.

The three temperature curves were then averaged, to define the, Pb1-Ins (temperature

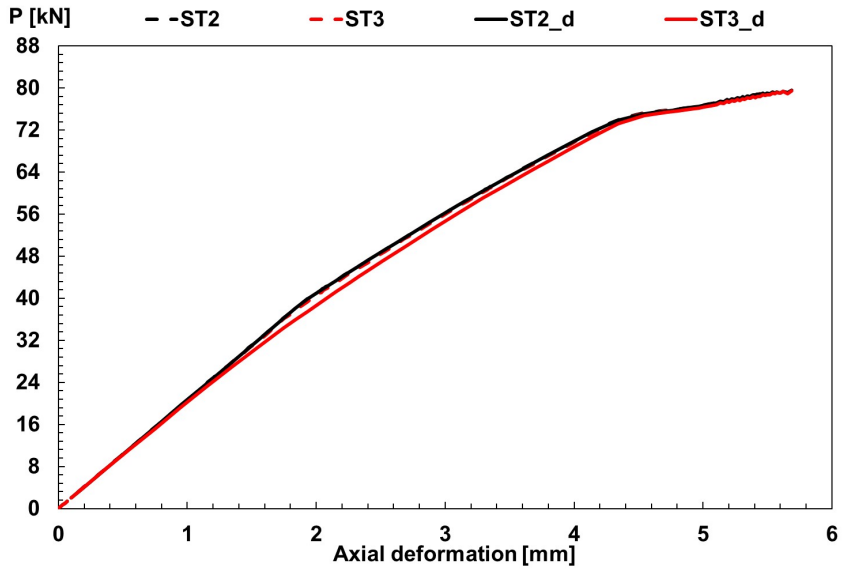

Figure 5.29: Comparison between force and displacement increment (d).

of the interface surface between the exposed plasterboard 1 (Pb1) and insulation (Ins.)), Pb2-Cav (temperature on the cavity facing surface of the exposed plasterboard 2 (Pb2)), Pb3-Cav (temperature on the cavity facing the surface from plasterboard 3 (Pb3)), Pb3-Ins (temperature of the interface surface between base layer plasterboard 3 (Pb3) and insulation (Ins.)), Ins-Pb4 (temperature of the interface between the insulation and plasterboard 4 (Pb4)), AS (ambient side, temperature of the bottom (unexposed) surface of plasterboard 4 (Pb4)) and FS (fire side, temperature of the top layer of plasterboard 1 (Pb1)). The results for the model are shown in Figure 5.32.

Fire side temperature curve follow the trend of the ISO 834 from equation 3.1, while Pb1-Ins was affected by the gypsum properties and material degradation.

In essence, the temperature variation depends on the relation of specific heat (c), thermal conductivity (k) and density (ρ), named thermal diffusivity (α), in which is equal to $\alpha = k/\rho c$, it represents the quantity of heat that is transferred in a material from the hot to the cold side.

At the begging, for Pb1-Ins, the plasterboard has low thermal diffusivity due the decrease in the thermal conductivity and a growth in the specific heat, therefore, the temperature gradient is small. When the Pb1-Ins temperature reaches 100 [°C], about

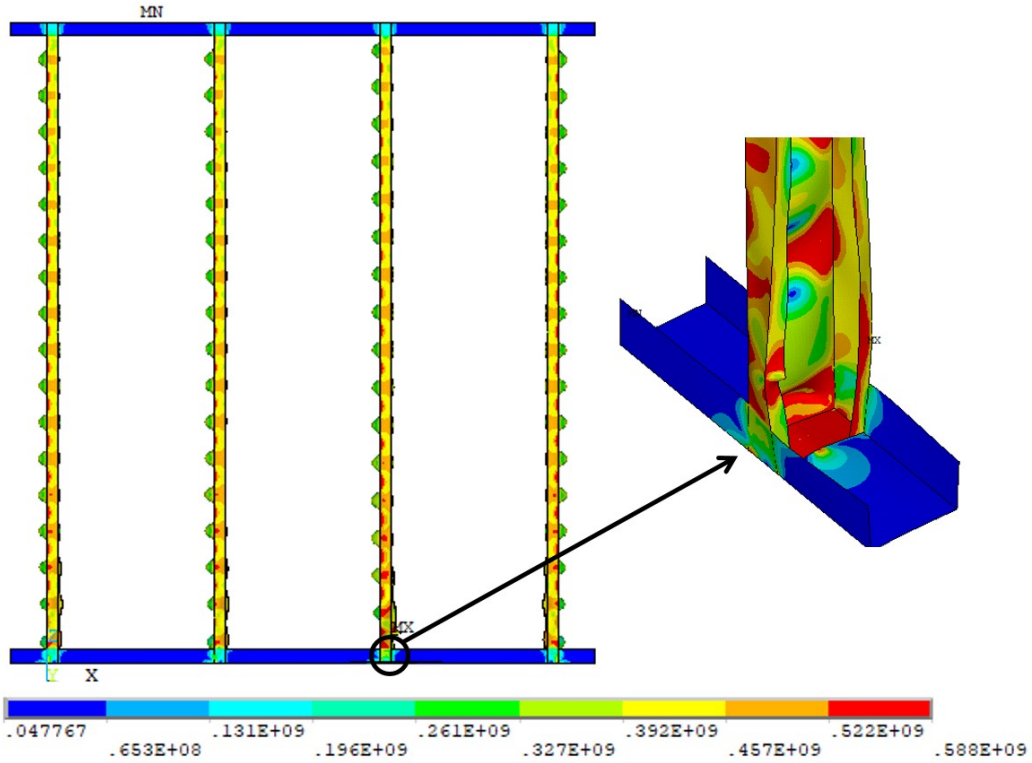

Figure 5.30: Von Mises stress for the LSF Wall for the Ultimate Limit State.

16 min, the temperature gradient rises, because the specific heat is starting to decrease and at the same time thermal conductivity is going up. Density remains constants after reaching 85 [°C] so it will no longer influence in heat transfer.

By the time Pb1-Ins reaches 400 [°C], the thermal conductivity of gypsum begins to grow sharply whereas specific heat is still decreasing, thus, the thermal diffusivity is bigger, resulting in a higher temperature gradient. This behaviour is seen until 41 min. When temperature reaches 600 [°C], at this point the specific heat undergo a growth phase

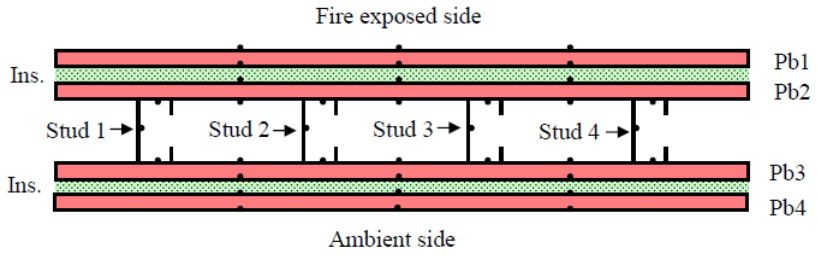

Figure 5.31: Position of thermocouples during test [7].

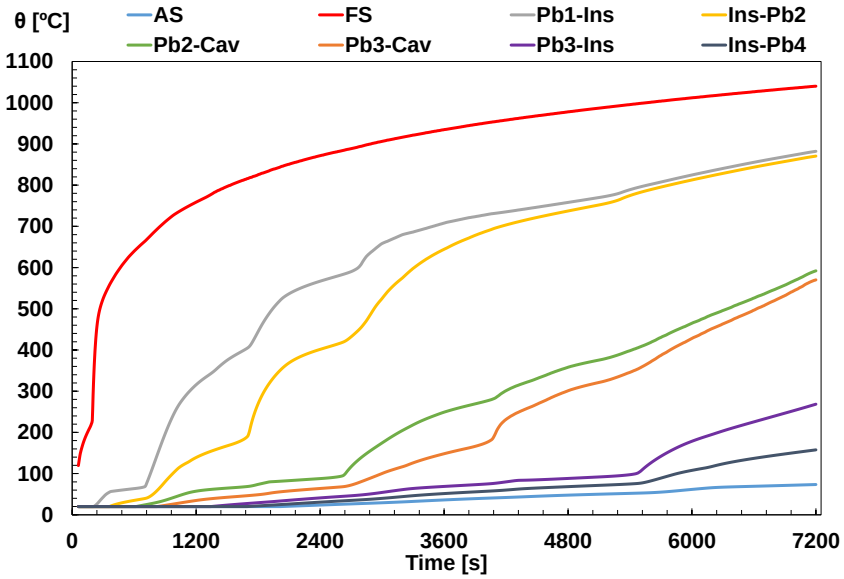

Figure 5.32: Temperature vs. time extracted from FEA model.

until about 700 [°C], when it decreases again, slowing down the temperature gain rate during this period. After 800 [°C], the specific heat is constant and thermal conductivity is varying linearly through time, in which, causes an almost linear temperature variation seen after 70 min.

Ins-Pb2 temperature depends on the glass fibre (GF) thermal properties and for this case, the specific heat and density are constants for all the temperature range, whereas the thermal conductivity is constant until 600 [°C], linear between 600-700 [°C] and after, remains linear but with an accentuated gain rate. For this reason, the variation until 600 [°C] depends only in the amount of heat that is crossing the plasterboard, therefore, the temperature gradient behaviour was similar to Pb1-Ins during that period. After 50 min, when temperature reaches 600 [°C] for Ins-Pb2, the temperature gradient rises quicker and by the time it gets to 700 [°C] the thermal conductivity is high enough to lead the Ins-Pb2 near to the temperature of Pb1-Ins. The almost linear behaviour seen after about 69 minutes is due to the linear variation of the thermal conductivity of glass fibre.

The Pb2-Cav temperature profile is located in the second plasterboard (Pb2), depending on the gypsum thermal properties. At this location, less heat is reaching the Pb2 surface, because much of the heat was absolved by the first plasterboard and by the glass fibre insulation, thus, temperatures variations are smaller than the two before. So, until about 47 min, due to small thermal diffusivity, the temperature variation was not accentuated. After 47 min, the temperature is at 120 [°C], and the specific heat is decreasing whereas the plasterboard conductivity is increasing. From this time on, the temperature is rising until the end of the simulation. No other variation is observed due to the fact that density is constant after 85 [°C] and specific heat only increases after 600 [°C], however the maximum temperature, at the end of the simulation, for Pb2-Cav was 592 [°C].

Pb3-Cav temperatures are also depending on gypsum thermal properties, and are located between in the third plasterboard (Pb3). The heat reaching this surface has been decreased due previous Pb1, Pb2, GF and also steel structure absorption, thus, lower temperature gradient is expected. When Pb2-Cav temperature reaches 100 [°C], more heat is getting though the Pb2, therefore, there is increase in Pb3-Cav temperature, in which, reaches the temperature where it starts to have higher thermal diffusivity. From this point on, the temperature gradient will increase according to the thermal conductivity and the heat transferred by Pb2 and the steel structure. This is the same case as before, no other variance is seen because the maximum temperature reached was about 570 [°C], less than the one needed to decrease the thermal diffusivity.

Pb3-Ins is located in the glass fibre insulation between Pb3 and Pb4. The maximum temperature reached for Pb3-Ins was 293 [°C] and since all thermal properties are constant until 600 [°C] for GF, the variation was caused by the amount of heating coming from Pb3. After 47 min, a noticeable temperature gradient is seen due to the fact that more heat is passing through Pb3, so, when Pb3-Cav starts to grown rapidly at about 91 min, Pb3-Ins also grows quicker.

Ins-Pb4, located in the fourth plasterboard (Pb4), follows the Pb3-Ins behavior, since it depends in the heat transferred by the insulation. When Pb3-Ins is growing faster, at

about 91 min, Ins-Pb4 is reaching 100 [°C], where thermal diffusivity for gypsum is higher, therefore, a bigger temperature gradient is seen, leading to a maximum temperature of 157 [°C] for Ins-Pb4.

The ambient temperature (AS) is located in the outer surface of Pb4. At this point, almost all the heat generated by the fire (furnace), was absolved by the insulations, steels and plasterboards. Thus, the temperature variation is slower when compared to the others. A small increase can be seen after 100 min, when the inner surface of the Pb4 (Ins-Pb4) reaches 100 [°C] and more heat is passing through to this surface. The maximum temperature obtained was, approximately, 73 [°C].

Temperatures obtained by the thermocouple during test were also calculated into an average curve by Gunalan and Mahendran [7]. The comparison between temperatures profiles obtained with FEA model and those from tests are plotted in Figure 5.33.

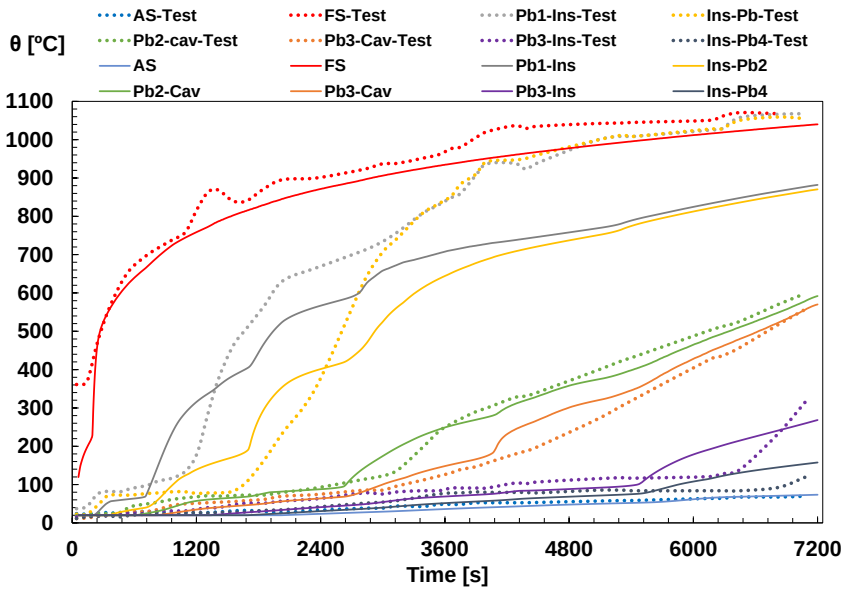

Figure 5.33: Average temperature profiles from test [7] and FEA.

All temperatures curves agreed well with test results, except for Pb1-Ins and Ins-Pb2. The sudden rise in temperature for Pb1-Ins, after 25 min that consisted until 35 min,

according to Gunalan [2], was caused by the heat blocked and redirected by the adjoining layer of insulation, in which Ansys was not capable of predicting with accuracy, even thou it was able to predict the risen behavior. After that, the Pb1-Ins temperature gradient started to reduce due the melt of insulation, where the heat was being used in the chemical process and thus the temperature did not change drastically [2]. From this point until the end the curve approaches the fire side temperature gradually due to cracking and the of fallen plasterboard pieces. The left, middle pieces of plasterboards have fallen off at 86, 106 and the right piece has fallen between 86 and 106 min [2]. However, since in Ansys the plasterboards were considered as one piece and that the mass loss was not accounted, it did not reproduce the plasterboard fallen off, thus, the average temperature in the end did not reach fire side values.

As for temperature Ins-Pb2, at 30 min the insulation started to burn and by the time 44 min, it was completely burned at mid-height between Stud 3 and 4 [2]. At 47 min, the Pb1-Ins and Ins-Pb2 temperature curves intersects, indicating burning out of the insulation at mid-height of the wall specimen between Studs e and 3 [2]. After that, due the fallen off the plasterboards pieces, the region is exposed to the furnace fire and thus it approaches the fire side temperature curve [2].

The FEA model developed in this work did not account for mass transportation, that is, no moisture diffusion has been considered and did not account for explicit thermal degradation (thermal degradation has been consider when using the bulk temperature of the cavity). Therefore, heat is still being consumed by the plasterboard, in which will not fall off, thus, and did not expose the cavity to the furnace condition, therefore, the amount of heat at the insulation was less than during tests. Still, the glass fibre insulation will not burn out, resulting in a minor temperature gradient than the one showed in test. For this reason, Pb1-Ins and Ins-Pb2 curves will not intercept, rather, they will continuously increase linearly and for those, higher maximum temperature relative error is expected.

For the others curves, the FEA model was able to predict the behaviour with very good agreement due to the fact that the Pb1 fall off and insulation burn out did not have much influence in these parts, that is, Pb3, Pb4 and GF insulation were not exposed

to the furnace heat directly. The comparison between the FEA and test were made for two variables: the maximum temperature and the root mean square error (RMSE). The RMSE is given by equation 5.34.

$$RMSE = \sqrt{\frac{1}{n}\sum_{i=1}^{n}\left[\frac{\theta_{FEA} - \theta_{test}}{\theta_{test}}\right]^2} \tag{5.34}$$

In which, n is the number of time instants to make the comparison, θ_{FEA} is the temperature from the finite element model and θ_{test} is the temperature from test. This error represents the relative difference between the two curves (FEA and test) so, in a perfect representation RMSE would be equal to 0, which means that as closer as 0 is, the better the finite element results are. Pb1-Ins and Ins-Pb2 will not be checked with RMSE due to the reasons cited before, they were not able to predict the fire behaviour. In addition, temperature from test below 20 [°C] were not considered, since the initial temperature for the FEA model was set to 20 [°C].

The RSME and maximum temperature for each curve is presented in the Table 5.5.

Table 5.5: Comparison of the average and maximum temperatures.

Temperature Point	Maximum Temperature [°C]		Error	
	Test*	FEA	RMSE	MAX. T. [%]
FS	1070	1040	—-	2,8
Pb1-Ins	1067	882	—-	17,3
Ins-Pb2	1059	871	—-	17,7
Pb2-Cav	598	592	0,20	1,0
Pb3-Cav	557	570	0,21	2,2
Pb3-Ins	315	269	0,32	14,6
Ins-Pb4	119	157	0,29	24,2
AS	70	73	0,23	4,1

*Taken from [2]

As for the studs temperature curves, only Stud 2 (ST2) and 3 (ST3) were considered, for two reasons: first, the temperature profile for all studs resulted as exactly the same for FEA and second, only temperature profile of the centre studs (2 and 3) were presented by Gunalan, Korlarkar and Mahendran [7]. Temperatures were extracted at the cold flange

(CF), hot flange (HF) and web (WB) at the mid-height of each stud (see Figure 5.34). Temperature profiles for stud 2 and 3 are in Figure 5.35.

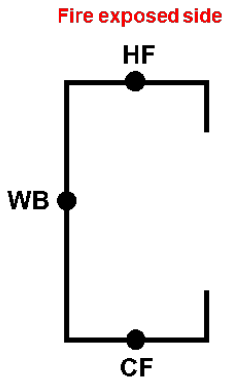

Figure 5.34: Points to obtain the temperatures.

Web, cold and hot flange for all studs showed the same values and behaviour. The comparisons with test results were made using an average value of the three points (HF, CF, WB) and its shown in Figure 5.36. The temperature distribution for stud 3 at mid-height is shown in Figure 5.37.

Results from test showed similar behaviour for stud 2 and stud 3 (see Figure 5.36). The main difference, is seen from 47 [min] until 66 [min] for stud 2. Stud 3 agree well in this period, because during test, higher temperatures were caused by the burn of the insulation material, due to the fact that the vertical joint of Pb2 was placed along stud 3. FEA model did not predict the material burnt out, but, the temperatures were similar. The curves showed good agreement with test results. Table 5.6 shows the relative error for each curve.

Table 5.6: Relative errors for center studs temperatures.

Stud	Maximum Temperature [°C]		Error	
	Test*	FEA	RMSE	MAX. T. [%]
Stud 2	582	583	0,14	0,2
Stud 3	664	583	0,11	12,2

*Taken from [2]

The relative errors found (see Table 5.5 and Table 5.6) were associated to the fact,

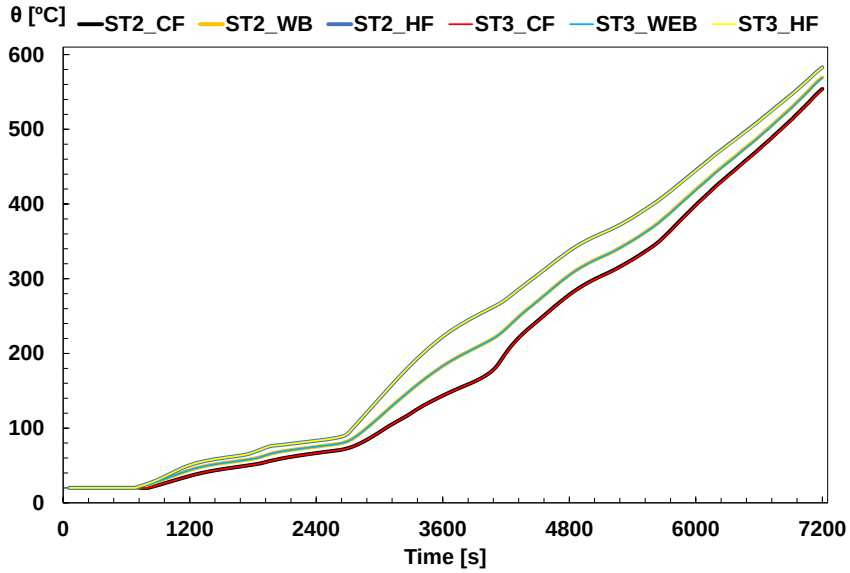

Figure 5.35: Temperature profiles for stud 2 (ST2) and stud 3 (ST3).

as pointed before, that the model did not account for mass loss, thus, not being able to reproduce the plasterboard fall off and the glass fibre burn out. Still, another factors have influenced the results: the mesh size and the experimental furnace curve. In this study no mesh convergence analyses were made to ensure that the results obtained were not influenced by the mathematical model, that is, temperatures values could have been higher or lower when compared with the results showed here. As in the previous static analyses the results converged for 4 [mm] elements, most likely that thermal model would also converge at the same size, however, due to the large time and memory consuming of these simulations, no mesh convergence test were carried out.

The proposed convection coefficient, α_c of 17,5 [W/m^2·K], resulted to be a very good approximation for the film coefficient expected in the cavity. This value was suggested due to the fact that, in certain conditions, without cavity insulation, the protection layers are expected to fall off, exposing this region to the furnace conditions (convection and radiation). Because the falling off depends on the number of screws, on the type and

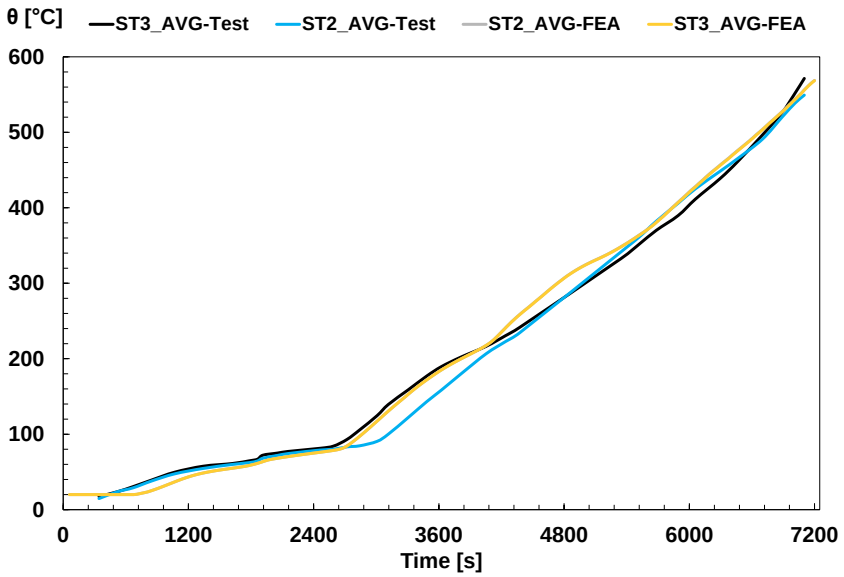

Figure 5.36: Comparison from FEA and test results [7]

number of layers that are protecting the LSF, only after a certain period of time, the cavity will be exposed to fire. By this reason, an average convection coefficient has been defined, using a bulk temperature defined by the average temperature of the cavity temperature between exposed and unexposed side.

In accordance with EN 1363-1 [25], the results for the unexposed side (room temperature) were analysed in order to verify if the wall has failed by the insulation criteria (see equations 4.3 and 4.4). The average and maximum temperature curve were plotted, using the temperatures collected from 30 nodes at the Pb4 outside surface (AS). Results showed that this LSF wall did not fail by insulation criteria, since it had lower temperature than both limits proposed by the standard, the results are shown in Figure 5.38.

Results agreed with test, in which, also did not fail by the insulation criteria, as Figure 5.38 shows.

For the considered boundary conditions, this thermal finite element model was considered suitable to predict the thermal behaviour of the LSF Wall.

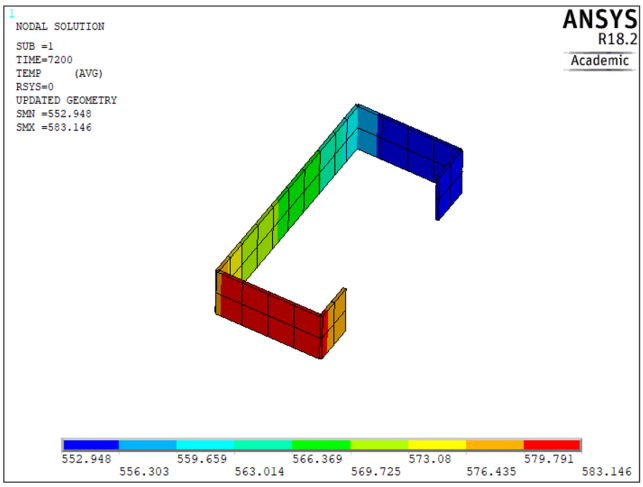

Figure 5.37: Temperature distribution for stud 3 at mid-height.

5.5.3 Thermomechanical validation

The resulting load, for LR of 20%, applied in the wall is presented in Figure 5.39. The thermal elongation reaction loads start to increase right after the studs' temperature start passing 20 [°C], and hit its peak at about 45 min, due to the increase in the thermal expansion coefficient.

Displacement from applied force nodes were extracted and are presented in Figure 5.40. The model showed high displacement level, increasing after about 45 [min], at the same moment that the thermal expansion hit its peak. Stud 4 showed the higher displacement, while stud 3 showed the lowest. The negative displacement is caused by the compression when the force is still at 15 [kN], after the studs' temperatures starts to grow, the structure expands due thermal expansion effects.

The comparison with tests and FEM results from [7], [13], are plotted in Figure 5.41. Results showed a big difference between tests and FEM results. Two reasons can be referred to this: one, the material properties and two, the mesh size. In respect to the material properties, even though they were collected from the biography, these values, when converted to true stress might have been slight changed or the approximations were not so accurate. In respect to the mesh, as pointed before, the model converged at 4 [mm] elements, however, due the limitations, this simulation was made with 10 [mm] that could

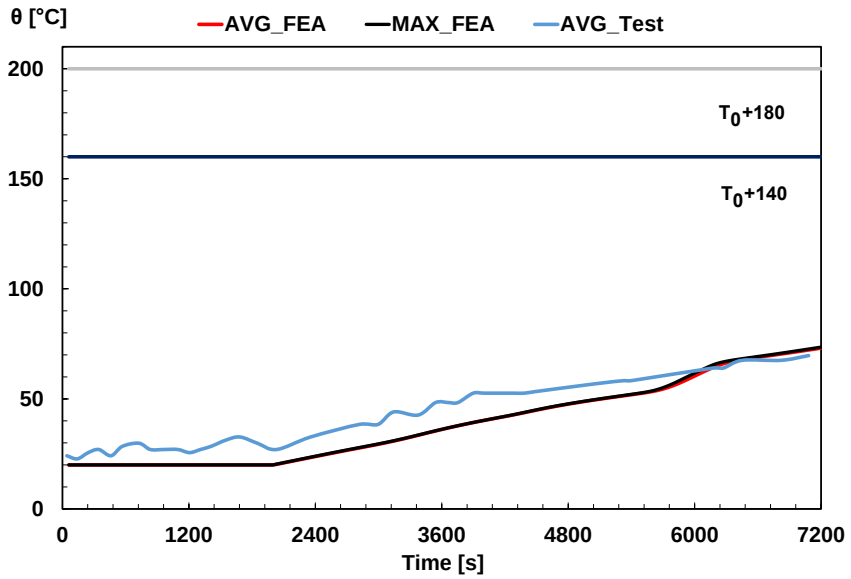

Figure 5.38: Insulation criteria. Test results taken from [7].

have led to this high deviation. Still, until about 45 [min], the prediction was accurate for the behaviour and displacement, also, after that point the model was able to predict the increase in displacements that the structure underwent during the test.

The failure mode obtained in FEA and test are in good agreement. During test the wall failed by moving away from the furnace (out of plane displacement) [7], as Figure 5.42 shows. This same behaviour is seen in the FEA model, at the time of failure, the thermal bowing that the stud 3 suffered, moved the stud in the opposite direction of the fire side (-y), the out of plane deflection also indicates the moving away from the furnace (+y) (see Figure 5.43). The critical temperature was 583 [°C] and the stud failed at 120 min (numerical failure).

The deformed shape modes for stud 2 and stud 3 are shown in Figure 5.44. In test, stud 2 and 3 showed inelastic local buckling of web and distortional buckling of the flanges [7]. The FEA deformed shape modes also show inelastic local buckling of web and the same instability mode for the flanges.

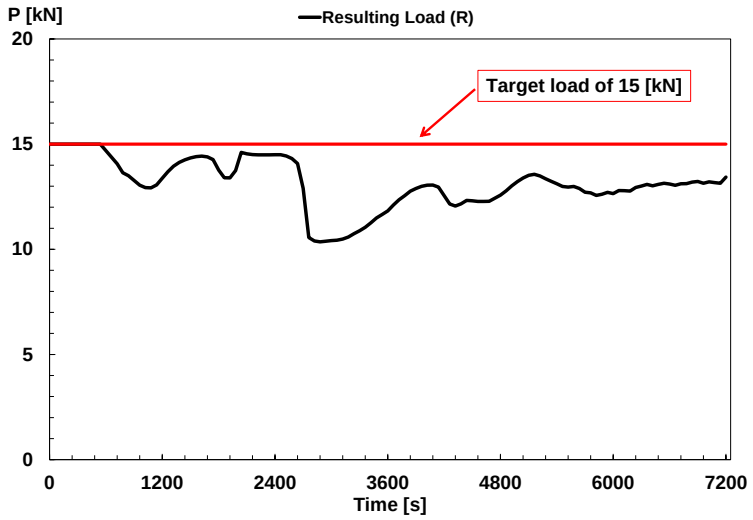

Figure 5.39: Resulting load.

The failures criteria for the load bearing capacity (R) given by EN 1363-1 [25], were evaluated to this model. The results are given in Figure 5.45. The wall did not fail by the maximum vertical contraction (h/100) or by the rate of vertical contraction (3h/1000).

This model was not able to represent with acceptable accuracy the test results, therefore, cannot be validated. However, it was still able to reproduce the LSF wall behaviour during fire. For this reason, this model will be used to develop parametric studies in order to analyse the influence of design models.

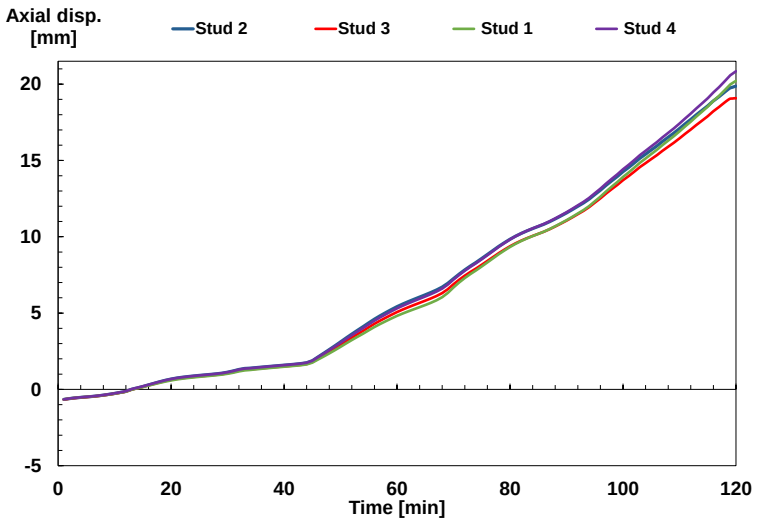

Figure 5.40: Axial displacement for the studs in thermomechanical analysis.

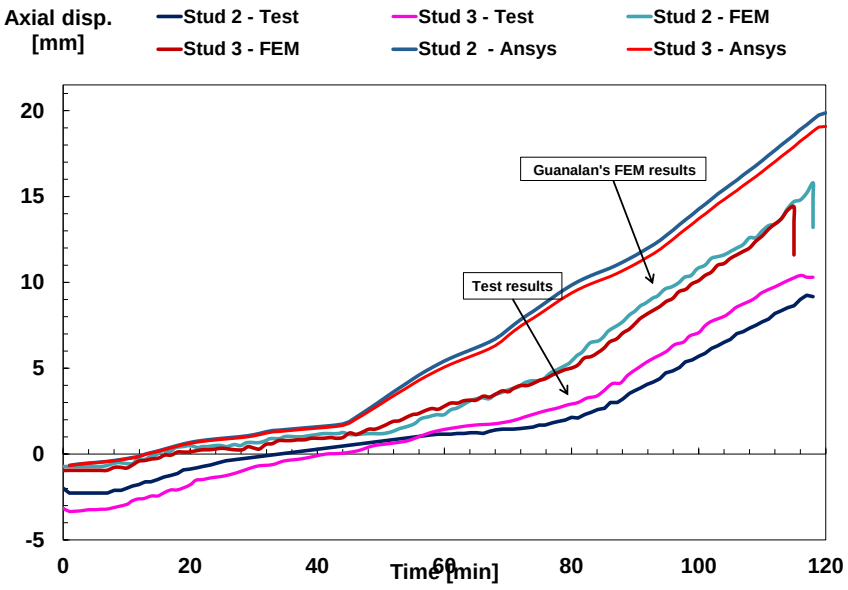

Figure 5.41: Comparison of results. FEM taken from [13] and test results taken from [7].

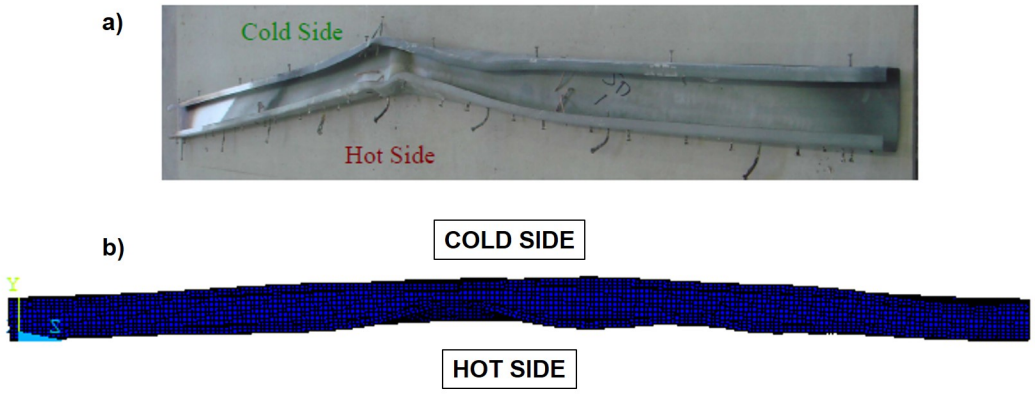

Figure 5.42: Deformed shapes at the time of failure (a): test [2] and (b): FEA.

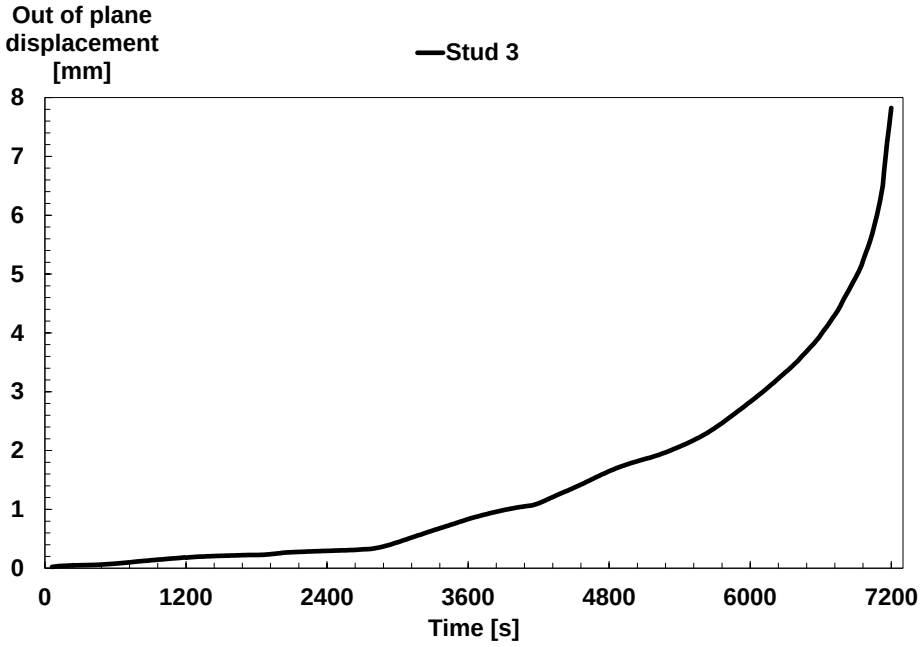

Figure 5.43: Out of plane displacement for Stud 3.

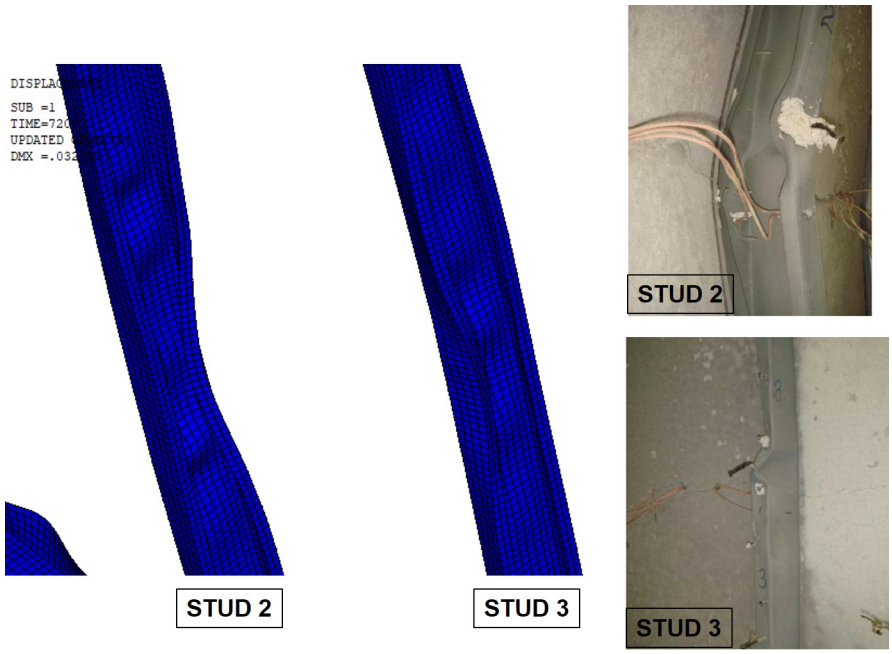

Figure 5.44: In the left: FEA deformed shapes, in the right, test deformed shapes [2].

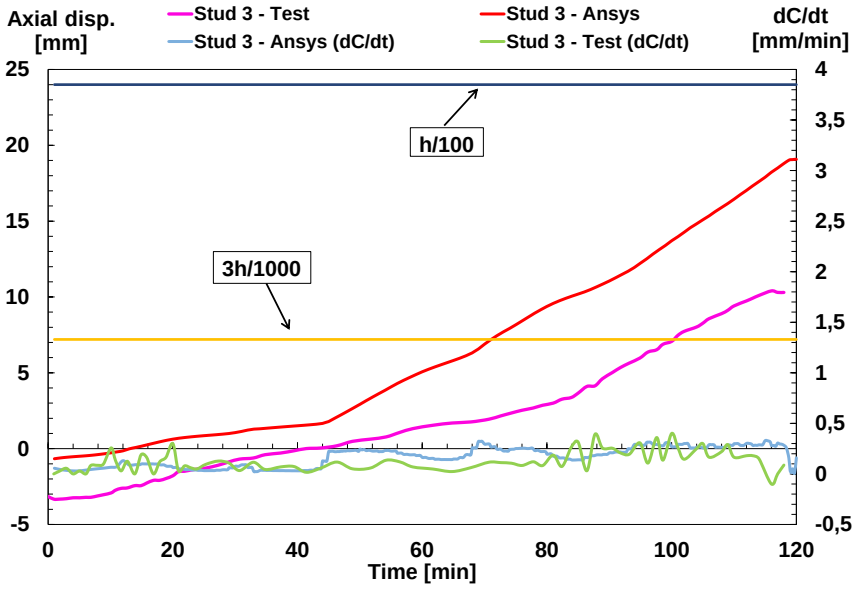

Figure 5.45: Maximum vertical contraction. FEM taken from [13], test from [7].

Chapter 6

Parametric Studies

This chapter aims to verify the influence of different LSF Wall configuration. The influence of plasterboards' thickness, plasterboards' restriction and steel section thickness are to be investigated.

6.1 Influence of the plasterboards

In order to analyse the influence of the plasterboards, an additional simulation was carried out. In this simulation, plasterboards were assumed to have 12,5 [mm] thickness, whereas the previous had 16 [mm].

a) Influence at room temperature

Since the plasterboards do not provide mechanical restriction, the simulation under room temperature did not change in respect to the previous one. Therefore, the same model was used with critical and ultimate load equals to 39,8 [kN] and 78,89 [kN] respectively.

b) Influence on temperature field distribution

To assess the plasterboards influence on thermal distribution a new thermal simulation, case 2 (see Table 6.1), was carried out with lined plasterboard of 12,5 [mm] thickness, as shown in Figure 6.1, the others parameters were kept the same as the previous simulations.

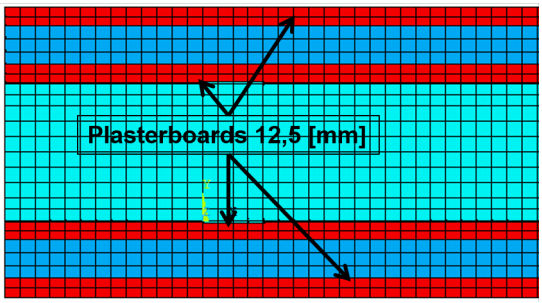

Figure 6.1: Plasterboards lined in the finite element model.

Table 6.1: Cases analysed for plasterboard influence.

Case	Plasterboard thickness [mm]
Case 1 (previous FEM)	16
Case 2	12,5

The boundary conditions were also the same, such as convection and radiation, including the solution method: same time increment and convergence tolerance.

The temperatures curves were extracted in the same point location, as previously done (see Figure 5.30), then, the average value was obtained from the three curves: AS, FS, Pb1-Ins, Ins-Pb2, Pb2-Cav, Pb3-Cav and Ins-Pb4. The results for case 2 (plotted as continuous lines) are plotted in Figure 6.2 together with case 1 (plotted as dotted lines).

There were no differences in the behaviour of the temperature curves, however, the temperatures were higher for case 2 (less protection) than case 1. For Ins-Pb2, case 2 reaches the growth phase at about 8 min whereas case 1, reached at 18 min. Pb2-Cav reaches, for case 1, 120 [°C] at 47 min, whereas case 2, at about 33 min.

This behaviour is seen in all temperature curves and is more noticeable for Pb1-Ins (see Table 6.2), in which, has higher temperature difference between case 1 and 2. This happens because in the case 2's, Pb2 is thinner than case 1, consequently, there is less gypsum mass in the plasterboards. Heat is conducted by the entire plasterboard volume and is transported from one side to another throughout the thickness, this means that the heat resistance by conduction is smaller. Since case 2's plasterboard has lower volume than case 1's plasterboard, more heat will get in the other surface, therefore, higher temperatures will be predicted.

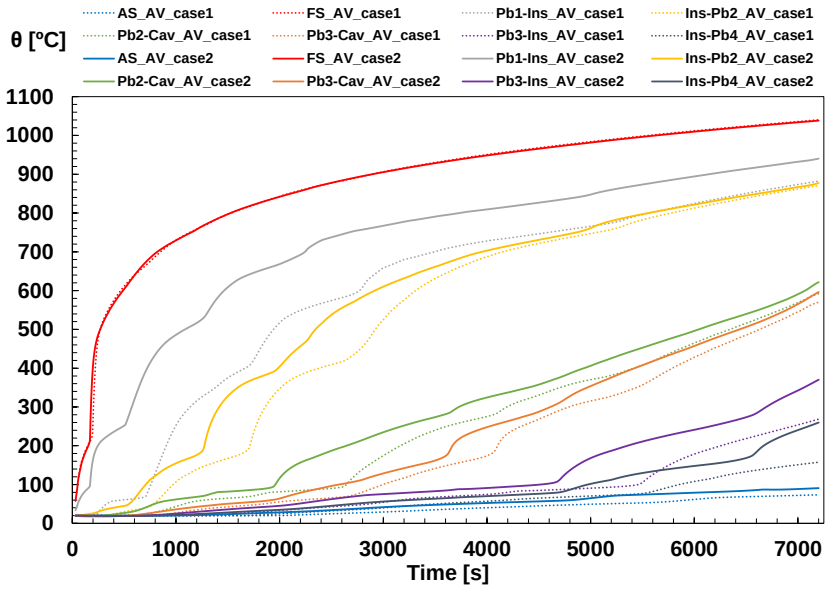

Figure 6.2: Temperature profiles comparison between case 1 and 2.

After reaching the first insulation, Ins-Pb2, the difference is not so high anymore. Values are approaching with very similarly predictions for Pb2-Cav and Pb3-Cav, resulting in a small difference in the maximum and average temperature, when compared with the others curves (see Table 6.2). This happens because, even thou the plasterboards are thinners, the glass fibre insulation is the same, so, almost the same amount of heat is still being transferred by GF. However, more heat is still passing, since GF is getting higher temperatures than for case 1, reason why, the subsequent curves show higher temperature difference. Also it is important to note the wider plateau that is predicted for the evaporation of the gypsum moisture in case 1.

In this comparison, the RMSE value represent the difference that the case 2 was from case 1 point to point, in which, values near 0 states that there were no variation in the temperatures. As far from 0 as it gets, the higher temperature values were obtained in case 2. The fire side temperature was not evaluated due to the fact that his temperature depends on the boundary condition imposed by the ISO 834 curve.

Table 6.2: Difference in average and maximum temperature for case 1 and 2.

Temperature Point	Maximum Temperature [°C]		Error	
	Case 1	Case 2	RMSE	MAX. T. [%]
FS	1040	1040	—-	—-
Pb1-Ins	882	940	1,36	6,1
Ins-Pb2	871	877	0,31	0,6
Pb2-Cav	592	622	0,38	4,82
Pb3-Cav	570	596	0,18	4,3
Pb3-Ins	269	370	0,28	27,2
Ins-Pb4	157	260	0,40	39,6
AS	73	91	0,32	19,7

Another visible gain is seen, as Table 6.2 show, in Pb3-Ins and Ins-Pb4, at Pb3 and Pb4 plasterboard surfaces. As pointed before, more heat is getting though in case 2, therefore, higher heat load is reaching Pb3 and Pb4 surface and since they are thinners than case 1's plasterboards, they are heating up more than case 1. Still, the second glass fibre insulation absolves the same amount of heat, thus, a lower gain is seen at Pb4 outer surface (AS).

For the steel temperatures, all the studs showed the same temperatures curves, thus, only stud 2 and 3 were considered for comparison. The temperature variation of web, cold and hot flange from stud 2 and 3 are plotted in Figure 6.3. The temperature distribution for stud 3 at mid-height is shown in Figure 6.4.

In order to compare with case 1, the average studs temperatures were plotted in Figure 6.5. The temperatures variations are similar, with noticeable difference between about 36 to about 58 min. This behaviour is a consequence of the heat load getting though the Pb2 plasterboard, the graph from Figure 6.2, indicates that in this period, for the case 2, Pb2 temperature is higher, therefore, values, are higher than for the Pb2 in case 1, and that before and after the period they are similar. So, this behaviour is also seen in the stud temperatures variation.

The maximum and average temperatures from both cases are shown in Table 6.3.

In respect to the insulation criteria failure (I) from EN 1363-1 [25], case 2 also did

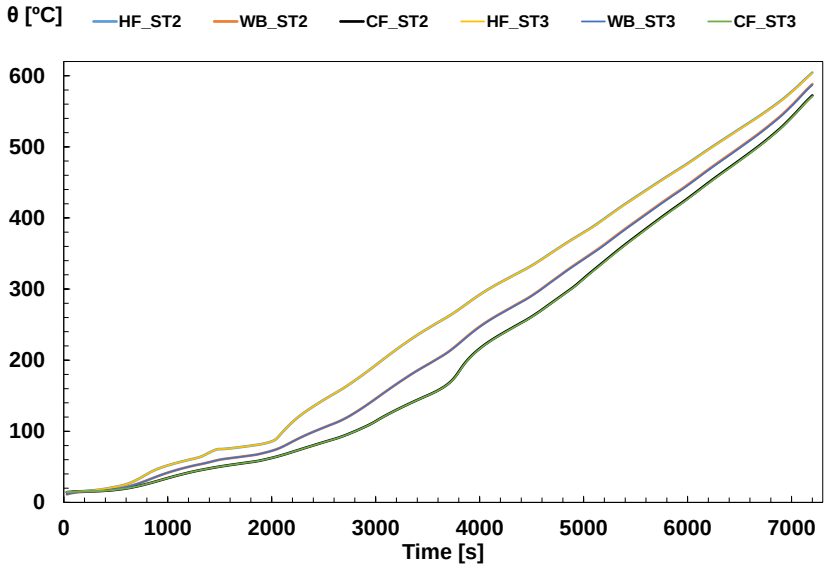

Figure 6.3: Temperature profiles for stud 2 and 3 from case 2 simulation.

Table 6.3: Relative difference for centre studs temperatures.

Stud	Maximum Temperature [°C]		Error	
	Case 1	Case 2	RMSE	MAX. T. [%]
Stud 2	583	604	0,20	3,5
Stud 3	583	604	0,18	3,5

not failed by the maximum and average temperature, as Figure 6.6 shows. However, in comparison with case 1, it showed higher temperatures values.

c) Influence on thermomechanical

The structure numerical failed at 118 min with a critical temperature of 588 [°C], 1% more than case 1 critical temperature, 583 [°C]. The studs' axial displacement is shown in Figure 6.7. Stud 3 showed the lowest displacement while stud 4 showed the highest displacement value.

The graph of Figure 6.8 shows the comparison with case 2 and the evaluation in respect to the load bearing capacity criteria from EN 1363-1 [25]. When compared with case 1, case 2 studs showed higher displacement due to higher temperature gradient across

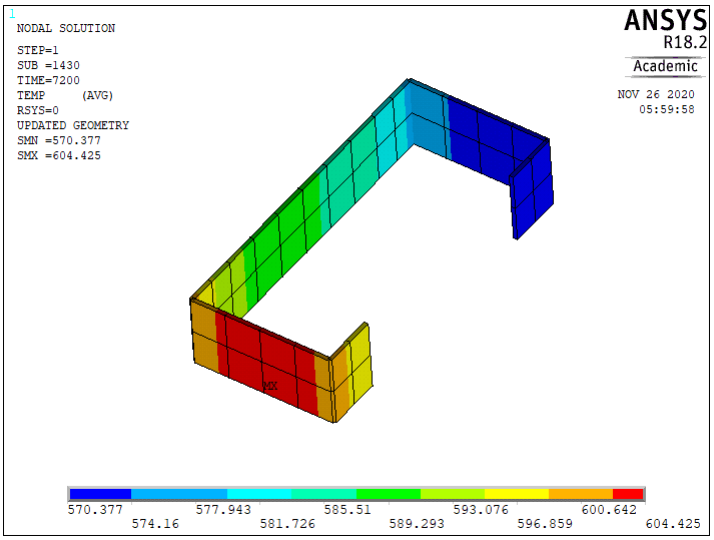

Figure 6.4: Temperature distribution for stud 3 at mid-height.

studs. Still, the configuration with plasterboard of 12,5 [mm] did not fail by load bearing capacity (R).

At the failure time, the LSF wall from case 2 bended towards to the opposite side of the fire (y+), the same way that happened in case 1. The comparison of the out of the plane displacement for both cases are in good agreement, as Figure 6.9 shows. As expected, case 2 showed higher displacement due to the higher temperature distribution.

6.2 Influence of the plasterboard restriction

The influence of the plasterboard restriction was investigated at room temperature and in the thermomechanical response.

a) Influence at room temperature

The influence from the plasterboard restriction was investigated for three cases: (1) with zero restriction, (2) with four restrictions with 600 [mm] between them and (3) seven (as shown in Figure 6.10) restrictions with 300 [mm] between them. The results for the critical load (P_{cr}, elastic buckling) and the ultimate load (U, non-linear simulation) are shown in Table 6.4, the reference value (RV) for error was taken from case 3.

Results showed that there is no substantial difference between case 2 and 3 for the

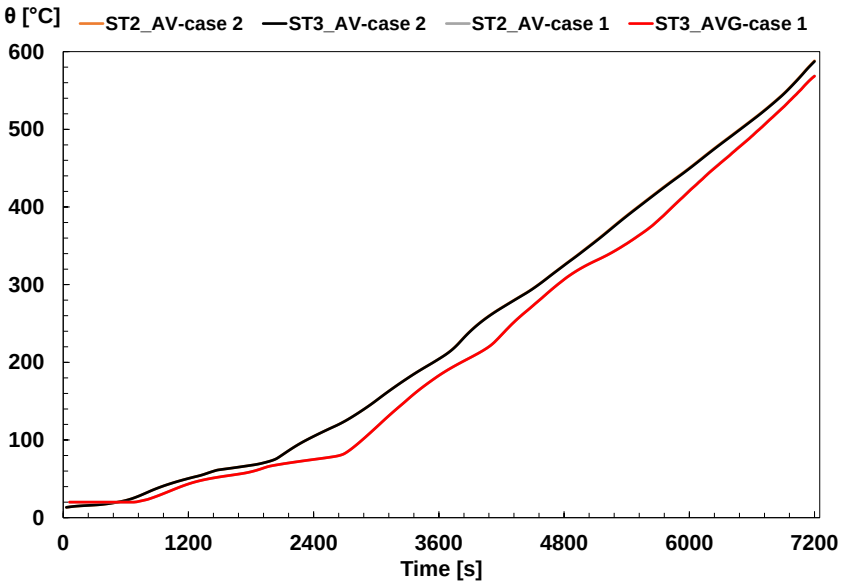

Figure 6.5: Averages studs temperatures for case 1 and 2.

Table 6.4: Effects of the different cases of plasterboard restriction.

Case	P_{cr}[kN]	U [kN]	Relative U error to RV [%]
1	39,85	53,55	32,12
2	39,81	78,76	0,16
3	39,83	78,89	–

ultimate and critical buckling load. However, case 1 was not able to predict the ultimate load, although it was able to predict the P_{cr}. Thus, the plasterboard restriction should be considered, but, more studies are needed in order to determine the real influence to the studs caused by this restriction, due to the fact that the difference between 600 and 300 [mm] were not large, even thou that case 2 has approximately half of restricted nodes when compared with case 3.

b) Influence in the thermomechanical response

Since these restrictions do not influence the thermal behaviour, the temperature distribution (case 3) from the validated model was applied in case 2. Case 1 was not simulated because it was not capable of predicting the ultimate load.

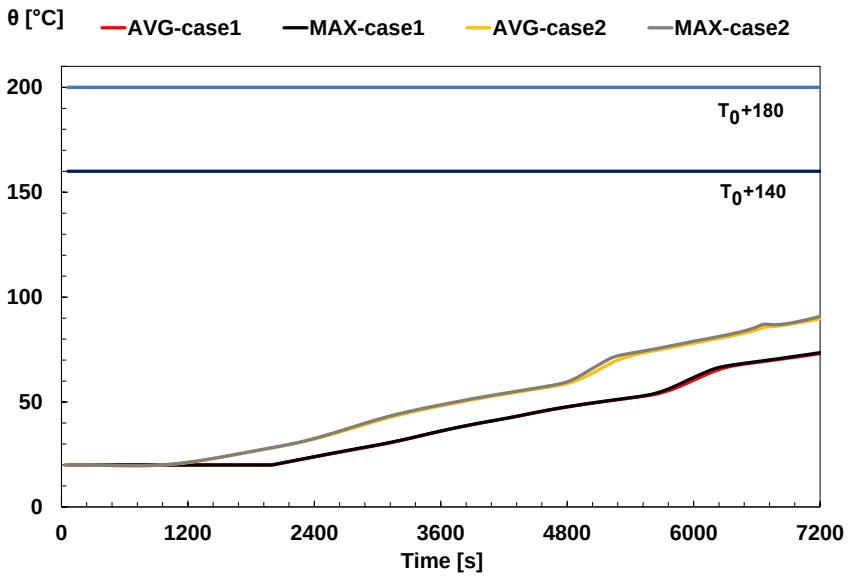

Figure 6.6: Insulation criteria.

The time of failure and critical temperature was the same for case 2 and 3. The studs' displacements from case 1 in comparison with case 2 are given in Figure 5.13. Both models showed exact the same displacement.

In respect to the out of the plane displacement, case 2 showed a slight difference when compared with case 3, but, not so noticeable, therefore, they look like the same. As for the lateral deflection, the model from case 2 presented higher lateral deflection (see Figure 6.12). This happened because the lower number of plasterboards restrains set the studs free to move in the x direction, thus, allowing for higher lateral deflection. During test the lateral deflection was about 15 [mm] [7], in which, both cases were not able to reproduce. This behaviour stated once more that the plasterboard restriction should be further investigated, since it seems to have some influence in lateral deflection.

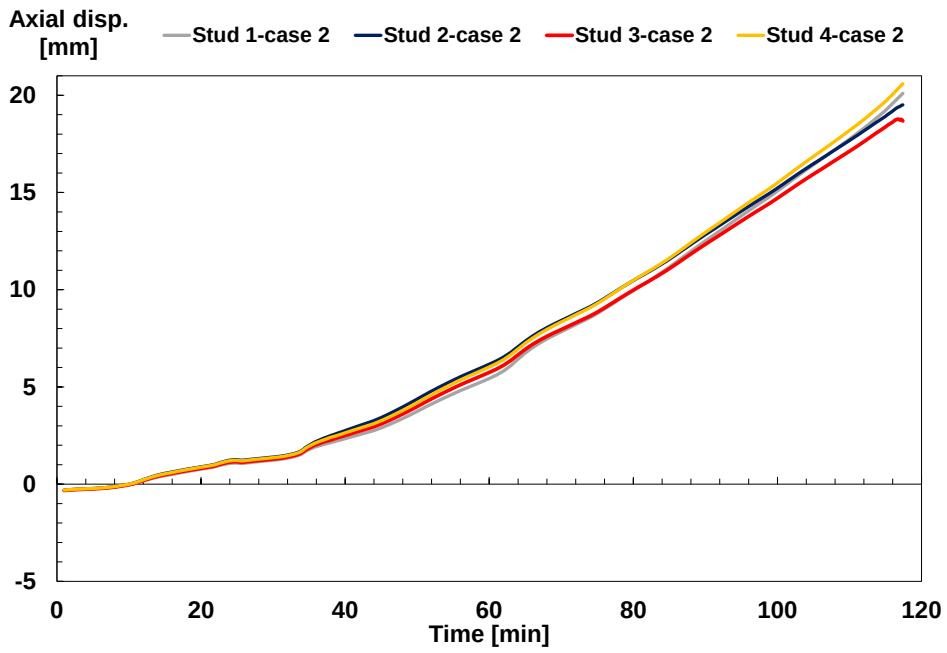

Figure 6.7: Axial displacement for studs in case 2.

Table 6.5: Effects of the different cases of steel sections.

Case	P_{cr}[kN]	U [kN]	Relative P_{cr} and U gain to RV [%]
1	206,91	113	80,75/30,18
2	88	89,68	54,73/12,03
3	39,83	78,89	–/–

6.3 Influence of the steel sections

a) Influence at room temperature

The influence of steel section was investigated in three cases: (1) 2 [mm], (2) 1,5 [mm] and (3) 1,15 [mm] (reference value). The results obtained for critical buckling load (P_{cr}) an ultimate load (U) are in Table 6.5.

Results showed that by raising the steel section, higher values of P_{cr} and U can be obtained. This happens due to higher mechanical resistance granted by the steel section. In particular, for case 1, the gain for critical load is approximately 80% and also, it is

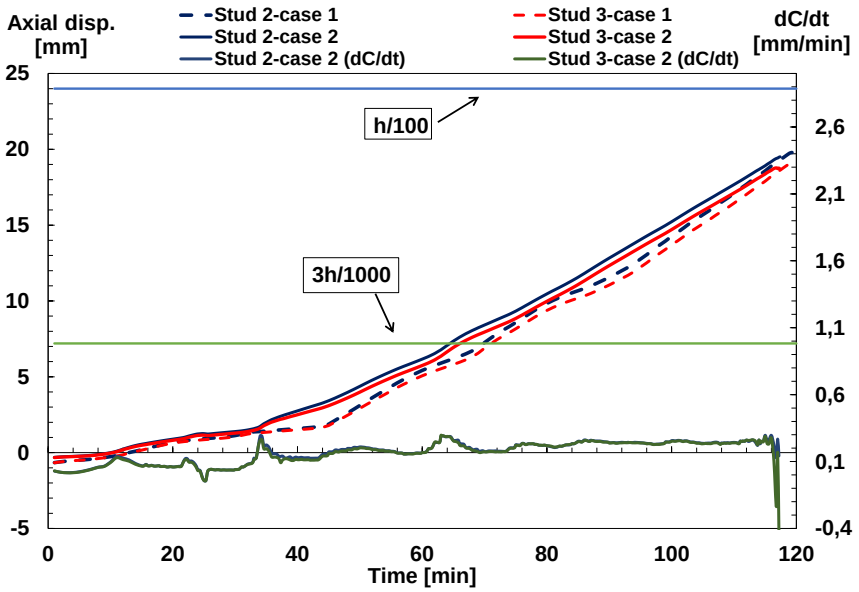

Figure 6.8: Comparison for case 1 and 2.

the only case that the critical load was higher than the ultimate load. This means that for LSF Walls constructed with steel sections of 2 [mm] thick will fail by reaching the ultimate load rather than the buckling load.

The third stud was the one that had the lowest buckling mode for the all cases, Figure 6.13 shows the comparisons of the buckling shape for the three simulated cases. In all cases, the local web buckling is predominant for the lowest mode.

In respect to the axial deformation with respect to the load bearing capacity, case 3 showed higher displacement values for the same reference load, when compared with 2 and 1 (see Figure 6.14). However, the difference between case 2 and 1 was less than 2% for all studs, while for ultimate load the difference was 20,6%.

All cases failed due yielding at the bottom of the studs. A representation of the von Mises stress for all the three cases is showed in Figure 6.15. Maximum equivalent stress for case 1, 2 and 3 were 596, 579, 582 [MPa] respectively, in which, all are above the yield strength of G500 steel, 569 [MPa]. Results showed that, in case 3, had high stress

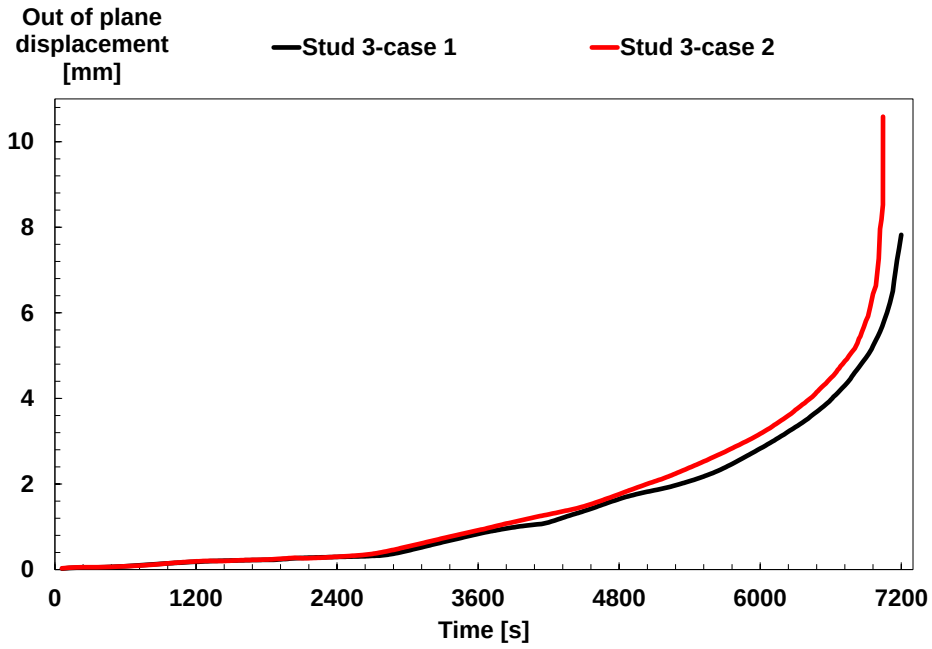

Figure 6.9: Comparison of the out of plane displacement for case 1 and 2.

values along studs (represented by red areas in Figure 6.15), however, for case 1 and 2 that did not happen. This is mainly because thicker steel sections have higher mechanical resistance, thus, resulting in lower stress values. In Figure 6.15 is possible to observe that case 3 has more higher values areas, followed by case 2 and then case 1 that has lower stress value distribution along the stud.

The time of failure and critical temperature were the same for the three cases. In respect to the displacement, there were a slight difference in the maximum displacement for the cases, displacement curves for Stud 3 are plotted in Figure 6.16. Still, the curves followed the exact same pattern until about 100 [min]. As Figure 6.16 shows, none of the cases studied failed by the load bearing capacity criteria from EN 1363-1 [25].

The out of the plane displacement showed noticeable difference between the cases, shown in Figure 6.17. As thinner as the section gets, the higher displacement it suffers. This is related to the bending moment suffered by LSF wall studs, thicker cross sections

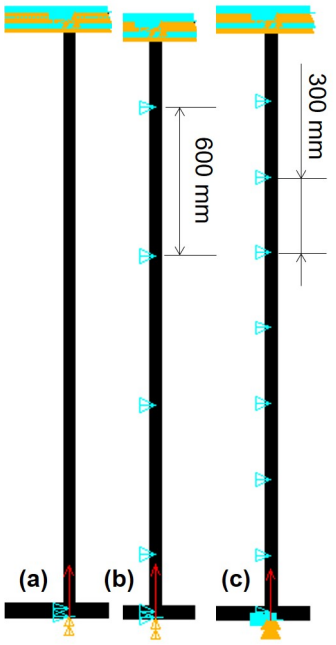

Figure 6.10: Space between plasterboards retrains for: (a) case 1, (b) case 2 and (c) case 3.

have higher inertia moment, therefore, it will be necessary higher bending moments to cause the structure to bend. Since the load applied was the same for the three cases, cases with bigger inertia moment showed lower out of the plane displacement. Still, this could have been affected also by the temperature field or by the alteration of the neutral axis position.

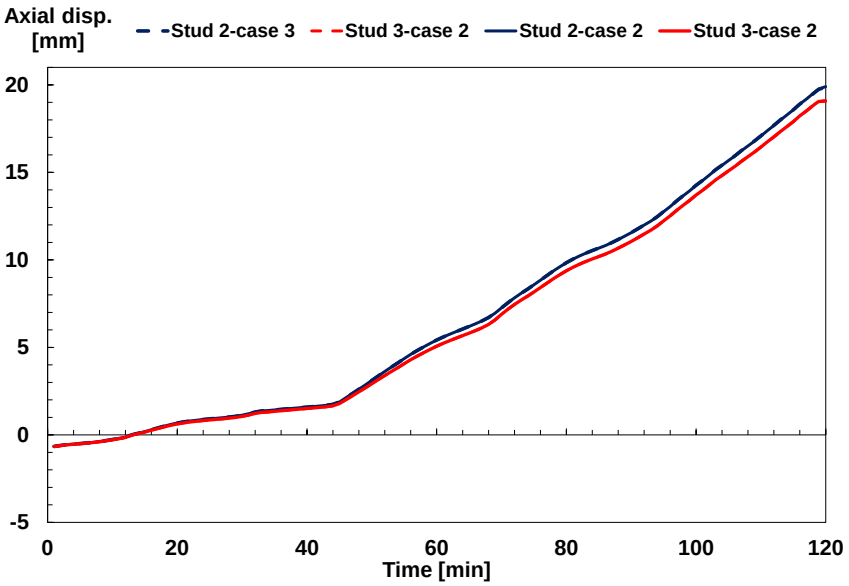

Figure 6.11: Studs' displacements for case 2 and 3.

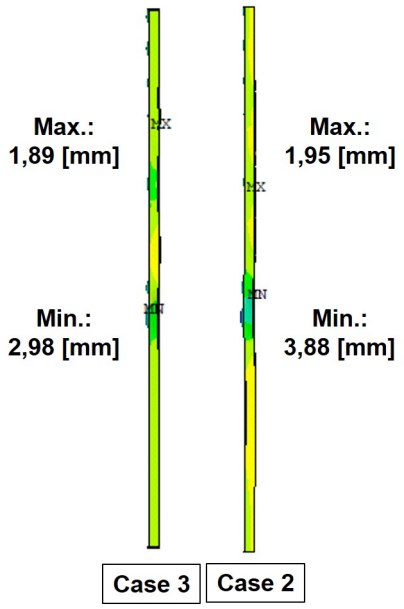

Figure 6.12: X displacement (lateral deflection) for Stud 3.

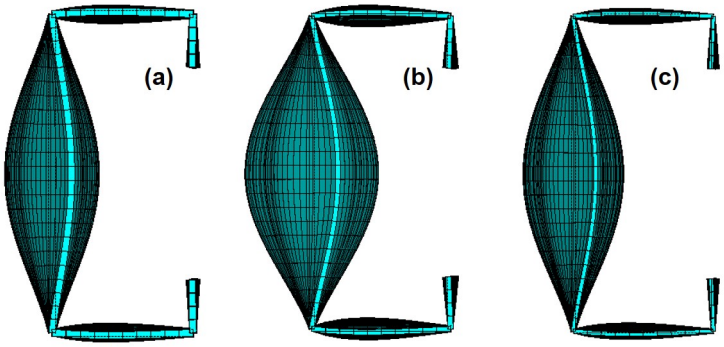

Figure 6.13: Upper view of Stud 3 for: (a) case 1, (b) case 2 and (c) case 3.

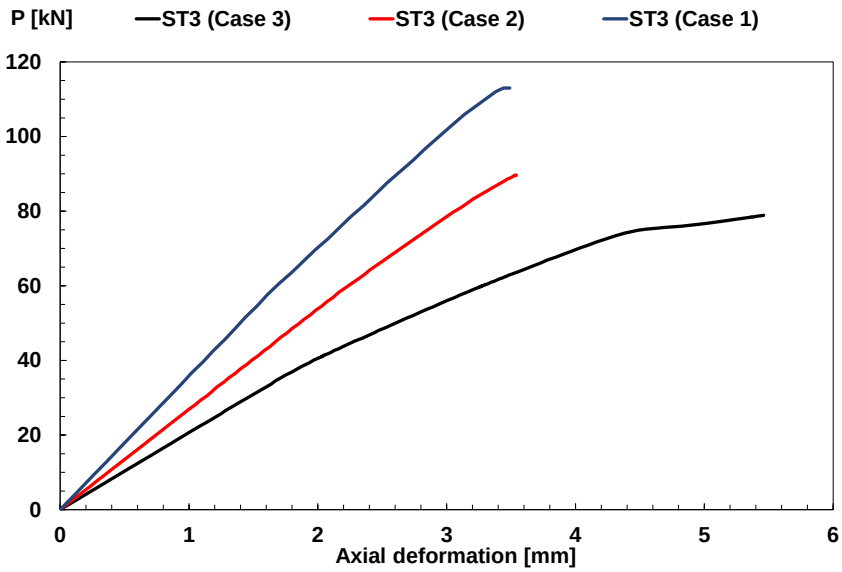

Figure 6.14: Displacement in function of the load for Stud 3.

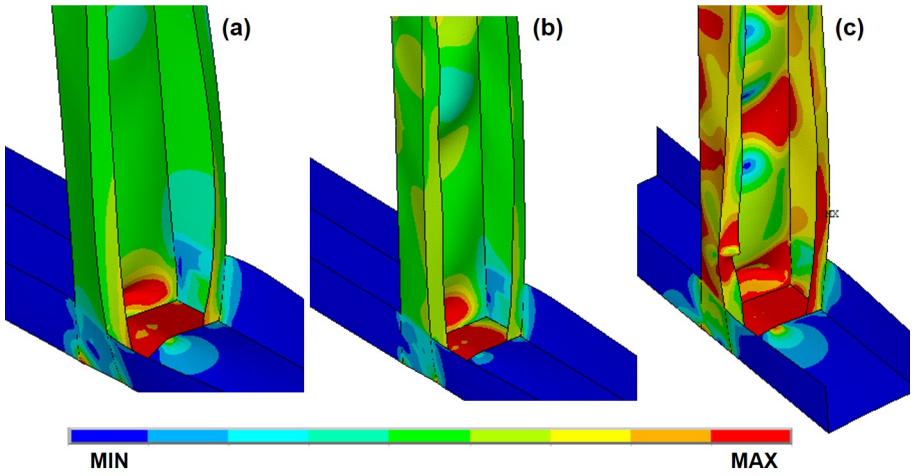

Figure 6.15: Von Mises stress distribution of Stud 3 for: (a) case 1, (b) case 2 and (c) case 3.

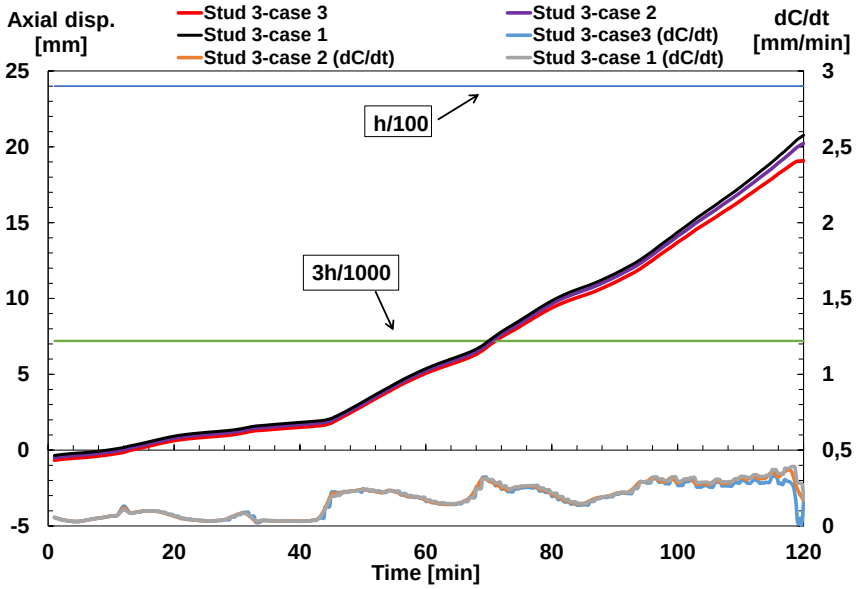

Figure 6.16: Axial displacement for the three cases.

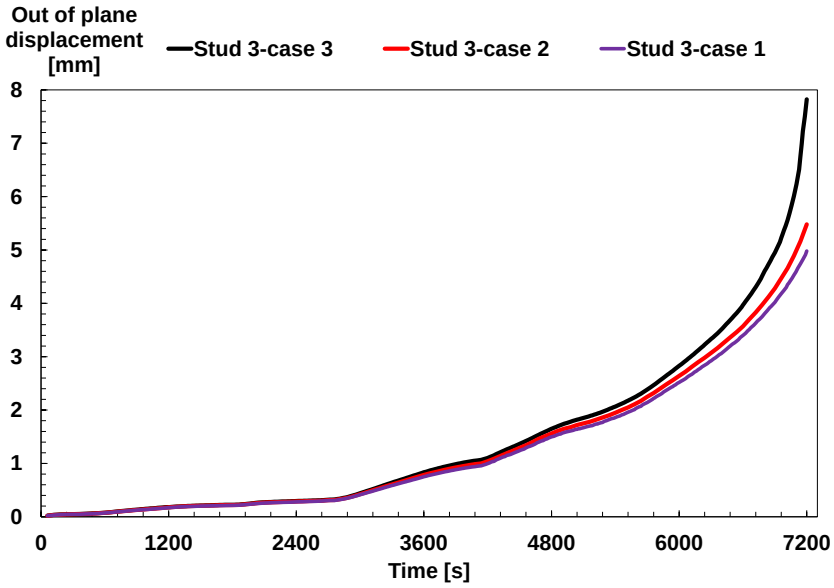

Figure 6.17: Out of plane displacement for the three cases.

Chapter 7

Simplified Method to Estimate Fire Resistance of LSF Walls

This chapter describes the simplified method chosen, in order to compare with test results from Gunalan and Mahendran [7] and the finite element model developed in this work.

When designing for a load bearing LSF walls, the building industry and designers have to make sure that they follows all the standard criteria and have adequate fire resistance. For that, full-scale test or finite element simulation can be carried out, however, these methods can take large time and resources, in order to accomplish the validation of the wall. For those reasons, simplified models were developed.

As the name suggest, simplified methods are simpler design formulas that can be applied for LSF wall, and are usually based in conservative assumptions. Simplified methods can be applied to determine the critical temperature, critical loads and time of failure.

7.1 Prediction of the LSF Wall critical temperature

The fire resistance rating of a wall depends in the amount of load that has been applied to the structure, and it is based in the ultimate load at room temperature. For

the validation of this work, a load ratio of 20% has been used. To a given load ration there is a critical temperature associated, that is the maximum temperature that the studs develop at the failure time. The critical temperature can be used to determine the fire resistance of a LSF Wall.

The first simplified model to be analysed was proposed by Kolarkar [17], in which, the author assume that the cross-sectional areas of the studs remained constant during the test, therefore, the load ratio at failure can be considered equivalent to the strength reduction factor. LR and strength reduction factor are equivalent to the ratio of yield load at elevated temperature to the yield load at room temperature, assuming a constant cross-sectional area [17]. Thus, the reduction factor graph (see Figure 7.1) is used to determine the critical temperature.

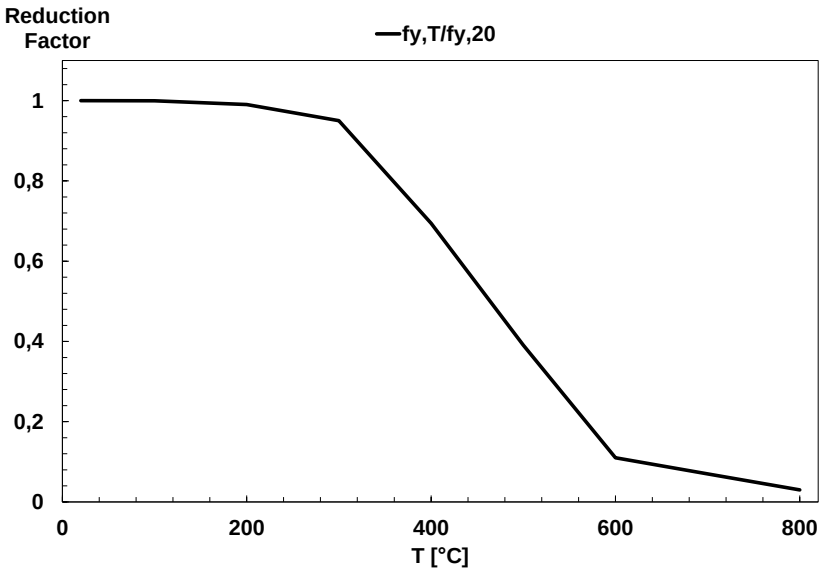

Figure 7.1: Reduction factor for strength [17].

Another model, proposed by Piloto, Khetata and Gavilán, will be presented [19]. The method was developed based on LSF wall lined in both side with plasterboards and consist in applying eq. 7.1 with a given load ratio, μ to determine the critical temperature (θ_{CRI}).

$$\theta_{CRI} = -0,0997 \cdot \mu^2 + 4,0935 \cdot \mu + 506,35 \qquad [°C] \quad (7.1)$$

Load ratio may change from 20 to 80%, in interval of 20%, were applied in eq. 7.1 as a result from the thermomechanical simulation, using the validated FEA models. The comparison is shown in Table 7.1, with relative error in respect to test and FEA from [7], [13], respectively.

Table 7.1: Critical temperature from different solution methods.

Load ratio	θ_{CRI} [°C]	θ_{CRI} FEA [°C]		$\theta^{(1)}_{CRI}$ [°C]		$\theta^{(2)}_{CRI}$ [°C]	
20%	664[3]	583	12	548,35	17%	568	14%
40%	530[4]	556	4,6%	510,57	3,7%	497	6,2%
60%	330[4]	—	—	393,04	16%	436	24,3%
80%	150[4]	—	—	195,75	23,4%	358	58,1%

[1] Taken from [19]; [2] Taken from [17]; [3] Taken from [7]; [4] Taken from [13].

Results implies that the simplified models analysed are conservative for this LSF Wall. Kolarkar [17] assumption is not conservative for higher load ratios, due to the fact that his model only takes into consideration the material reduction properties and do not account for the LSF wall design such as plasterboards or insulation's influence. The same results are showed by Piloto, Khetata and Gavilán's [19] method, but with less deviation. Their model accounted for the LSF wall design, however, the configuration of the test specimens used to develop the formula were different than the ones here simulated. In their study, the walls did not have external insulation between plasterboard as the model in this study had.

In addition, the EN 1993-1.2 presents a simplified approximation by stating that, for members with class 4 sections, the load bearing function of the steel member should be assumed to be maintained after a time t, if, the steel temperature at all cross-sections is not more than 350 [°C], which implies in a very conservative method [26].

Simplified calculations are a good approximation method when advanced methods or full-scale test are not available.

Chapter 8

Conclusions

This work presented a numerical validation study of load bearing light steel frame (LSF) walls structure. Three parametric analysis were performed to evaluate the influence of plasterboard thickness, plasterboard restriction and steel section influence. Two simplified model were assessed in order to obtain the critical temperature in respect to the load ratio applied on the wall.

The model was validated at room temperature with good displacement and ultimate load agreement. Regarding temperature distribution, the model predicts very well the time history curves placed after the first glass fibre insulation, previous curves showed higher error due to plasterboard fall off during test, still, the model was considered validated with good agreement. As for the thermomechanical, the model was not able to predict displacements with good accuracy, but could predict the deformed shape mode at failure time, such as the out of plane displacement due to bending moments created by the thermal bowing and load eccentricity (neutral axis displacement to the cold side during fire simulation).

The plasterboard thickness has a major influence in the temperature distribution, sharply in the temperature curves located at any of the two plasterboards. For this reason, higher temperature distribution was obtained in the studs, causing the LSF wall to numerically fail sooner than the original model. The critical temperature was also higher when compared with the validated model.

The plasterboard restrains in the plane of the wall, influences the ultimate load. However, it did not show relevant influence in cases where there were less restrains. Thermomechanical response was only affected in respect to the lateral deflection.

The thickness of the steel presented relevant influence in the critical load and ultimate load, due to the higher mechanical resistance. There were no noticeable differences in the studs' displacements in thermomechanical response, but, out of plane displacement is affected, in thicker steel sections, lower displacements are obtained.

Simplified models were able to predict the critical temperature, in respect to the load ratio, with conservative deviation for load ratios until 40%, higher load ratios it did not predict with conservative deviation.

For future works, the validation of the thermomechanical model should be done. In addition, others parametric studies such as thinner plasterboards, different insulation material, different distance between studs, should be analysed in order to obtain the influence of those parameters. A new simplified calculation based on a complete validated model, of this LSF Wall, should be developed.

References

[1] F. Alfawakhiri, M. A. Sultan, and D. H. MacKinnon, "Fire resistance of loadbearing steel-stud walls protected with gypsum board: A review", *Fire Technology*, vol. 35, no. 4, pp. 308–335, 1999.

[2] S. Gunalan, "Structural Behaviour and Design of Cold-formed Steel Wall Systems under Fire Conditions", Thesis (Doctoral), Queensland University of Technology, 2011.

[3] B.C. Son; H. Shoub, "Fire Endurance Tests of Double Module Walls of Gypsum Board and Steel Studs", no. April, p. 27, 1973.

[4] K. H. Klippstein, "Behavior of Cold-Formed Steel Studs in Fire Tests.", *Oil Shale Symposium Proceedings*, pp. 275–300, 1980.

[5] J. T. H. Gerlich, "Design of Loadbearing Light Steel Frame Walls for Fire Resistance", *Fire Engineering Research Report 95/3*, p. 118, 1995.

[6] V. K. R. Kodur and M. A. Sultan, "Factors influencing fire resistance of load-bearing steel stud walls", *Fire Technology*, vol. 42, no. 1, pp. 5–26, 2006.

[7] S. Gunalan, P. Kolarkar, and M. Mahendran, "Experimental study of load bearing cold-formed steel wall systems under fire conditions", *Thin-Walled Structures*, vol. 65, pp. 72–92, 2013.

[8] S. Kesawan and M. Mahendran, "Fire tests of load-bearing LSF walls made of hollow flange channel sections", *Journal of Constructional Steel Research*, vol. 115, pp. 191–205, 2015.

[9] Y. Dias, P. Keerthan, and M. Mahendran, "Predicting the fire performance of LSF walls made of web stiffened channel sections", *Engineering Structures*, vol. 168, no. December 2017, pp. 320–332, 2018.

[10] S. Kesawan and M. Mahendran, "Predicting the performance of LSF walls made of hollow flange channel sections in fire", *Thin-Walled Structures*, vol. 98, pp. 111–126, 2016.

[11] F. Alfawakhiri and M. A. Sultan, "Fire Resistance of Loadbearing LSF assemblings", in *15th International Specialty Conference on Cold-Formed Steel Structures*, St. Louis, Missouri, 2000, pp. 545–561.

[12] Y. Telue and M. Mahendran, "Design of Cold-formed Steel Wall Frames Lined with Plasterboard on One Side under Axial Compression", *International Journal of Steel Structures*, vol. 6, no. 1, pp. 1–12, 2006.

[13] S. Gunalan and M. Mahendran, "Finite element modelling of load bearing cold-formed steel wall systems under fire conditions", *Engineering Structures*, vol. 56, pp. 1007–1027, 2013.

[14] K. H. Klippstein, "Strength of Cold-Formed Steel Studs Exposed To Fire.", *4th International Specialty Conference on Cold-Formed Steel Structures*, vol. 1, pp. 513–555, 1978.

[15] G. M. E. Cooke, "The structural response of steel I-section members subjected to elevated temperature gradients across the section", Thesis (Doctoral), City University London, 1987.

[16] B. Zhao, S. Zajac, J. Komenda, P. Morris, P. Dierickx, S. Matera, and F. Peñalba-Diaz, "Calculation rules of lightweight steel sections in fire situations", European Comission, Luxembourg, Tech. Rep. 7215, 2005, pp. 1–243.

[17] P. N. Kolarkar, "Structural and Thermal Performance of Cold-formed Steel Stud Wall Systems under Fire Conditions", Thesis (Doctoral), Queensland University of Technology, 2010.

[18] S. Gunalan and M. Mahendran, "Fire performance of cold-formed steel wall panels and prediction of their fire resistance rating", *Fire Safety Journal*, vol. 64, pp. 61–80, 2014.

[19] P. A. G. Piloto, M. S. Khetata, and A. B. R. Gavilán, "Loadbearing capacity of lsf walls under fire exposure", *MATTER: International Journal of Science and Technology*, vol. 4, pp. 104–124, 2018.

[20] W. Chen, J. Ye, Q. Zhao, and J. Jiang, "Full-scale experiments of gypsum-sheathed cavity-insulated cold- formed steel walls under different fi re conditions", *Journal of Constructional Steel Research*, vol. 164, p. 105 809, 2020.

[21] A. H. Buchanan and A. K. Abu, *Structural Design for Fire Safety*, Second. Chichester, West Sussex, United Kingdom: John Wiley & Sons, Ltd, 2017.

[22] E. 1991-1-2, *Eurocode 1: Actions on Structures - Part 1-2: General Actions - Actions on Structures Exposed to Fire*. Brussels: European Committee for Standardization, 2002.

[23] J. Purkiss, *Fire Safety Engineering Design of Structures*, Second. Oxford: Butterworth-Heinemann, 2007, p. 424.

[24] F. Alfawakhiri, "Behaviour of Cold-Formed-Steel-Framed Walls and Floors in Standard Fire Resistance Tests", PhD thesis, Carleton Univesity, 2001.

[25] E. 1363-1, *Fire resistance tests - Part 1: General Requirements*. Brussels: European Committee for Standardization, 2020.

[26] E. 1993-1-2, *Eurocode 3: Design of Steel Structures. Part 1-2: General Rules - Structural Fire Design*. Brussels: European Committee for Standardization, 2005.

[27] ANSYS, Inc., *Ansys® Academic Research Mechanical, Help System*, version 18.2.

[28] B. Schafer and T. Peko, "Computational modeling of cold-formed steel : Characterizing geometric imperfections and residual stresses", *Journal of Constructional Steel Research*, vol. 47, pp. 193–210, 1998.

[29] N. Vasios. (2015). Nonlinear Analysis of Structures, [Online]. Available: https://scholar.harvard.edu/files/vasios/files/ArcLength.pdf (visited on 08/20/2020).

[30] P. Keerthan and M. Mahendran, "Numerical modelling of non-load-bearing light gauge cold-formed steel frame walls under fire conditions", *Journal of Fire Sciences*, vol. 30, no. 5, pp. 375–403, Sep. 2012.

[31] T. Ranawaka and M. Mahendran, "Experimental study of the mechanical properties of light gauge cold-formed steels at elevated temperatures", *Fire Safety Journal*, vol. 44, no. 2, pp. 219–229, 2009.

Appendix A

LSF Wall Drawings

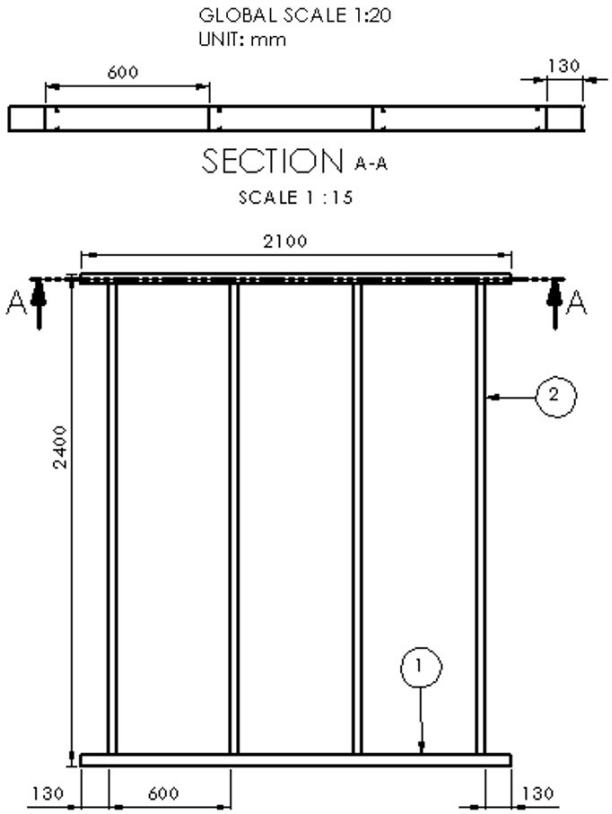

Figure A.1: Front view of the LSF Wall (Modified from [13]).

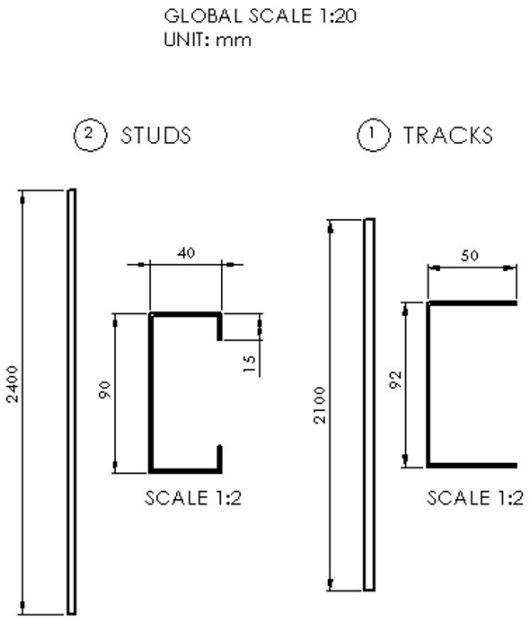

Figure A.2: Stud and Track drawings (Modified from [13]).

Appendix B

Material Properties

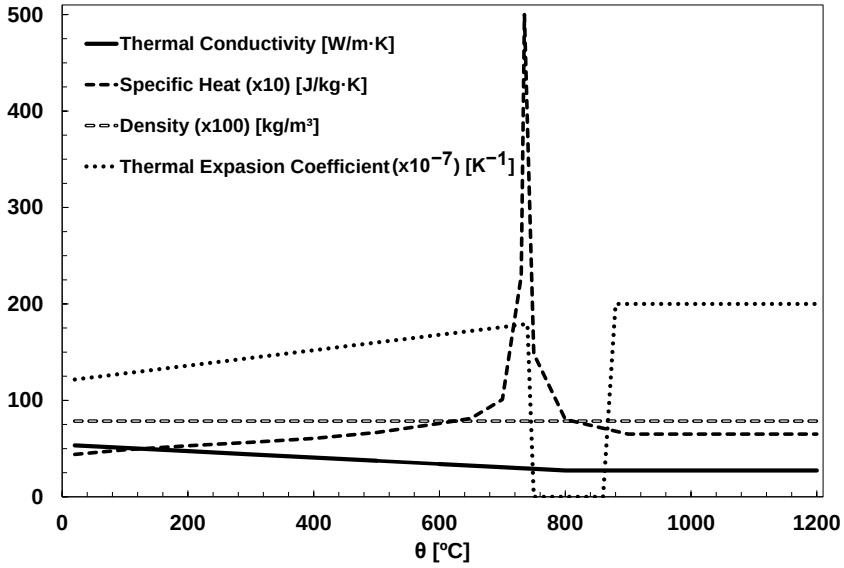

Figure B.1: Thermal properties of Steel [25].

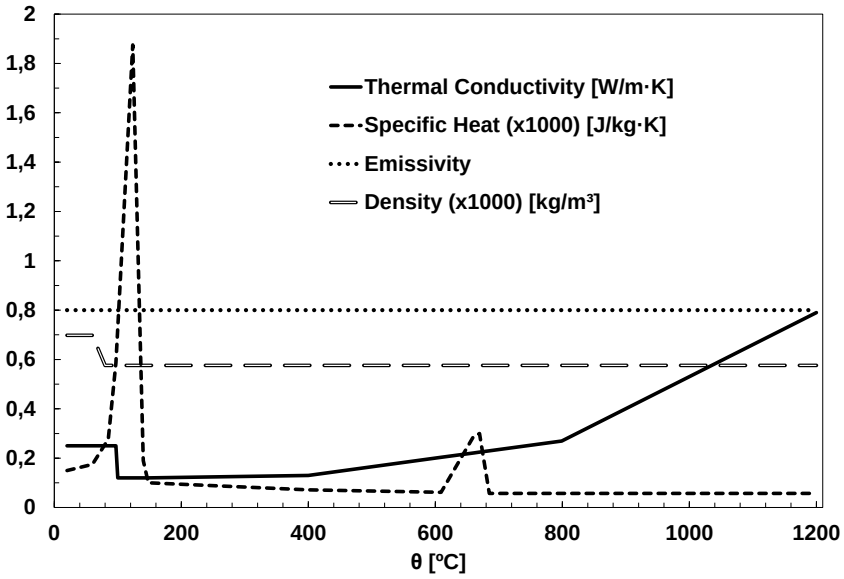

Figure B.2: Thermal properties of Gypsum [30].

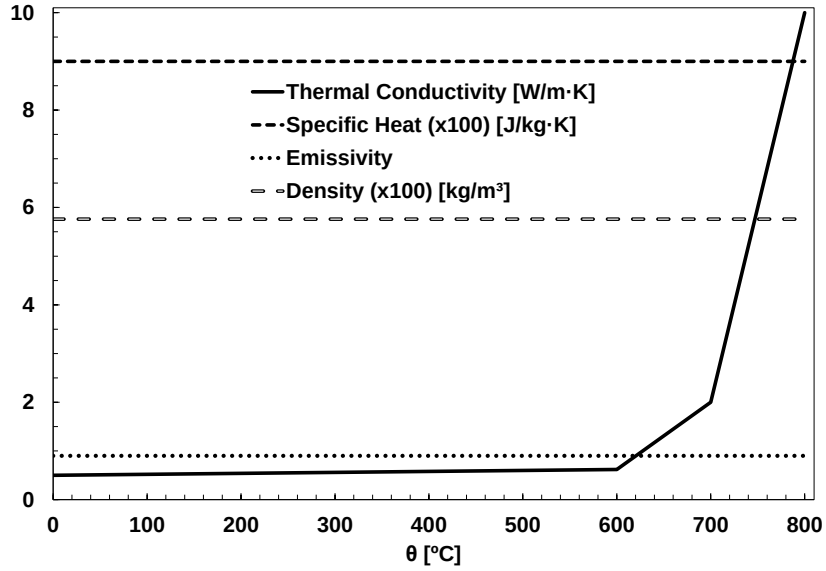

Figure B.3: Thermal properties of Glass Fibre [30].